UNIVERSITY OF OKLAHOMA

GRADUATE COLLEGE

MODELING OF FREE SURFACE MOTION DURING IMPREGNATION OF A POROUS FIBER BED

A Dissertation

SUBMITTED TO THE GRADUATE FACULTY

in partial fulfillment of the requirement for the

degree of

Doctor of Philosophy

By

JUFANG HE
Norman, Oklahoma
2000

UMI Number: 9975797

MODELING OF FREE SURFACE MOTION DURING IMPREGNATION OF A POROUS FIBER BED

A DISSERTATION
APPROVED FOR THE SCHOOL OF
AEROSPACE AND MECHANICAL ENGINEERING

BY

Acknowledgements

I would like to send my deepest appreciation to my advisor, Dr. Altan, for his support, encouragement and guidance throughout my graduate work at the University of Oklahoma. Especially during my research work leading to this dissertation, Dr. Altan constantly gave me valuable suggestions and commends. I could not have finished this dissertation without the help from Dr. Altan. Also, I would like to thank all the faculty members of my dissertation committee: Dr. O'Rear, Dr. Striz, Dr. Lai, and Dr. Parthasarathy for all the discussions and beneficial suggestions during my work for this dissertation.

My valuable education as well as everything wonderful in my whole life comes from the long-lasting and selfishness love from my parents, He, Ming Jie and Chen, Qiao Feng. Especially at the hard times of my life, they are always standing behind me. I dedicate this dissertation to them.

I would like to thank all my family members, my husband Jin Cao and my son Michael Cao for their understanding and love to me. My husband Jin Cao's support and understanding greatly encouraged me in all of my work. My son Michael Cao helped me by being a good kid. I thank my friends, Ma, Hongguo and his family, Zhou, Mengjuan and her family; and all other friends who helped me in my work as well as in my life in Norman, OK.

I would also like to thank NASA microgravity research program for the finical support of this research.

Contents

Chapter 1	INTRODUCTION	1
1.1	Capillary Flow in Porous Me...........................	1
1.2	Static Free Surface Shape...............................	2
1.3	Dynamics of Capillary Flow in Porous Media........	7
1.3.1	Darcy's Law and the Permeability of Porous Media...	7
1.3.2	Capillary Tube Model....................................	9
1.3.3	Dynamic Contact Angle During Capillary Motion..	12
1.3.4	Permeability of a Fiber Bed..............................	14
1.4	Scope of This Dissertation...............................	22
Chapter 2	STATIC FREE SURFACE SHAPE IN A TWO-DIMENSIONAL CHANNEL................	25
2.1	Introduction...	25
2.2	Theory...	27
2.3	Free Surface Shape in a Vertical Channel.............	29
2.4	Free Surface Shape in an Inclined Channel............	39

2.5	Free Surface Shape in a Horizontal Channel..........	46
2.6	Conclusion..	54
Chapter 3	QUASI-STATIC IMPREGNATION OF A FIBER BED BY CAPILLARY FORCES IN A GRAVITY FIELD..	55
3.1	Introduction...	55
3.2	Quasi-Steady Capillary Motion With Gravity Effect..	59
3.2.1	Capillary Motion in a Uniform Channel..............	59
3.2.2	Capillary Impregnation of a Fiber Bed................	69
3.3	Quasi-Steady Impregnation of Fiber Beds............	71
3.4	Fluid Front Motion during Capillary Impregnation..	75
3.5	Permeability Predictions.................................	86
3.6	Conclusion..	90
Chapter 4	TRANSVERSE IMPREGNATION OF AN ANISOTROPIC FIBER BED BY CAPILLARY FORCES..	93
4.1	Introduction...	93

4.2 Fiber Packing Pattern................................. 95

4.3 Anisotropic Capillary Impregnation of a Fiber Bed.. 99

4.4 Results of Fluid Front Motion.......................... 102

4.5 Prediction of the Anisotropic Permeability of a Fiber Bed... 111

4.6 Conclusion.. 117

Chapter 5 FIBER BED IMPREGNATION WITH EXTERNAL PRESSURE AND PERMEABILITY USING EXTENDED LUBRICATION THEORY 118

5.1 Introduction.. 118

5.2 Impregnation of a Fiber Bed with External Pressure.. 120

5.2.1 Fluid Front Motion and Shape Change 120

5.2.2 Fluid Front Shapes and Locations during the Flow.. 123

5.3 Extended Lubrication Model for Fiber Bed Permeability Prediction... 125

5.3.1 Previous Works.. 125

5.3.2 Extended Lubrication Model.............................. 136

5.3.3 Permeability Prediction of Different Fiber Packing Patterns.. 147

5.4 Conclusion... 154

Chapter 6 GENERAL CONCLUSIONS.................................... 156

BIBLIOGRAPHY.. 159

List of Figures

Figure 2.1	Coordinate system and the relevant geometric parameters used in the calculation of free surface shape in a vertical channel	31
Figure 2.2	Iterations of shooting method in the numerical calculation of free surface shape	34
Figure 2.3	Free surface shapes in a vertical channel under different Bond numbers when contact angle is 30 degrees	37
Figure 2.4	Free surface shapes in a vertical channel under different Bond numbers when contact angle is 60 degrees	38
Figure 2.5	Free surface in an inclined channel and the coordinate system used in the analysis	40
Figure 2.6	Free surface shapes in an inclined channel under different Bond numbers when contact angle is 30 degrees and inclination angle is 30 degrees	42

Figure 2.7	Free surface shapes in an inclined channel under different Bond numbers when contact angle is 60 degrees and inclination angle is 30 degrees	43
Figure 2.8	Free surface shapes in an inclined channel under different Bond numbers when contact angle is 30 degrees and inclination angle is 60 degrees	44
Figure 2.9	Free surface shapes in an inclined channel under different Bond numbers when contact angle is 60 degrees and inclination angle is 60 degrees	45
Figure 2.10	Free surface in a horizontal channel and the coordinate system used in the analysis	48
Figure 2.11	Free surface shapes in a horizontal channel under different Bond numbers when contact angle is 30 degrees	52
Figure 2.12	Free surface shapes in a horizontal channel under different Bond numbers when contact angle is 60 degrees	53
Figure 3.1	Capillary motion in a vertical channel and the coordinate system used in the analysis of the motion	60

Figure 3.2 Change of the height of the fluid front during capillary motion in a uniform channel when contact angle is 30 degrees........ 67

Figure 3.3 Change of the height of the fluid front during capillary motion in a uniform channel when contact angle is 60 degrees........ 68

Figure 3.4 Motion of fluid front during capillary impregnation of a fiber bed and the relevant parameters........ 73

Figure 3.5 Change of vertical impregnation distance during impregnation for different fiber volume fractions. $Bo=5.72\times10^{-8}$; $\theta=0^0$ 76

Figure 3.6 Change of vertical impregnation distance during impregnation for different fiber volume fractions. $Bo=1.27\times10^{-8}$; $\theta=20^0$ and 30^0........ 77

Figure 3.6a Change of vertical impregnation distance during impregnation of the initial layers of fibers. $Bo=1.27\times10^{-8}$; $\theta=20^0$........ 78

Figure 3.6b Change of impregnation velocity with time during impregnation of the initial layers of fibers.

v_f = 80%; Bo =1.27×10^{-8}; θ=20^0........................ 78

Figure 3.7 Location and shape of the fluid fronts at different times during impregnation for 70% fiber volume fraction.. 80

Figure 3.8 Location and shape of the fluid fronts at different times during impregnation for 85% fiber volume fraction.. .81

Figure 3.9 Change of vertical impregnation distance during impregnation for different Bond numbers. Bo =5.72×10^{-8}; v_f=70%; θ=0^0..................... 82

Figure 3.10 Change of vertical impregnation distance during impregnation for different Bond numbers. Bo =1.27×10^{-8}; v_f=80%; θ=0^0......................... 83

Figure 3.11 Change of vertical impregnation distance during impregnation for different Bond numbers. Bo =1.27×10^{-8}; v_f=80%; θ=20^0........................ 87

Figure 3.12 Comparison of permeability predictions obtained from current study with lubrication model and experimental data. $e=1-v_f$.. 91

Figure 4.1 Fiber arrangement pattern used in this study........... 97

Figure 4.2 Fiber arrangement criteria for possible capillary impregnation using different contact angles............. 98

Figure 4.3 Location and shape of the fluid fronts at different times during capillary impregnation. v_f=70%; β=60^0; θ =0^0.. 105

Figure 4.4 Location and shape of the fluid fronts at different times during capillary impregnation. v_f=70%; β=30^0; θ =0^0.. 106

Figure 4.5 Change of impregnation height with time during impregnation for different flow directions. v_f=70%; β =60^0;θ=0^0... 107

Figure 4.6 Gravity effect during the impregnation of a hexagonal fiber bed for different fiber volume fractions. β=60°; θ =0^0; Bo=5.72×10^{-8}.......................................108

Figure 4.7 Gravity effect during the impregnation of a hexagonal fiber bed for different contact angles. β=60°; v_f= 70%; Bo=5.72×10^{-8}.................................109

Figure 4.8 Location and shape of the fluid fronts at different times during capillary impregnation. v_f=70%; β=45^0; θ=0^0..........110
Figure 4.9 Permeability $\overline{K}_x$ prediction with fiber volume fraction for different packing angles.......... 112
Figure 4.10 Permeability $\overline{K}_y$ prediction with fiber volume fraction for different packing angles.......... 113
Figure 4.11 Fitting of a circular tube into space among fibers to calculate longitudinal permeability.......... 114
Figure 5.1 Location and shape of the fluid fronts at different times during impregnation for 70% fiber volume fraction. δ =0.5.......... 126
Figure 5.2 Location and shape of the fluid fronts at different times during impregnation for 70% fiber volume fraction. δ =0.3.......... 127
Figure 5.3 Change of vertical impregnation distance during impregnation for different external pressure. v_f=70%.......... 128

Figure 5.4 Location and shape of the fluid fronts at different times during impregnation for 85% fiber volume fraction. δ =0.1 129

Figure 5.5 Change of vertical impregnation distance during impregnation for different external pressure. v_f=85% 130

Figure 5.6 Permeability prediction using lubrication model for flow through the channel between fiber surfaces when fibers are arranged in square pattern 132

Figure 5.7 Permeability prediction using lubrication model for flow through the channel between fiber surfaces when fibers are arranged in hexagonal pattern 134

Figure 5.8 Permeability prediction using lubrication model for different flow directions relative to the isosceles triangle of the fiber arrangement 138

Figure 5.9a Separation of flow channel for permeability prediction using lubrication model when flow direction is shown as v_a in Fig. 5.8 139

Figure 5.9b Separation of flow channel for permeability prediction using lubrication model when flow direction is shown as v_b in Fig. 5.8 140

Figure 5.10 Permeability prediction using lubrication model for different flow directions when fibers are arranged in rectangular pattern 146

Figure 5.11 Permeability change with fiber volume fraction using extended lubrication model and the comparison with Bruschke's prediction. Fibers are packed in hexagonal pattern. e=1-v_f 148

Figure 5.12 Permeability change with fiber volume fraction using extended lubrication model. Fibers are packed in isosceles triangular pattern. β=50° 149

Figure 5.13 Permeability change with fiber volume fraction using extended lubrication model. Fibers are packed in isosceles triangular pattern. β=45° 150

Figure 5.14 Permeability change with fiber volume fraction using extended lubrication model. Fibers are packed in square pattern 151

Figure 5.15 Permeability change with fiber volume fraction using extended lubrication model. Fibers are packed in rectangular pattern with different ratio of the two sides..152

List of Tables

Table 4.1 Ratio of longitudinal to normal permeability for different packing angles... 115

Abstract

This work studies the free fluid surface shape and its motion through a porous fiber bed. The static free surface shape in a two-dimensional channel is numerically calculated. The results of the free surface shape are presented for different Bond numbers, contact angles and inclination angles. When analytical solution is available, numerical results are compared with the analytical results. Free surface shapes and locations are solved when the fluid is driven by capillary forces to flow through an anisotropic fiber bed. Such motion is simulated using the theory of creeping flow through a two-dimension channel. The results of free surface motion are presented for different fiber volume fraction, contact angle, and Bond numbers. It is found that gravity affects only the final stage of the impregnation process. Permeability of the fiber bed is obtained using Darcy's law and the fluid front velocity from the calculation. Anisotropic transverse permeability of a fiber bed due to different fiber arrangement pattern is discussed and compared with the longitudinal permeability. Permeability prediction using lubrication model is discussed. It is found that when fiber volume fraction reaches a certain level, the equation for the calculation of permeability needs to be reconsidered. An extension of the lubrication is suggested. Permeability for different fiber arrangement pattern is discussed and presented.

Nomenclature

ρ: Density

α : Contact angle

μ : Dynamic viscosity

θ : Inclination angle

σ : Surface tension

θ_d : Dynamic contact angle

θ_s : Static contact angle

β : Fiber packing angle

b : Half channel width of a vertical channel

Bo: Bond number

Contact angle in the calculation of fiber bed impregnation

d : Half of the closest distance between fiber surfaces

d_1 : Half of fiber separation distance within one layer

d_2 : Fiber separation distance between two adjacent layers

dQ: flow volume in time dt

e : Void fraction

g : Gravitational constant

h : Half channel height of a horizontal channel

Half of fiber separation distance

K: Permeability

L : Half channel width of a inclined channel

n : Ratio of the length of two sides of a rectangular packing

P: Pressure

P_{ex}: External pressure

Q: Volume flow rate

r: Radius of fiber

R: Radius of the cylinders that form the flow channel

R_1: Radius of curvature

r_1: Radius of curvature of the free surface during impregnation

R_2: Radius of curvature

t : Time

v: Impregnation velocity

Vertical impregnation distance

v_f: Fiber volume fraction

x: Impregnation distance

Chapter 1 INTRODUCTION

1.1 Capillary Flow in Porous Media

Since early time of this century, capillary driven flow in porous media has generated considerate interest in researchers and engineers because of its numerous applications in various fields such as soil mechanics and petroleum engineering. In soil mechanics, humidity distribution in the soil plays an important role in guiding agricultural activities. In petroleum industry, the physics of immiscible water/oil displacement in porous media is a major concern to waterflooding of oil reservoirs. The dynamics of capillary flow is affected by two factors: capillary forces that drive the flow and the resistant forces to the flow generated by the medium. Capillary forces come from the "liquid bridge" between the solid surfaces in the medium. The resistance forces come from the viscous forces during the flow. Such resistance forces depend on the geometric structure of the medium and fluid properties.

In recent years, the development of fiber reinforced composite materials brings new topics to research of fluid flow in porous media. The microstructure of such materials is formed by some certain arrangements of cylindrical-shaped fibers connected by the flow of molten polymer and the later curing of such polymer. The mechanical properties of such materials are highly dependent on the microstructure characteristics, such as fiber volume fraction, fiber orientation as well as pore distribution, of the material. Flow of polymer in between fibers supplies connection between fibers such that the designed properties can be obtained. Since fibers are structurally anisotrpic, the resistance force to the flow is anisotropic. Such resistance force changes with fiber volume fraction, fiber arrangement pattern, and flow direction. On the other hand, capillary forces driving the flow also change with fiber arrangement pattern as well as fiber volume fraction. Studying the dynamics of polymer flow is important in quality control, cost estimation, and efficiency control of the manufacture process.

Fluid front shape plays an important role in the research of the dynamics of capillary driven flow. The value of the capillary forces depends on the shape of the free surface that exists between cylindrical fiber surfaces. The location and shape of the free surface affects the flow dynamics through the pressure jump generated across the free surface. If the flow stops, the existence of the free surface balances the static pressure on both sizes of the surface. In order to understand the dynamics of capillary flow in a fiber bed, one needs to have knowledge of both static free surface shape and dynamic change of the free surface during the flow.

1.2 Static Free Surface Shape

A drop of mercury on a plane surface has a spherical shape. A drop of water, on the other hand, has a different shape. Fluid in a container has a convex or concave free surface, depending on the fluid kind. All these are examples of static free surfaces caused by the surface tension force. The shape of the fluid surface is governed by the balance of hydrostatic pressure with capillary pressure generated by the curvature of the free surface and surface tension of the fluid.

Pressure balance across a free fluid surface is described by Laplace equation (1805). Laplace's equation relates the principal radii of curvature of a free surface with the pressure difference across the surface and the surface tension of the fluid. In general, Laplace equation is a high order, nonlinear differential equation that needs to be solved with appropriate boundary conditions. These boundary conditions are the contact angles at the contact line of fluid with solid surface.

Contact angle is considered as changing with the fluid type, wall material and the roughness of the wall. It represents the force balance between different media. When a free fluid surface adheres to a solid surface, contact angle is related to the surface tension force of different media as:

$$\cos\alpha = \frac{\sigma_{as} - \sigma_{fs}}{\sigma_{af}}. \tag{1.2.1}$$

where σ_{as}, σ_{fs}, σ_{af} are the surface tension force between air and solid wall, fluid and solid wall, and air and fluid; respectively. They change with fluid property, toughness of the wall, and temperature.

Because of the complexity of Laplace equation itself as well as the shape of different containers, analytical solution for Laplace's equation can only be obtained for some special cases. One of such special case is that gravity effect is absent so the free surface shape is spherical. The other special case is that the fluid is held between two horizontal walls. Most of the time, free surface shape is solved using mathematical approximation or numerical method.

Early study focused on the two-dimensional axisymmetric free surface shape. Concus (1968) solved the free surface shape in a circular tube by expending Laplace equation by the power of Bond number (the dimensionless ratio of gravity to capillary forces) in a cylindrical coordinate system. Solution of free surface shape for small and large Bond numbers are obtained by picking the dominating terms in the expansion. For intermediate value of Bond number, shooting method was used to solve the free surface shape. Padday and Pitt (1972) classified the symmetric free surfaces into to categories: the bounded surface and unbounded surface. Bounded surfaces refer to liquid drops or bridges formed between two parallel plates. Unbounded surfaces refer to a small object withdrawn from an infinite reservoir or liquid bridges formed between a horizontal wall and an infinite reservoir. It is found that a bounded surface could be defined by a single parameter while an unbounded surface needed two parameters to define its shape. Orr and Scriven (1975) analytically solved the free surface shape between a sphere and a plate when gravity effect is negligible with a discussion of the possible appearance of singularity points and the stability of the free surface shape. Hartland and Hartley (1976) collected these early results of two-dimensional free surface shape and represented them in the form as family of free surface shapes. Later, Siekmann et al (1977) analytically solved the free surface shape in a horizontal channel. Siekmann (1979) also showed that the problem of free surface shape in a horizontal channel could be represented using the equation of motion of a simple pendulum oscillating with finite amplitude.

At the same time when these free surface in simple shaped containers were obtained, some free surface shape in complicated geometry were also studied. Using the balance of gravity with capillary forces, Princen (1968a, b, c) calculated the height and shapes of the free surfaces among cylindrical rods. Princen's calculations were two-dimensional and gravity effect to the free surface shape was neglected. Later, three-dimensional free surface shape in arrays of cylinders with gravity effect was obtained using finite element method (Orr and Scriven, 1975).

Recent works focus on the free surface shapes at corner or complex containers. Some special surface was also discussed, such as the free surfaces at the corners of some containers. Mason and Morrow (1983) experimentally studied the radii of free surfaces at the corner of capillaries with uniform cross-section such as rod in a tube or polygon tube. Manson and Morrow (1991) solve the free surface shape of perfectly wetting liquid in a triangular tube. Langbein (1995) obtained the approximate analytical solution of liquid surfaces in polyhedral containers.

Compared with axisymmetric free surface shape, the nonaxisymmetric free surface shape seems to be more difficult to obtain. Two kinds of nonaxisymmetric free surface shape were discussed in the literature. One of them is a liquid drop on an inclined plate. The other is the free surface of a liquid drop between two parallel horizontal plates. Either the inclination of the disks or the separation of centers of disks can cause the free surface shape to be nonaxisymmetric.

A liquid drop resting on a smooth plane is defined as sessile drop when the plane supports the drop in a direction against gravity. If the support from the plane is in the gravitational direction, the liquid drop is defined as a pendent drop. For a sessile drop on a horizontal plane, there is always a stable free surface shape. But if the plane supporting the liquid drop is inclined or the direction of gravity is changes such that the liquid drop becomes a pendent drop, one cannot always expect a stable drop shape. Lawal and Brown (1982) discussed the stability of sessile and pendent drops using finite element method. O'Brien (1991) proposed an asymptotic solution to the shape of a sessile or pendent drop. Drop surface is divided into interior, outer and neck regions for a pendent drop and inter and outer regions for a sessile drop. The solution for the free surface shape is obtained by composite the solutions in different regions. O'Brien's result was found to match with numerical calculation.

Free surface shape between two equal disks can become nonaxisymmetric if the two disks are not coaxial or a lateral gravity field applied exists. Different approaches have been tried to obtain the nonaxisymmetric free surface shape between two equal disks. Discussion of changing from axisymmetric shape to nonaxisymmetric shape was also performed. For an axisymmetric free surface between two equal disks, the volume of the fluid cannot be less than a critical amount depending on the ratio of disk radius to disk separation distance, according to Sanz and Martinez's experimental results (1982). In this work, gravity effect was neglected. Perales (1987) proposed an asymptotic solution to the nonaxisymmetric free surface shape based on the bifurcation techniques. Chen and Saghir (1994) used finite element method to numerically calculate the same free surface shape. Chen and Saghir's results were found to have good agreement with Perales's asymptotic solution except near the critical Bond number when the free surface becomes unstable. Slobozhanin and Perales (1993) discussed the same stability problem with gravity effect considered. It was found that a stable free surface could only exist between equal disks under certain range of fluid volume. If the fluid volume were less than the minimum required value, free surface would either break into two drops or detach from the edge of one of the disks. When fluid volume is greater than the maximum value of the range, the free surface would lose its axisymmetry. Laveron-Símavilla and Perals (1995) used finite difference method to solve the nonaxisymmetric free surface shape between two equal disks and the related potential energy. When the radius of the two disks are not equal, the free surface shapes were presented in the form of family of curves (Martinez and Perales, 1987)

Some other shapes of the free surface between various shapes of objects are also discussed. Huh and Scriven (1969) discussed the unbounded free surface shape formed outside a solid object in a fluid reservoir. Tallmadge (1971) discussed properties of the free surface such as curvature at the top of the surface and the effect of curvature on the height of the surface based on some previous published data. Analytical expressions for these properties were developed and compared with asymptotic expressions in the literature. Saez and Carbonell (1987) investigated shape and stability of a free surface between two touching cylinders aligned vertically. A general bifurcation analysis was developed from Laplace equation. It was found that the maximum fluid volume for a stable free surface changes with Bond number (a dimensionless parameter of gravity to capillary force) and contact angle. The influence of Bond number and contact angle to the shape and stability of the free surface were discussed. Serial papers by Wong et al (1992a, b) discussed free surface in some irregular shaped containers. Both theoretical and experimental works (Mason and Morrow, 1994) on fluid drainage in a pore formed by touching spheres show that change of contact angle has negligible effect on the curvature of the free surface. The contact line will move to a new position to balance the change of contact angle so that the curvature of the free surface remains the same. Kagan and Pinczewski (1996) obtained a closed-form analytical solution of free surface in a narrow slit.

1.3 Dynamics of Capillary Flow in Porous Media

1.3.1 Darcy's Law and the Permeability of Porous Media

Due to randomness of pore distribution in porous media, flow through a porous medium is highly dependent on the microstructure of the medium. Macroscopic study of such flow must include the characteristics of pore distribution in the medium. Darcy (1856) first proposed the macroscopic physical law of flow through porous media in the last century. Darcy's law is an empirical relation of flow velocity through a porous medium related with pressure difference across the medium and fluid properties. The property of the medium is represented by a physical parameter called the permeability of the medium. Darcy's law predicted the linearity of flow velocity with pressure gradient across the medium. Later works (Kozeny, 1927; Carman, 1937) made use of Darcy's law and proposed the concept of hydraulic radius of the medium that represented the ratio of cross-sectional area normal to the flow to the perimeter presented to the fluid. Permeability of a certain porous medium is a function of porosity, cross-sectional area of the medium, hydraulic radius, and an experimental constant defined as KC constant. KC constant was thought to be unchanged within certain limit of porosity. The concept of hydraulic radius proposed a method to predict the permeability of a porous medium without voluntarily repeating experimental measurements.

Permeability of a porous medium depends on the porosity and orientation of the pores within the medium. Up to date, various methods of obtaining permeability have been proposed, yet the most efficient and accurate way to obtain permeability data is still through experimental measurement. Flow rate and pressure are easy to measure experimentally. By making use of the linearity proposed in Darcy's law, permeability of a porous medium can be easily obtained. By using Kozeny and Carman's model, permeability of a certain kind of porous media can be predicted without repeating works. For such reason, Darcy's law and Kozeny and Carman's model is widely used in various fields (Williams et al, 1974; Kececioglu and Jiang, 1994; Thies-Weesie and Philipse, 1994; Cai, 1992; Leverett).

1.3.2 Capillary Tube Model

Dynamics of fluid flow through porous media depends on fluid properties, pore distribution, and the driving forces to the flow. If the contact angle between the fluid and the solid surface is less than 90 degrees, the fluid wets the surface and impregnates the porous medium upon contact. Such flow is driven by capillary pressure generated from the curvature of the free fluid surface. Washburn (1921) first studied a general pressure driven creeping flow in a circular tube. His work predicted that during capillary flow in a circular tube, the length of the fluid column changes linearly with the square root of time. Washburn's results haven been the starting point for most of the modern research on flow through porous media.

The slope of the straight line proposed by Washburn is proportional to the cosine of the contact angle between fluid and the solid surface. The ratio of the slopes was used to obtain the contact angle of carbon blacks (Studebaker and Snow, 1955). Washburn's equation is based on macroscopic analysis of free surface motion. If molecular motion is considered, some certain correction might be introduced to the fluid motion analysis. Good (1972) generalized Washburn's equation by analyzing motion of fluid molecules ahead of the liquid front during fluid flow through porous media. Good's analysis led to the proposal of the expression for maximum time-dependent possible velocity during the flow. Contact angle represents the intermolecular action between fluid and solid surface. Contact angle can be different when the properties of either the solid wall or the fluid is changed. Bruil and Aartsen (1974) studied the contact angle change due to the appearance of aqueous surfactant solutions to powders. Each time when different density of the surfactant solutions was applied, the slope of the straight line predicted by Washburn was measured. Change of contact angle is observed by comparing the change of this slope.

The linearity predicted by Washburn's equation has been used extensively in the analysis of flow through porous media. Levine and Neale (1975) used rigid body analysis to the same fluid flow problem as Washburn. Their result of capillary climbing with gravity was in the form of serial expansion. When gravity effect is neglected, the linearity predicted by Washburn was observed. Yang et al (1988) experimentally verified the linearity of Washburn's prediction by the capillary impregnation into monodisperse spherical beads. Kolosov (1988) converted the structure of a fiber bed into an equivalent capillary tube. The geometry of such fictitious tube is then used to calculate capillary flow through the fiber bed. Capillary impregnation of a fiber bed studied by Ahn and Seferis (1991) introduced a shape factor to characterize flow in different directions. Bayramli and Powell's (1991a) numerical calculation of capillary flow through a fiber bed showed both microscopic and macroscopic behavior of the fluid fronts during the flow. It was shown that while fluid front's motion followed a straight line macroscopically, the microscopic fluid front motion shows a periodical characteristic. Bayramli and Powell's experiments (1991b) of flow along fiber axis supplied a method to calculate the effective capillary radius of a certain porous medium. Hodgson and Berg (1988) studied the effect of surfactants on the wicking flow in fiber beds. It was found that surfactants could change the value of capillary forces such that the flow dynamics changed. In all the experiments, the linearity is found to hold during wicking process.

Washburn's equation works for fluid motion in vertical or horizontal direction. Similar work was done for radical fluid motion. Using the same assumption as Washburn for flow penetration into porous media, Marmur (1988) developed the differential equation for a fluid drop penetrating radically into a porous medium. This differential equation includes the radius of the fluid drop in the analysis of flow dynamics. If the flow is from an infinite fluid reservoir, an approximate analytical solution is developed. Later experimental works (Danino and Murmur, 1994; Borhan and Rungta, 1993) verified Murmur's theory.

Washburn's equation describes fluid motion in a single circular tube. When this equation is used in analysis of flow in some real media such as rocks and sands, it was found that a single tube model might not be enough. Based on this observation, some multi-tube models have been proposed. Sorbie et al (1995) studied capillary motion into a pair of wide/narrow pores and developed an analytical solution to such problem. This doublet pore model was found to work better in waterflooding into petroleum reservoir than the single capillary tube model from Washburn. Marmur and Cohen (1997) characterize a porous medium as an assembly of capillaries with different radii. The relevant capillary radius at each time dominates the rate of fluid penetration.

Different researchers have discussed validity of using Washburn's equation. An important assumption of Washburn's study is that inertia force effect is negligible during the flow. If this condition is not satisfied, using Washburn's equation in flow analysis is invalid. Dreyer et al (1994) studied various forces during the capillary flow between parallel plate and compared their analysis with experimental data. The total time domain was divided into three sub-domains depending on the forces that dominated: inertia dominated domain, convective forces dominated domain, and friction dominated domain. Friction dominated domain is longer during the flow compared with the other. It is found that Washburn's equation works only for friction dominated domain. Washburn's equation assumes that the free surface shape is circular so that the capillary forces can be easily calculated. Tilton (1988) used Galerkin finite-element method to study interface motion in a capillary tube under different capillary numbers (a dimensionless parameter of the ratio of viscous force to capillary force). It was found that interfacial shape deviate from a circular one at large capillary numbers. Since Washburn's equation doesn't include gravity effect, one can not expect to obtain the flow behavior as the free surface approaches its final position. Some alternative method needs to be employed. Trutschel and Schellenberger (1998) assumed that fluid reaches its final position by a small amplitude damping. This damping is calculated by assuming initially a plain surface and its subsequent damping using Galerkin finite element method simulation. Some other effect to fluid flow such as geometric variations perpendicular to the flow direction was discussed by Borhan et al (1991) using flow between two sinusoidally corrugated plates in a gravity field.

1.3.3 Dynamic Contact Angle During Capillary Motion

An important issues regarding the dynamics of fluid motion is the contact angle at the contact line between fluid and solid. Especially if capillary forces drive the flow, dynamic contact angle changes the value of forces that drive the flow. Dynamic contact angle was found a function of static contact angel and capillary number. Different branches of research exist in the modification of dynamic contact angle.

The appearance of dynamic contact angle has been experimentally observed for a long time. Theoretical analysis had not been done until Dussan and Davis (1974) proposed a basic assumption on rolling of the free surface basic on some simple experimental evidences. Using the traditional non-slip boundary condition to solve the free surface motion problem, one would come up with the appearance of singularity at the solid wall. In order to correct such singularity of flow analysis, Dussan (1976) proposed a model that relaxed the traditional non-slip boundary condition at a region defined as "inner region" near the contact point. The technique of matching asymptotic solutions at different regions was used to obtain flow solution in the whole region of interest. Huh and Mason (1977) used the model of relaxing non-slip boundary condition at inner region of motion and calculated pressure driven flow in capillary tube. A corrected Washburn's equation was proposed accounting for dynamic contact angle and reveals the importance of slippage. Kafka and Dussan (1979) pointed out the dependence of dynamic contact angle on the geometry of flow. It was pointed out that even though experimental measurement of dynamic contact angle could be used in the macroscopic analysis of contact line motion, it is not enough to study the physics of free surface flow. Later experimental work by Ngan and Dussan (1989) experimentally verified the validity of imposing the slip boundary condition to the inner region. Ngan and Dussan didn't directly measure contact angle of the free surface. Instead, an alternative procedure of measuring the apex height to convert it to contact angle is developed. More recently, experimental works that can measure contact angle (Dussan et al, 1991) obtain similar results. Petrov and Sedev (1993) experimentally measured dynamic contact angle and compared with different approaches to theoretically obtain dynamic contact angle value: from dynamic capillary height via corresponding static relationship or extrapolated from dynamic meniscus profile. It was found that neither of these approaches represents the real dynamic contact angle. A hydrodynamic deformation exists close to the contact line. The thickness of such deformation region varies with maximum static capillary height. A different method to study the dynamics of free surface flow is to relax constant surface tension condition. Shikhmurzaev's study of contact line motion on a smooth surface (1993) and in liquid/liquid/solid system (1997) studied the contact line motion by relaxing the condition that surface tension is a constant. Instead, a surface tension gradient is introduced. Free surface region is divided into three sub-regions according to the serial expansion of Navier-stokes equation. The technique of matched asymptotic expansions is used in the solution of free surface flow. The resulting dynamic contact angle as a function of free surface velocity and other relevant parameters is compared with experimental result from Fermigier and Jenffer (1991). Thompson and Robbins's experiments (1989) confirmed that the slip boundary condition existed in microscopic length scale while the traditional non-slip boundary condition was valid macroscopically.

Besides the theoretical studies mentioned above, dynamic contact angle is also observed experimentally. Change of dynamic contact angle with capillary was studied and graphically presented by Huffman (1975). These data were later organized and presented dynamic contact angle as a function of capillary number by Jiang et al (1975). Experimental Study of dynamic contact angle on smooth and rough surface (Cain et al, 1983) suggested that dynamic contact angle increases with the velocity of flow. It was found experimentally (Rame and Garoff, 1996) that for small capillary number (from 10^{-3} to 10^{-1}), static capillary can describe the free surface shape, while in a microscopic length scale a viscous deformation region exists that is a function of capillary number. While capillary number is a major influence to dynamic contact angle, it is possible that intermolecular force also contributes to the dynamic contact angle. Kalliadasis and Chang's experimental (1994) work showed that the intermolecular force is weak in the influences to the dynamic contact angle. Lee and Chiao (1996) verified jiang et al's proposal experimentally by measuring the microscopic dynamic contact angle on a needle inserted into glycerin and epoxy resin. More recent, Ishimi and Slattery (1998) suggested an approximate analytical method to calculate the advancing fluid front motion. Their calculation as well as experimental data showed agreement with Jiang et al's results. Remoortere and Joos, (1991) compared different proposals regarding the dynamic contact angle as a function of capillary number. It was found that the difference among these is small for small capillary numbers.

1.3.4 Permeability of a Fiber Bed

The aim of dynamic analysis of capillary motion is to guide the manufacturing process. During manufacturing of fiber reinforced composite materials resin flow through fiber lattice and later solidified by external pressure and heat. Resin flow follows the rule of fluid flow in porous media. The most convenient way to industrial process is still make use of Darcy's law. Thus the permeability of the fiber bed becomes a critical parameter for the design of manufacturing process. Using various model of fluid flow in porous media above, the permeability of a fiber bed can be obtained. Since permeability of a fiber bed should be a material property of the medium. It should be independent of the fluid property, flow characteristics as well as analyzing method. Theoretically, permeability of a fiber bed can be obtained by either analyzing capillary motion with Washburn's equation or obtaining pressure jump across a unit cell of fiber arrangement and calculating permeability with Darcy's law. Besides these, experimental measurement remains an important method to measure permeability as well as verify permeability data from theoretical analysis.

Permeability, a physical property of fiber bed, is a function of fiber arrangement. The resistance to the flow depends on the permeability of the fiber bed and fluid properties. To obtain the value of such resistance force or permeability for fiber beds with different microscopic structure, proper physical models need to be used. Happel (1959) used the idea of cell model in flow field analysis to obtain resistance of a single fiber to the surrounding flow. This model was later used by different mathematical treatment of the flow equation to study the resistance flow of different fiber beds (Hashimoto, 1959; Sangani and Acrivos, 1982a, b; Drummond and Tahir, 1984; Clague and Phillips, 1997). Berdichevsky and Cai's (1993) calculation using self-consistent method and finite element simulation obtained similar result as Sangani and Acrivos and early work of Happel. Keller (1964) introduced lubrication model in the resistance force calculation of fiber bed. It was later used to calculate the resistance force in a fiber bed when fibers are closely arranged. Both approximate and analytical expressions of permeability were obtained (Gebart, 1992; Bruschke, 1992). Sadiq et al's experimental data verified Bruschke's prediction for fiber volume fraction range of 60-75%. Lubrication model in permeability prediction has gain vast experimental evidences (Astrom, 1992). Using the lubrication model, permeability change due to disarrangement of fibers was also studied. Cai and Berdichevsky (1993) used finite element method to study resistance to flow in hexagonal and square packing due to the absence of fibers. It was shown that resistance force decreases when some fibers are removed from the bed. Lundstrom and Gebart (1995) studied the variation on permeability due to inconsistency of fiber radius and the removal of fibers from a certain arrangement. Even though the cell and lubrication model works well for regularly arranged fiber bed, it can not be used for fiber bed when fibers are randomly arranged. Sangani and Yao (1988a, b) used the technique of calculating the thermal conductivity based on the computer generated random arrangements to calculate friction forces to flow through randomly arranged cylinders. Such friction forces were then converted to the permeability of the fiber bed. Randomness in fiber placement was found to increase permeability only in high porosity (<0.8) (Papathanasiou and Lee, 1997) using boundary element method.

In general, fiber bed is structurally anisotropic. Permeability of a fiber bed is related to the flow direction as well as fiber arrangement. Larson and Higdon (1987) numerically calculated the flow field in hexagonal and cubic fiber arrangement cell with different flow directions. Their results show that the flow field changes dramatically when flow direction is changed. Larson and Higdon (1987) also calculated the anisotropic in-plane permeability by changing the cross-sectional shape of the fiber from circular to ellipsoid. Their results show that the principle permeability of a fiber bed changes with the ratio of the two principal axes of the ellipses and the inclination angle of the packing. Bruschke and Advani (1990) proposed a finite element approach to mold filling in anisotropic porous media. This model allows the change of permeability in magnitude and direction throughout the medium. Fluid front at equal time steps are predicted and appeared to agree with experimental observation.

Experimental method of permeability measurement includes unidirectional and radial flow measurement. Unidirectional flow can measure permeability in the appointed direction. The experimental setup as well as data acquisition is simple. But the anisotropy of the permeability can not be observed. Radial flow, on the other hand, clearly presents the anisotropy of the permeability. Its experimental setup and data acquisition is more complicated compared with unidirectional flow measurement. Gauvin and Chibani (1990) used the unidirectional flow to study permeability of non-woven reinforcement. In this study, Lamb theory was used to obtain shear flow loss and drag forces on the rovings. Such resistance to flow was later converted to permeability. Adams and Rebenfeld's (1991a) used a group of unidirectional flow measurement to obtain the in-plane permeabilities of one layer of reinforcement with fibers unidirectionally or randomly arranged. The anisotropy of the permeability is shown when fibers are unidirectionally arranged. Seo and Lee (1991) used experimental data from Gutowski in predicting permeability of a fiber bed. They developed flow of power-law fluid through fiber bed. Experimental data showed good agreement with theoretical prediction. Kim and McCarthy's (1991) experimental results showed the dependence of permeability on fiber orientation and fiber volume fraction. Gebart and Lidstrom (1996) measured the in-plane permeability tensor by simultaneously placing parallel mold cavities to different directions relative to the injecting flow. They found that the permeability could change to as much as 23 times when the direction of flow changes 90 degrees. Ferland et al (1996) developed a simple method to measure in-plane permeability. A built-in Darcy's law is developed so that one can calculated the permeability by observation of fluid front motion and pressure change with time. Woerdeman et al (1995) suggested an approximate method to relate permeability tensor to a set of permeability measurement in different flow directions. A robust binary search algorithm is used to solve the non-linear equations resulted from general Darcy's law using permeability tensor. Permeability measurement using radial flow was performed by Chan et al (1993). In this work, the principal direction of in-plane permeability was obtained by observing the extreme axes of the fluid front ellipse. The value of the principal permeability was calculated using Darcy's law and time rate change of the extreme axes of the fluid front. Similar measurements were performed by others (Gauvin et al, (1996); Robitaille et al). Parnas and Salem (1993) compared experimental results from one-dimensional flow and radial flow through woven composite reinforcements. Fluid front motion clearly shows an elliptical shape with its principle axis agrees with the measurement from one-dimensional result. Lai et al's (1997) experimental results showed that permeability difference between unidirectional and radial flow measurement is within 10%.

For multi layer of fibers, permeability and thickness of each layer affect the overall permeability. Total thickness of the whole fiber mat during the process of the composite materials. Such compression also brings changes to the permeability. Permeability and compressibility of fiber mats were experimentally measured (Trevino et al, 1991). This result was then used (Young et al, 1991) to numerically calculate fluid front motion during resin injection molding. Good agreement was fund between numerical calculation and experimental observation. Adams and Rebenfeld proposed a semipermeable wall model (1991b) to analyze flow through multilayer fiber reinforcements. Parnas et al measured (1995 a, b) permeability of multilayer preforms formed by 3-d woven fabric and random mat. It was shown showed that the permeability of a 3-d woven could be one order of magnitude lower than that of a random mat. Overall, permeability data starts from a higher value at the beginning of the measurement and decrease to a lower and steady value. Experimental work with multiple layers didn't give quantitative agreement with theoretical prediction, but gave the same trend. Calado and Advandi (1996) developed a simple model to predict the effective average permeability of multilayer beds that account the in-plane permeability, transverse permeability, and thickness of each layer as well as total length of the mold. This model allows one to calculate the fluid front difference between layers easily by a two-dimensional finite element approach. Mogavero and Advani's permeability measurement with multi-layer fiber bed (1997) show that prediction of permeability based on weighted average scheme can give reasonable accurate (24% error) result for moderate thickness of each layer. If the thickness is big in some layer, some nonlinear pressure behavior appears. Weighted average scheme is no longer valid. Processing of composites under pressure changes the thickness of fiber mats that in turn changes permeability. Lakakou et al's study (1996) pointed out that the variation in permeability of multilayer fiber mats are mainly due to the change of porosity. The result suggests that an empirical constant needed in analyzing permeability of multi layer fiber mats.

Normal flow visualization technique is applicable for isotropic or orthotropic permeability measurement. For more complex permeability measurement, imbedded fiber optic technique is introduced by Ahn et al (1995). This method imbeds fiber optic in the preform to monitor fluid front motion. Principal permeability is obtained by analyzing the axis of the ellipsoid fluid front surface. Fiber bed consist of unidirectionally packed permeable cylinders with elliptical cross-sectional shape is studied (Ranganathan et al, 1996). It was found that packing pattern, packing angle as well as the cross-sectional characters influence the permeability of the fiber bed. Rudd et al (1996) proposed a model to predict in-plane permeability due to geometric deformation of fiber beds.

Permeability is a function of fiber arrangement. If fiber bed undergoes shear deformation, fiber volume fraction changes therefore permeability will change. This change of permeability was experimentally investigated by Lai and Young (1997). It was found that the angle shift of the principal axis increases with shear angle and the in-plan permeability decreases with shear angle. Hristopulos and Christakos (1997) studied effective permeability of heterogeneous media using the replica-variation approach.

Permeability of a fiber bed changes with fiber arrangement and later process of fiber mats. For industrial purpose, a general database has been developed containing the permeability results of glass fibers from carefully controlled experiments (1997).

1.4 Scope of This Dissertation

This work investigates microscopic fluid front motion during capillary impregnation of a fiber bed. Fluid front shape and location is solved at different times of capillary impregnation. Permeability prediction is obtained and compared with the ones from using lubrication theory. The anisotropy of the permeability of a fiber bed is discussed. Some experimental data in the literature is compared with the results obtained in this study.

Chapter 2 solves the free surface shape in a two-dimensional channel. Laplace equation is first separated into two second-order differential equation that can be solved numerically. A shooting method is used to obtain the final free surface shape. Different free surface shapes in a vertical channel for different Bond numbers and contact angles are obtained. Similar procedure is employed to solve the free surface shapes in inclined channels. For free surface shape in a horizontal channel, analytical solution is obtained and compared with numerical calculation. The critical Bond number for the existence of a stable free surface in a horizontal channel is discussed.

Chapter 3 studies capillary impregnation of a fiber bed with flow direction normal to the fiber axis. Fibers are simulated as hexagonally arranged cylinders. Governing equation for quasi-static creeping flow in a two-dimensional channel is used in the calculation. Gravity effect is included in the analysis. First, capillary flow in a uniform channel is investigated. Fluid front motion as well as the final position is obtained as a function of Bond number. Then, capillary impregnation of a fiber bed is calculated by separating the channel between two cylindrical fiber surfaces into small segments of uniform channels. Flow model of continuous and discontinuous fluid front motion is introduced. Results of this calculation show the free surface shape and location during the impregnation. The periodical change of flow velocity is also observed. Gravity effect is shown to affect the impregnation significantly only during the final stage of the impregnation. Permeability of such fiber bed is obtained as a function of fiber volume fraction. The permeability data are compared with the ones using lubrication model. It is found that there is a limit of fiber volume fraction for permeability prediction using lubrication theory.

Chapter 4 studies capillary of an anisotropic fiber bed and the prediction of the anisotropic permeability. Similar methods as in Chapter 3 in simulating fiber bed structure and the flow modeling are used. The structure of a fiber bed changes from a hexagonal to an isosceles triangular. Capillary flow from different directions is discussed. The criteria of possible capillary impregnation and impregnation by external pressure are developed. It is found that the permeability of a fiber bed could be change as much as one order of magnitude when flow direction is changed. The ratio of permeabilities decreases as fiber volume fraction increases. Similar as in Chapter 3, fluid front locations as well as shapes are obtained. Permeability data are found to agree with experimental results.

Chapter 5 studies the effect of external pressure to the impregnation and the theoretical prediction of fiber bed permeability. It is found that for a limited amount of external pressure added to the impregnation process, the capillary tube model can not be used in the study of the flow. Traditional way of permeability prediction using lubrication theory needs a correction when fiber volume fraction is high. A general expression of permeability is developed for different fiber arrangement patterns.

Chapter 2 STATIC FREE SURFACE SHAPE IN A TWO-DIMENSIONAL CHANNEL

2.1 Introduction

Static free surface shape represents the status when the various forces acting on the fluid are balanced. It is also the final stage of any kind of fluid motion. Understanding the shape of static fluid surface is the first step toward fluid front prediction during its motion.

When a fluid is at a static state, the height it can reach on the wall of its container depends on the vertical component of the capillary forces generated from the free fluid surface and the density of the fluid. The shape of the static free surface is the result of the balance among hydrostatic pressure of the fluid, atmospheric pressure, and capillary pressure. For a given gravity field, free surface shape is a function of surface tension of the fluid, contact angle between the fluid and solid wall, and the shape of container that holds the fluid.

The prediction of the static free surface shape and the discussion of the mathematical properties of the solution to free surface shape have been very active since early 60s. Free surface shape changes with the shape of the container as well as the orientation of the container. If the supporting forces from the bottom of a rectangular tank is in the direction of gravity, free surface shape can only exist under certain conditions (Concus, 1964). Similarly, free surface in a horizontal channel is stable only under limited combination of contact angles and Bond numbers (Siekmann, 1977). Under the condition that the free surface shape is stable, the shape of the free surface can be obtained using analytical or numerical methods. Concus' solution of free surface shape in a circular tube (1968) is a combination of both mathematical approximation and shooting method. Siekmann's prediction of free surface shape in a horizontal channel (1977) based on the analytical integration of Laplace's equation. For free surface shape in a complex geometry such as free surface among several cylinders, finite element methods was used in the prediction of the free surface shape (Orr and Scriven, 1975). In recent years, lots of research has been done on the free surface shape between two equal disks. Free surface shape changes with the orientation of the disks relative to gravity field as well as the slenderness of the gap between the disks (Perales, 1987). The volume of the fluid held between the disks also influences the shape and stability of the free surface. If the volume is smaller than a critical volume, the free surface can not be stable (Sanz and Martinez, 1982). If the volume is greater than the upper limit of the range, the free surface shape lost its axisymmetry (Slobozhanin and Perales, 1993).

This chapter investigates free surface shapes in a two-dimensional channel. The channel can be vertical, horizontal or inclined. Shooting method is used in the numerical calculation of free surface shapes in vertical and inclined channels. For free surface shape in a vertical channel, solutions for the free surface shape are presented for different Bond numbers and contact angles. For free surface shape in an inclined channel, solutions of free surface shape are presented for different inclination angles, Bond numbers and contact angles. For free surface shape in a horizontal channel, both analytical solution and numerical prediction are presented. Good agreement is found between the two methods. The critical Bond number for a stable free surface shape in a horizontal channel is obtained from the analytical solution.

2.2 Theory

Free surface in a container is the borderline between different media. Hydrostatic pressure of the fluid acts on one side of the surface, air pressure (or hydrostatic pressure of a different fluid) acts on the other side. The surface tension forces on the free surface balance the difference between these different pressures. The general mathematical expression for force balance on the free surface is Laplace's equation:

$$\Delta P = \sigma\left(\frac{1}{R_1} + \frac{1}{R_2}\right), \tag{2.2.1}$$

where ΔP is pressure difference across the free surface; R_1 and R_2 are the principal radii of curvature of the free surface; and σ is the surface tension of the fluid. In order to solve the free surface shape, Eq. (2.2.1) needs to be converted to the expression using the coordinates of the free surface. In a Cartesian coordinate system, a three-dimensional surface can be represented by the equation:

$$z = f(x, y). \tag{2.2.2}$$

The sum of the curvature of such surface can be expressed in terms of the gradient of the function $f(x, y)$ as:

$$\frac{1}{R_1} + \frac{1}{R_2} = \nabla \cdot \frac{\nabla f}{\sqrt{1 + (\nabla f)^2}}, \tag{2.2.3}$$

where ∇f is the gradient of the function f and $\nabla \cdot$ represents the divergence of a vector. So the coordinates $(x, y, f(x, y))$ of the points on the free surface satisfies:

$$\Delta P = \sigma \nabla \cdot \frac{\nabla f}{\sqrt{1 + (\nabla f)^2}}. \tag{2.2.4}$$

The expression of the pressure difference across the free surface depends on the relative location of the free surface to the origin of the coordinate system. If the origin of the coordinate system is set at the free surface of the fluid reservoir, Eq. (2.2.4) becomes:

$$\rho g f = \sigma \nabla \cdot \frac{\nabla f}{\sqrt{1+(\nabla f)^2}} . \tag{2.2.5}$$

Equation (2.2.5) represents the general requirement for the coordinates of all the points on a free fluid surface. Besides this condition, the free surface shape should also satisfy the boundary conditions at the wall of the container. These boundary conditions are: the points on the free surface should also satisfy the equation for the surface of the container; free surface and the container form an angle that is the contact angle between the fluid and solid wall. Suppose the equation for the surface of the container is:

$$\psi(x,y,z)=0, \tag{2.2.6}$$

then the points (x, y, f(x, y)) should satisfy:

$$\psi(x,y,f(x,y))=0, \tag{2.2.7}$$

on the contact line of free surface with the container. Satisfactory to the contact angle condition can be expressed using the dot product of the norm to the two surfaces at the contact line as:

$$\cos\alpha = \pm \frac{-(\partial f/\partial x)(\partial\psi/\partial x)-(\partial f/\partial y)(\partial\psi/\partial y)+\partial\psi/\partial f}{\sqrt{1+(\nabla f)^2}\,|\nabla\psi|} . \tag{2.2.8}$$

Generally speaking, solving free surface shape is to find the solution of Eq. (2.2.5) that can satisfy Eqs. (2.2.7), and (2.2.8) on the contact line. Analytical solutions can be obtained only under some special conditions. One of them is that when gravity effect is absent. The absence of gravity makes the left-hand side of Eq. (2.2.5) to be zero. If one of the radii of curvature is infinity, as for free surface in a infinite channel, the curvature of the free surface becomes a constant. This refers to a circular free surface that can be easily obtained analytically from the geometry of the channel.

The forces acting on the free surface are capillary forces and gravity force. Thus free surface shape is different for different capillary and gravity conditions. A dimensionless parameter, Bond number, is introduced to represent the ratio of gravity force to surface tension. Bond number is defined as:

$$Bo = \frac{\rho g L^2}{\sigma}, \tag{2.2.9}$$

where L is a characteristic length. Besides Bond number, contact angle and the geometry of the channel also changes free surface shape. In the following calculations, all the solutions of the free surface shapes are expressed for different Bond numbers and contact angles. Since static free surface shape with a contact angle greater than 90 degrees is only the mirror reflection of the free surface shape with its supplementary angle, only contact angles less than 90 degrees are used in this study. All the free surface shapes are in a two-dimensional channel. The channel could be vertical, inclined and horizontal. For an inclined channel, inclination angle is also included as a parameter to the solution.

2.3 Free Surface Shape in a Vertical Channel

Before actually solving free surface shape in a vertical channel, a proper coordinate system needs to be set up. Figure 2.1 shows the coordinate system and the relevant parameters used in the analysis. The channel is infinite in the y direction so the free surface shape becomes two-dimensional. w is half channel width. For such free surface, one of the principal radii becomes infinity (here R_2 is set to be infinity). The dimensionless Bond number is defined as:

$$Bo = \frac{\rho g w^2}{\sigma}. \tag{2.3.1}$$

Free surface shape can be represented by the curve formed by the intersection of free surface with the plane y=const. Equation (2.2.3) is expanded in a Cartesian system as:

$$\frac{1}{R_1} = \frac{\dfrac{dx}{ds}\dfrac{d^2z}{ds^2} - \dfrac{dz}{ds}\dfrac{d^2x}{ds^2}}{\sqrt{[(dx/ds)^2 + (dz/ds)^2]^3}}, \tag{2.3.2}$$

where s represents arc length of the curve. If Eq. (2.3.2) is plugged into Eq. (2.2.5), one comes up with a high order, nonlinear differential equation as:

$$\rho g z = \frac{\dfrac{dx}{ds}\dfrac{d^2z}{ds^2} - \dfrac{dz}{ds}\dfrac{d^2x}{ds^2}}{\sqrt{[(dx/ds)^2 + (dz/ds)^2]^3}}. \tag{2.3.3}$$

Equation (2.3.3) is still difficult to solve either numerically or analytically. It needs some simplification before one could obtain the solution of the free surface shape. The simplification is done by making use of the angle β, the angle that the free surface makes with x axis at each point of the curve (see Fig. 2.1). The first derivatives in Eq. (2.3.3) are related with angle β as:

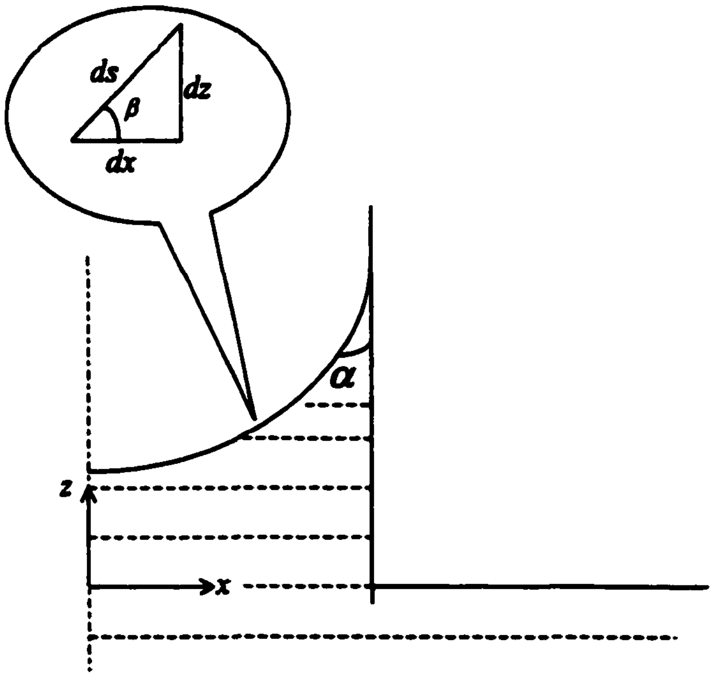

Figure 2.1 Coordinate system and the relevant geometric parameters used in the calculation of free surface shape in a vertical channel.

$$\sin\beta = \frac{dz}{ds}, \quad (2.3.4)$$

$$\cos\beta = \frac{dx}{ds}. \quad (2.3.5)$$

Equations (2.3.4) and (2.3.5) are then differentiated with respect to s to get:

$$\frac{d^2x}{ds^2} = -\sin\beta\frac{d\beta}{ds}, \quad (2.3.6)$$

$$\frac{d^2z}{ds^2} = \cos\beta\frac{d\beta}{ds}. \quad (2.3.7)$$

Equations (2.3.4)-(2.3.7) can be plugged into Eq. (2.3.3) to obtain:

$$\rho gz = \frac{d\beta}{ds}. \quad (2.3.8)$$

In this equation, the change of angle β with respect to arc length is related with the hydrostatic pressure of the fluid. Equation (2.3.8) is then plugged into Eqs. (2.3.6) and Eq. (2.3.7) to obtain two coupled differential equations as:

$$\frac{d^2x}{ds^2} = -\sin\beta\,\rho gz, \quad (2.3.9)$$

$$\frac{d^2z}{ds^2} = \cos\beta\,\rho gz. \quad (2.3.10)$$

Equations (2.3.9) and (2.3.10) are still in dimensional form. In order to show the general solutions of the free surface shape, it is customarily to nondimensionlize the equations before actually solving them. Equations (2.3.9) and (2.3.10) are nondimensionlized using the following parameters:

$$\xi = x\sqrt{\frac{\rho g}{\sigma}}; \quad (2.3.11)$$

$$\zeta = y\sqrt{\frac{\rho g}{\sigma}}\,; \tag{2.3.12}$$

$$\tau = s\sqrt{\frac{\rho g}{\sigma}}\,. \tag{2.3.13}$$

Equations (2.3.9) and (2.3.10) are then become nondimensionlized as:

$$\frac{d^2\xi}{d\tau^2} = -\frac{d\zeta}{d\tau}\zeta\,, \tag{2.3.14}$$

$$\frac{d^2\zeta}{d\tau^2} = \frac{d\xi}{d\tau}\zeta\,. \tag{2.3.15}$$

Since the direction of gravity is the same as the axis of symmetry of the channel. The free surface shape is also symmetric. The symmetric condition and the contact angle condition on the channel walls are used as the boundary conditions for the solution of Eqs. (2.3.14) and (2.3.15). These boundary conditions are:

When $\xi = \sqrt{Bo}$; $\frac{d\xi}{d\tau} = cos\,\alpha$, $\frac{d\zeta}{d\tau} = sin\,\alpha$;

When $\xi = 0$; $\frac{d\xi}{d\tau} = 1$, $\frac{d\zeta}{d\tau} = 0$,

where α is the contact angle. It can be seen from the above boundary conditions that the height of both the contact point on the channel walls and the point on the axis of symmetry are unknown. To solve the shape of the curve satisfying both boundary conditions, a shooting method is used in the numerical calculation. Figure 2.2 shows the concept and steps of calculation using the shooting method. Two widely separated points (points A_i and A_{i+1} in Fig. 2.2) are picked to solve for the curve shape. The boundary condition at the channel wall is used to find the next point of the solution

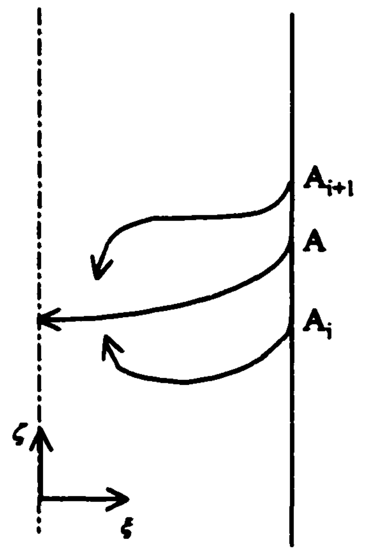

Figure 2.2 Iterations of shooting method in the numerical calculation of free surface shape.

curve. Equations (2.3.14) and (2.3.15) are used to solve the first derivative on the next point. When the first derivative on the next point is found, the third point on the curve can be solved. Such iterations are repeated to solve the shape of the whole curve. The resulting curves are examined during the integration procedure to determine the directions in which the two curves turn away from the axis of symmetry. If the two curves turn to different directions, the solution of the free surface shape is enclosed in the range bounded by the two initial points. The middle point of the range is picked to start a new curve calculation and examine its direction in which it turns away from the axis of symmetry. A new range can be obtained that contains the final solution. Such an iteration is repeated until the final solution is found. If, on the other hand, two initial points turn to the same direction, one of the points needs to be replaced until a proper range of initial points is found. Then the above procedure of integration is used to find the curve shape.

Solutions of free surface shape in a two-dimensional vertical channel are numerically calculated for different Bond numbers and contact angles. Arc length $d\tau$ is used as an intermediate parameter in the calculation. Different arc lengths are used and the resulting curves are compared. It was found that the resulting curves appear identical when the arc length is shorter than $0.001 * \sqrt{Bo}$. Such an arc length is used in all the calculations. At the axis of symmetry, the angle β should be zero to satisfy the axisymmetric condition. In this study, a criterion of $sin\,\beta \le 0.01$ is used at the point nearest to the axis of symmetry. Such criterion means that the angle of the free surface with x-axis is less than 0.57 degrees.

For different Bond numbers, the free surface shape solutions are at the different heights in the channel. In order to compare the effect of Bond number on the final shape of the free surface, the origin of the coordinate system is moved to a new position. The ζ coordinate of the new origin is:

$$\zeta_0 = \frac{1}{\sqrt{Bo}} \int_0^{\sqrt{Bo}} \zeta \, d\xi . \tag{2.3.16}$$

Figure 2.3 shows the free surface shapes in a vertical channel when contact angle is 30 degrees. With the Bond number changes from 0.001 to 1000. The effect of Bond number on the surface shape can be observed. Increase in Bond number flattens the free surface shape. The Bond number represents the ratio of gravity to capillary force. The static free surface shape is the balance of capillary forces that pulls up the liquid column and gravity force that pulls down the liquid column. A larger Bond numbers results in a decrease in the amount of fluid capillary forces can push up. Thus free surface shape becomes flatter.

Figure 2.4 shows the free surface shape in a vertical channel when the contact angle is 60 degrees. The same range of Bond numbers is used in the calculation. The effect of Bond number to the free surface shape shows similar behavior as in Fig. 2.3. Comparing the curves with same Bond number but different contact angle, one can observe the effect of contact angle to the free surface shape. Different contact angles change the slope of the curve that in turn makes the free surface shape different.

When Bond number becomes zero, numerical calculation cannot be performed because the right-hand side of both Eqs. (2.3.14) and (2.3.15) become zero. Instead, a small value of Bond number ($B = 0.001$) is chosen in the numerical calculation. At the

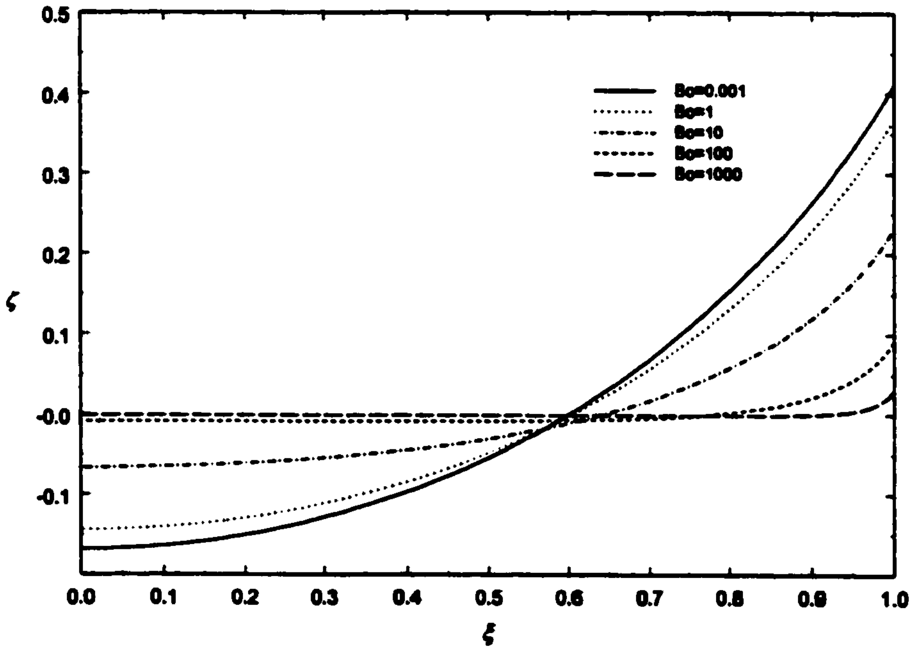

Figure 2.3 Free surface shapes in a vertical channel under different Bond numbers when contact angle is 30 degrees.

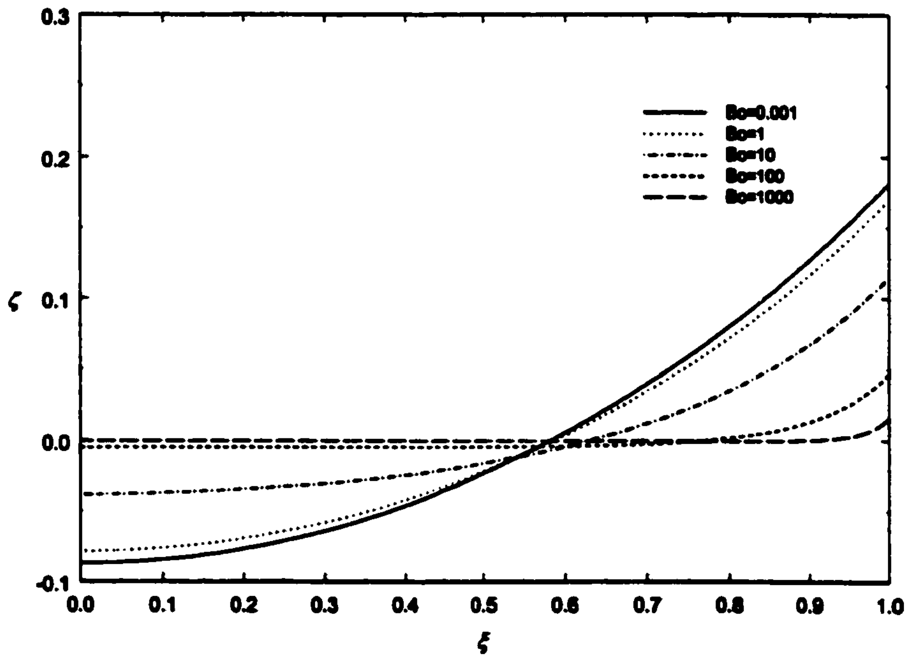

Figure 2.4 Free surface shapes in a vertical channel under different Bond numbers when contact angle is 60 degrees.

same time, the analytical solution of a circular free surface shape is obtained and compared with the numerical solution when Bond number is 0.001. Numerical calculation appears identical with the analytical curve for both contact angle values used in this study.

2.4 Free Surface Shape in an Inclined Channel

Free surface shape in a channel changes with Bond number, contact angle, and the orientation of the channel. In the above figures of free surface in a vertical channel, the shapes of the free surfaces are symmetric since gravity is in the axis of symmetry of the channel. If the channel is inclined with gravity direction, the free surface shape will lose its symmetry. Calculation of free surface shape needs to include inclination angle of the channel as one of the parameters that influence the result.

The choice of coordinate system and the relative parameters are shown in Fig. 2.5. It can be seen that the coordinate system is the same as for the calculation of free surface in a vertical channel. The equations that need to be solved are the same. The changes are the equations of channel walls and boundary conditions. For free surface shape in a vertical channel, the integration of the curve shape starts from the channel wall represented by the equation $\xi = \sqrt{Bo}$. Only half of the curve needs to be calculated because of symmetry. For an inclined channel, however, contact points on both walls need to be considered. Using the coordinate system chosen, the equation for the walls of the channel is:

$$\xi = \frac{\sqrt{Bo}}{\sin\theta} \pm \frac{\zeta}{\tan\theta}, \qquad (2.4.1)$$

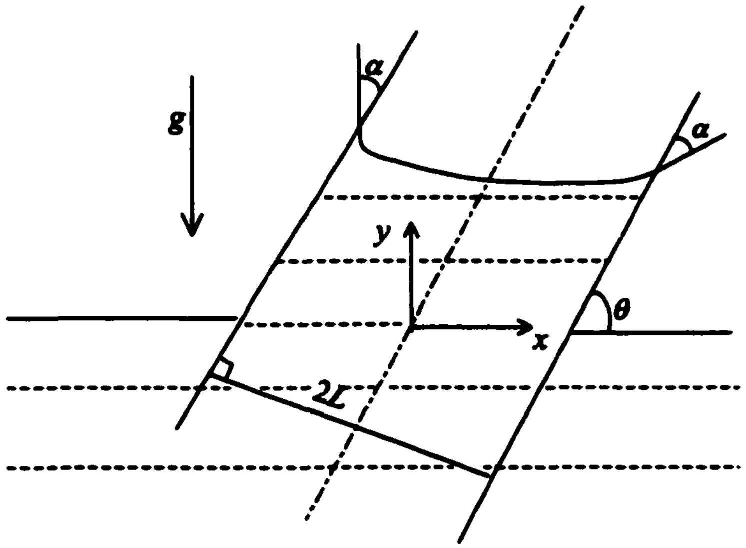

Figure 2.5 Free surface in an inclined channel and the coordinate system used in the analysis.

where θ is the inclination angle of the channel. The plus and minus signs in Eq. (2.4.1) represent the right and left walls, respectively. The centerline of the channel is:

$$\xi = \frac{\zeta}{\tan\theta}. \tag{2.4.2}$$

Both Eq. (2.4.1) and Eq. (2.4.2) are in nondimensional form with the same method of nondimensionlization. The boundary conditions are:

At the left wall: $\frac{d\xi}{d\tau} = \cos(\theta + \alpha)$, $\frac{d\zeta}{d\tau} = -\sin(\theta + \alpha)$;

At the right wall: $\frac{d\xi}{d\tau} = \cos(\theta - \alpha)$, $\frac{d\zeta}{d\tau} = \sin(\theta - \alpha)$.

A Similar method is used as in the calculation of free surface shapes in a vertical channel. To show the effect of Bond number on the free surface shape, a new method of comparing the shapes of the curves is used. The origin of the coordinate system is moved to the contact point on the left wall of the channel. With the same contact angle value, all the curves start with the same slope. The effect of Bond number on the free surface shape can easily be observed.

Figure 2.6 shows free surface shapes in an inclined channel with inclination angle of 30 degrees and contact angle 30 degrees. Three different Bond numbers 0.001, 1, and 10 and used for the calculation. Since contact angles are the same for all three curves, all three curves start with the same slope. Comparing the spreading of the free surface in horizontal direction, the effect of Bond number can be observed. Figure 2.7 shows curves with contact angle of 60 degrees. The inclination angle of the channel is still 30 degrees.

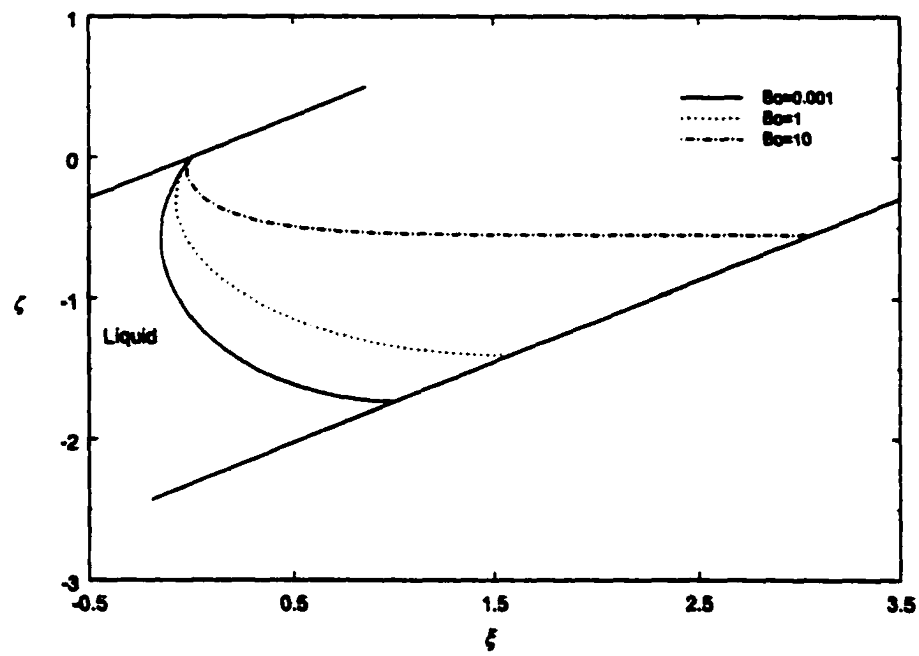

Figure 2.6 Free surface shapes in an inclined channel under different Bond numbers when contact angle is 30 degrees and inclination angle is 30 degrees.

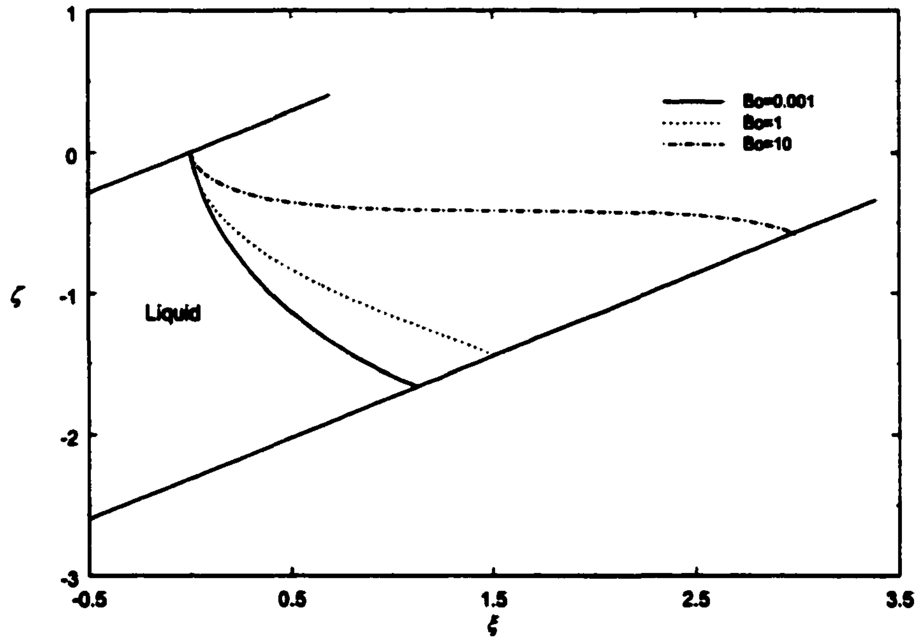

Figure 2.7 Free surface shapes in an inclined channel under different Bond numbers when contact angle is 60 degrees and inclination angle is 30 degrees.

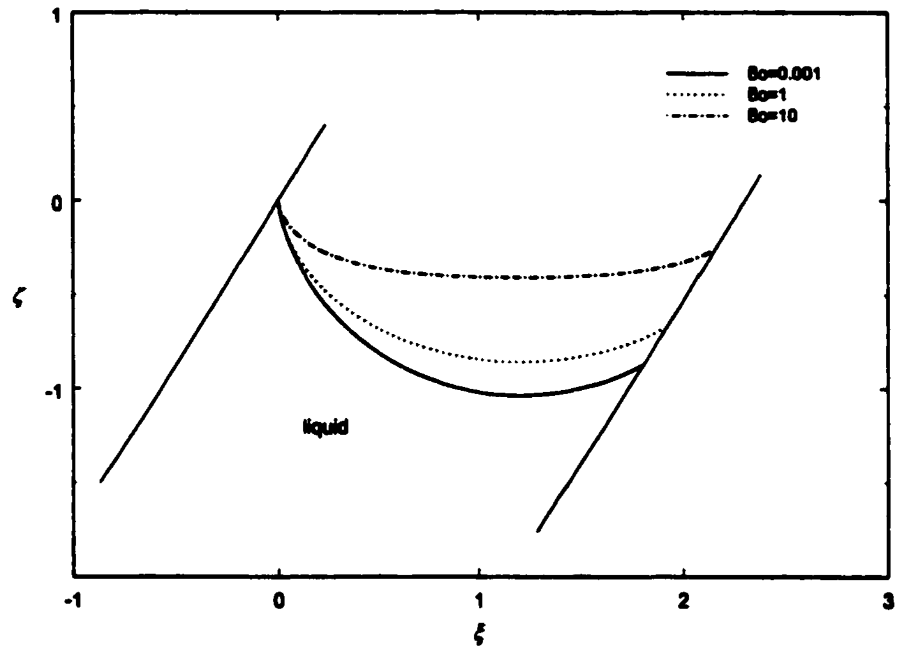

Figure 2.8 Free surface shapes in an inclined channel under different Bond numbers when contact angle is 30 degrees and inclination angle is 60 degrees.

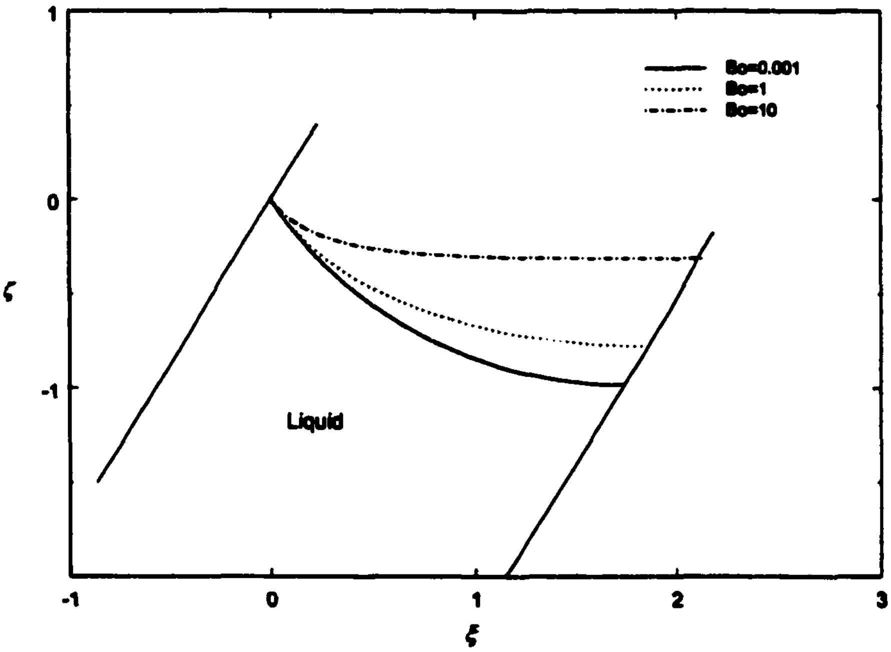

Figure 2.9 Free surface shapes in an inclined channel under different Bond numbers when contact angle is 60 degrees and inclination angle is 60 degrees.

Same values of Bond numbers are used in the three curves. Similar effect of Bond number on the free surface shape as in Fig. 2.6 can be observed. Comparing curves with same Bond number but different inclination angles, it can be seen that the spreading of the free surface decreases with increase of inclination angle. Figure 2.8 shows the free surface shapes with 30 degrees contact angle. The inclination angle of the channel is 60 degrees. Again the same effect of Bond number on the free surface shape is observed. Comparing curves in Fig. 2.8 with the ones in Fig. 2.6, the effect of contact angle on the free surface shape can be seen. Figure 2.9 show free surface shapes with 60 degree contact angle. The inclination angle of the channel is 60 degrees. Similar effect of contact angle on the free surface shape can be observed by comparing curves in Fig.2.9 with the ones in Fig. 2.7 with the same Bond number. Observing all the curves in Figs. 2.6-2.9, most of them appear to be not symmetric except the ones when Bond number is 0.001. As discussed before, free surface shape becomes circular when gravity effect is absent. A circular shape of free surface in a channel is always symmetric. This is the reason when Bond number decreases, the free surface shapes gradually approach to be symmetric. When the inclination angle θ is set to 90 degrees, the resulting curves are found to be identical with the results of free surface in a vertical channel obtained in the previous section.

2.5 Free Surface Shape in a Horizontal Channel

If a two-dimensional channel is inserted into a fluid reservoir, fluid will be driven by capillary forces to move along channel walls. Capillary forces support the weight of the fluid column between channel walls. If the channel is horizontal, however, the forces from the top and bottom walls support the weight of the fluid column. Force balance on the free surface between walls is the balance of capillary pressure with the hydrostatic pressure. Since the hydrostatic pressure at the bottom of the fluid column is unknown, not the same as free surface in a vertical or inclined channel, a different method needs to be used to solve the free surface shape.

Figure 2.10 shows the coordinate system and the relevant parameters used in solving the free surface shape in a horizontal wall. The dimensionless Bond number is defined as:

$$Bo = \frac{\rho g h^2}{\sigma}. \tag{2.5.1}$$

Assume the hydrostatic pressure at the bottom wall is p_0. Laplace's equation can be written as:

$$-p_0 - \rho g x = \sigma \frac{y''}{(\sqrt{1+y'^2})^3}. \tag{2.5.2}$$

Force balance on the whole surface requires that capillary forces balance the force generated by pressure difference. This balance can be written as:

$$(p_0 - \rho g h) 2h = 2\sigma \cos\alpha. \tag{2.5.3}$$

Eliminating p_0 from Eqs. (2.5.2) and (2.5.3), one gets:

$$\frac{\rho g h}{\sigma} + \frac{\cos\alpha}{h} - \frac{\rho g}{\sigma} x = \frac{y''}{(\sqrt{1+y'^2})^3}. \tag{2.5.4}$$

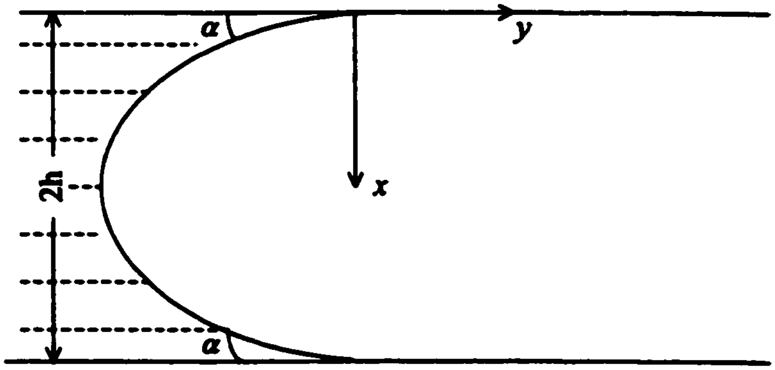

Figure 2.10 Free surface in a horizontal channel and the coordinate system used in the analysis.

Equation (2.5.4) is then nondiemnsionlized using the same parameters as before and Eq. (2.5.1). The nondimensional equation is written as:

$$\sqrt{Bo}+\frac{\cos\alpha}{\sqrt{Bo}}-\xi=\frac{\zeta''}{(\sqrt{1+\zeta'^2})^3}. \tag{2.5.5}$$

Two boundary conditions are needed to solve Eq. (2.5.5). These boundary conditions are the contact angles on the walls. The boundary conditions are expressed as:

When $\xi=0$, $\zeta'=-(\tan\alpha)^{-1}$;

When $\xi=2\sqrt{Bo}$, $\zeta'=(\tan\alpha)^{-1}$.

Using these boundary conditions, Eq. (2.5.5) can be integrated once to obtain:

$$\zeta'=\frac{g(\xi)}{\sqrt{1-(g(\xi))^2}}, \tag{2.5.6}$$

Where

$$g(\xi)=-\frac{1}{2}\xi^2+(\sqrt{Bo}+\frac{\cos\alpha}{\sqrt{Bo}})-\cos\alpha. \tag{2.5.7}$$

It can be seen from Eq. (2.5.6) that the absolute value of $g(\xi)$ can not be greater than 1 in order for the equation to be valid. Since the value of $g(\xi)$ satisfies this condition on both walls, as one can see by plugging the relevant ξ values into Eq. (2.5.7). The only condition for the validity of Eq. (2.5.6) is:

$$|g_{max}|=\frac{Bo+\cos^2\alpha/Bo}{2}\leq 1. \tag{2.5.8}$$

Solving Eq. (2.5.8), the limiting value of Bond number can be obtained as:

$$1-\sin\alpha\leq Bo\leq 1+\sin\alpha. \tag{2.5.9}$$

Physically, a decrease in Bond number won't break free surface. So the left half of Eq. (2.5.8) is given up for the limitation of Bond number. Siekmann's (1977) study had a similar discussion of the limitation of Bond number. Starting from the equation in Siekmann's work that leads to the limit Bond number, one would get the same range as in Eq. (2.5.8). However, there was no explanation of why the lower limit of the Bond number was dropped. From this point of view, it can be seen that the analytical solution from integrating Eq. (2.5.6) will not cover the whole range of Bond number.

Integrating Eq. (2.5.6), the analytical solution for free surface shape in a horizontal channel can be obtained as:

$$\zeta = \frac{2}{b1\sqrt{a1+ba}}\{(b1-a1)\Pi(\delta,\gamma^2,\gamma)+a1\,\mathrm{F}(\delta,\gamma)\}, \tag{2.5.10}$$

where

$$a1 = Bo + \frac{\cos^2\alpha}{Bo}; \tag{2.5.11}$$

$$b1 = 2; \tag{2.5.12}$$

$$\delta = \arcsin\sqrt{\frac{(a1+b1)(1-\cos\alpha)}{2(a1-b1\cos\alpha)}}; \tag{2.5.13}$$

$$\gamma = \sqrt{\frac{2b1}{a1+b1}}, \tag{2.5.14}$$

and Π and F are the elliptic integrals of the third and first kind, respectively.

The curves of the free surface shapes in a horizontal channel can be obtained either by numerically integrating Eq. (2.5.6) or by drawing the curve from Eq. (2.5.10). The step length in the numerical integration is the same as the previous calculations of free surface in vertical and inclined channels. In order to draw the curve for Eq. (2.5.10), an IMSL Fortran subroutine is used to generate the data file. Curves from both of these methods are compared with each other. For Bond numbers in the range shown in Eq. (2.5.8), curves using both methods are identical. When the Bond number reaches the upper limit of the Bond number, curves using both methods appear to be unstable. If the Bond number reaches the lower limit of the Bond number, Eq. (2.5.10) cannot give any curve. But the numerical integration of Eq. (2.5.6) still can obtain the shape of the free surface.

Figure 2.11 shows the free surface shapes in a horizontal channel with different Bond numbers. The values of Bond numbers are 0.001, 0.1, 1, and 1.25. Contact angle used is 30 degrees. It can be seen that increase in Bond number makes free surface spreads further in the horizontal direction. If Bond number reaches its upper limit, free surface will detach from the upper wall and form and form a liquid drop on the bottom wall. When Bond number decreases, the shape of the free surface gradually approaches to be circular that represents free surface shape with no gravity.

Figure 2.12 shows the free surface shapes in a horizontal channel with different Bond numbers when contact angle is 60 degrees. Bond numbers used are the same as in Fig. 2.11. Same effect of Bond number on the spreading of the free surface is observed. Comparing the curves of the same bond number but different contact angle, the effect of contact angle on the spreading can be observed. The spreading of the free surface decreases with increase in contact angle. As Bond number decreases, the free surface shape gradually becomes a symmetric circular shape.

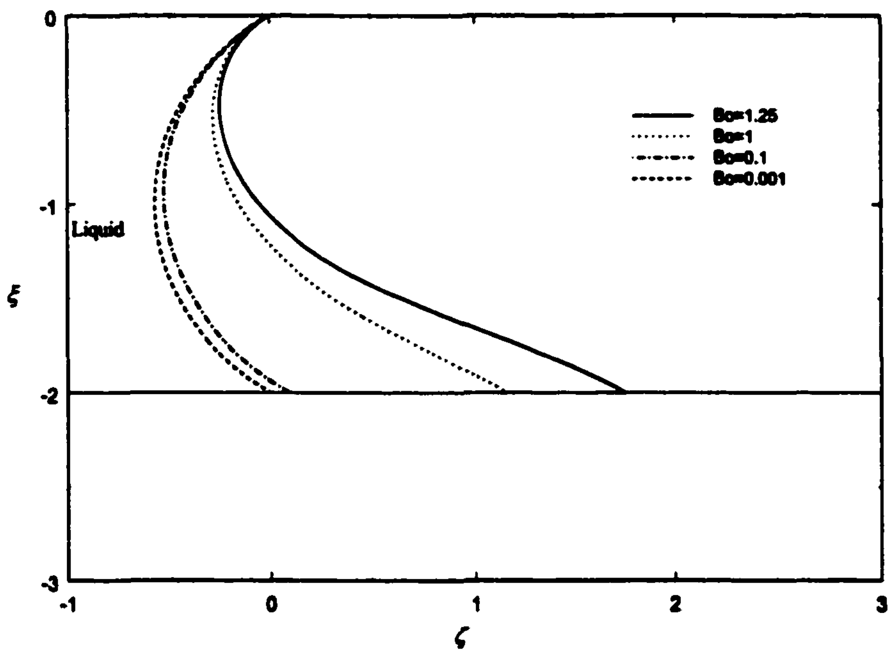

Figure 2.11 Free surface shapes in a horizontal channel under different Bond numbers when contact angle is 30 degrees.

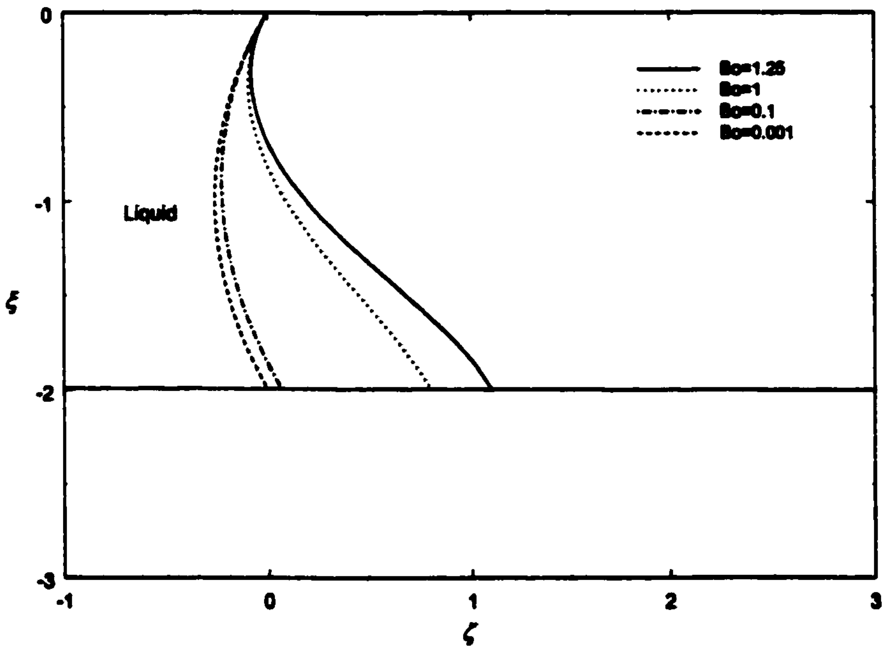

Figure 2.12 Free surface shapes in a horizontal channel under different Bond numbers when contact angle is 60 degrees.

2.6. Conclusion

Free surface shapes in a two-dimensional channel for different Bond numbers, contact angles and inclination angles are obtained. Free surface shapes in a vertical channel are symmetric to the centerline of the channel. The shape of the free surface becomes flatter when Bond number is decreased. In a vertical channel, the free surface shapes lose their symmetry unless Bond number is 0. Increase in Bond number makes free surface spreads in horizontal direction. If the channel is horizontal, the analytical solution to Laplace equation cannot cover the whole range of the Bond number value. Numerical calculation is still necessary for free surface shape calculation under small Bond numbers. Free surface shape becomes unstable when Bond number approaches its limit value. Similar as the free surface shapes in vertical and inclined channels, increase in Bond number increases the spreading of the fluid in horizontal direction.

Chapter 3 QUASI-STATIC IMPREGNATION OF A FIBER BED BY CAPILLARY FORCES IN A GRAVITY FIELD

3.1 Introduction

Impregnation of a porous medium takes place in a number of manufacturing processes. During these processes, the fluid wets the porous medium and impregnates the pores until the medium is fully saturated. In particular, molding of composite materials involves impregnation of porous preforms by a low viscosity thermosetting resin. These preforms are usually made of glass or graphite fibers assembled in a particular pattern. Depending on the material used and the geometry of the part, an external pressure is usually applied for several seconds to facilitate the impregnation. In addition to the external pressure, capillary forces are often important in enhancing the impregnation. At smaller length scales, capillary forces govern the impregnation dynamics for a low viscosity resin. Thus, it is important to investigate the capillary impregnation of a porous fiber bed to characterize the impregnation speed. The dependence of the impregnation behavior on the material properties such as the surface tension and viscosity of the fluid, the contact angle between the fluid and the porous media, and the fiber volume fraction of the porous fiber bed need to be fully understood.

The fluid front motion in a pressure driven creeping flow through a circular tube was first studied by Washburn (1921). Washburn's results have been subsequently used by various researchers to model the impregnation of an anisotropic medium. Depending on the microstructure of the anisotropic medium, the flow is modeled to take place through equivalent circular tubes as proposed by Kosolov (1988) and Marmur and Cohen (1997). The flow models based on Washburn's study predict that the impregnation length in a porous medium varies linearly with the square root of time. Experimentally, the fluid front motion in porous fiber beds is shown to agree with the model predictions based on Washburn's equation (Williams et al. 1974, Bruil and Aartsen, 1974).

Bayramli and Powell (1990) used Washburn's equation to numerically calculate the fluid front motion driven only by capillary pressure though a fiber bed. In their study, the fibers were arranged in a hexagonal pattern and the flow direction was normal to the fiber axis. Instead of implementing a model using an equivalent circular tube, the governing equation of capillary motion in a two-dimensional channel is used to simulate the impregnation through the fiber bed. It is found that during impregnation, the velocity of the fluid front changes periodically as it moves through the layers of hexagonally-arranged fibers. However, as the impregnation takes place across several fiber layers, the linear variation of the impregnation distance with the square root of time is observed at a larger length scale compared to fiber diameter. In Bayramli and Powell's work, gravity effects on the impregnation velocity were assumed to be negligible. Thus, the final height of the fluid front location could not be predicted as the impregnation velocity was asymptotically decreased with time. Due to the presence of gravity, a finite impregnation height exists where the capillary forces are balanced by the gravity. Bayramli and Powell (1990) also obtained permeability of the fiber bed based on the impregnation velocity and their results agreed with the experimental data from Lam and Kardos (1988).

Instead of using the capillary impregnation velocity, the permeability of a fiber bed can be obtained by studying the average resistance forces in a steady, pressure driven flow through a fiber bed. Two basic models (i.e., cell model and lubrication model) are used to predict permeability. Cell model is used for fiber beds with low fiber volume fraction and lubrication model is used for fiber beds with high fiber volume fraction. In both models, permeability of the fiber bed is expressed as a function of the friction force on the fiber surface. Cell model assumes the flow field around each fiber is not affected by the surrounding fibers. Cell model was first used by Happel (1959) to obtain the drag force on the surface of a single fiber. Later, Sangani and Acrivos (1982) numerically obtained permeability of long cylinders and spheres packed in various cubic arrays. Lubrication model, on the other hand, accounts for the effect of neighboring fibers on the flow. The friction forces in the flow channel formed by two fiber surfaces were obtained by Keller (1964). Gebart (1992) proposed an approximate equation for the permeability of a hexagonally arranged fiber bed. Gebart's work is based on implementation of lubrication model with the experimental observation of Gutowski (1987). Bruschke (1992) combined cell and lubrication models and presented a closed form expression for the permeability, thus covering a wider range of fiber volume fraction.

This chapter investigates the fluid front motion during the transverse impregnation of a fiber bed due to capillary forces. The fibers are arranged in a hexagonal pattern and the impregnation takes place perpendicular to the fiber axis. The final impregnation height is obtained as a function of fiber volume fraction, contact angle, and Bond number as the capillary forces are balanced by the gravity. The impregnation velocity is also used to predict the permeability of the fiber bed.

3.2 Quasi-Steady Capillary Motion With Gravity Effect

3.2.1 Capillary Motion in a Uniform Channel

Fluid front motion through a fiber bed is modeled using the capillary motion through a two-dimensional channel. Therefore, the fluid front motion in a two-dimensional channel is essential to the study of capillary impregnation of a fiber bed. Static free surface shape in a two-dimensional channel was studied in the previous chapter. For a quasi-steady fluid motion, free surface shape at every location is assumed to be the same as its static free shape. Thus static free surface shape obtained previously can be used in the study of quasi-steady capillary flow in a channel.

The channel geometry, coordinate system and the relevant parameters are shown in Fig. 3.1. Flow direction is opposite to gravity direction. The basic assumptions for the quasi-steady capillary motion analysis are:

1. Only capillary forces drive the flow.
2. Viscous forces dominate inertia forces during the flow.
3. The flow is quasi-steady and the free surface shape is the same as the static shape.
4. The flow is unidirectional.

From these assumptions, the velocity field satisfies:

$$v_x = 0\text{; and } v_z = 0. \qquad (3.2.1)$$

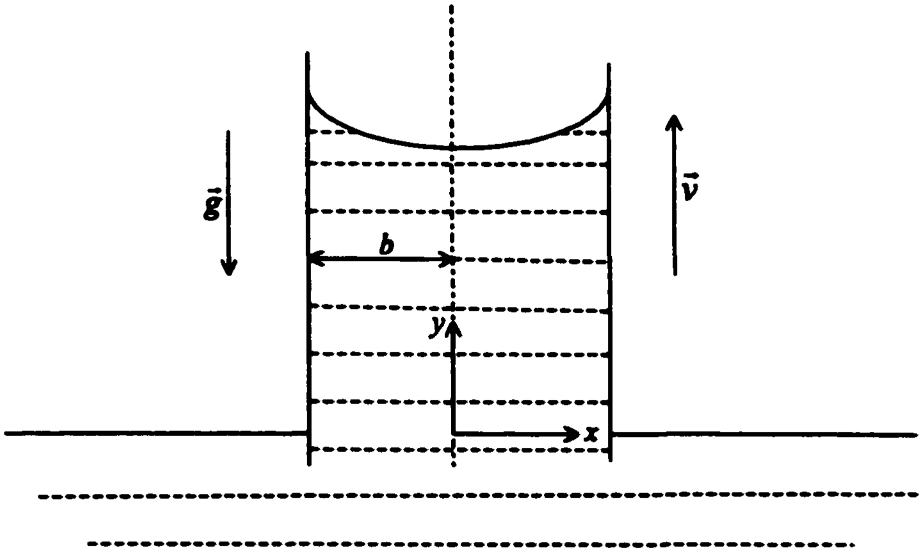

Figure 3.1 Capillary motion in a vertical channel and the coordinate system used in the analysis of the motion.

Since the flow is two-dimensional, the variation of flow field in the third direction vanishes. This condition can be expressed as:

$$\frac{\partial}{\partial z}=0\,. \tag{3.2.2}$$

For an incompressible fluid, the continuity equation writes:

$$\frac{\partial x_x}{\partial x}+\frac{\partial v_y}{\partial y}+\frac{\partial v_z}{\partial z}=0\quad. \tag{3.2.3}$$

Combining Eqs. (3.2.1) and (3.2.3), one can draw the following conclusion:

$$\frac{\partial v_y}{\partial y}=0\,. \tag{3.2.4}$$

One can see that flow velocity is one-dimensional. Velocity of the flow changes only in the direction normal to the flow direction.

The capillary pressure generated by the free surface drives the flow. For a steady state flow driven by pressure difference, Navier-Stokes equation can be expressed as:

$$0=-\frac{\partial P}{\partial x}; \tag{3.2.5}$$

$$0=-\frac{\partial P}{\partial y}-\rho g+\mu\frac{\partial^2 v_y}{\partial x^2}; \tag{3.2.6}$$

$$0=-\frac{\partial P}{\partial z}. \tag{3.2.7}$$

The no-slip boundary conditions on the channel walls are:

When $x = \pm b$; $v_y = 0$.

Capillary motion of the flow is driven by the capillary pressure. From Eqs. (3.2.5) to (3.2.7), one can see that the pressure is linear in the y direction. The value of the pressure gradient due to capillary effect can be obtained using Laplace equation as:

$$\frac{dP}{dy} = -\frac{\sigma}{r_1 y}, \tag{3.2.8}$$

Where r_1 is the radius of curvature of the free surface. Equation (3.2.6) is integrated twice with respect to x to obtain the velocity of the flow. The integration constants can be solved using the no-slip boundary conditions. The result of the flow velocity is:

$$v = \frac{1}{2\mu}\left(-\frac{\sigma}{r_1 y} + \rho g\right)(x^2 - b^2). \tag{3.2.9}$$

Equation (3.2.9) shows the velocity of the quasi-steady capillary flow in a channel. The volume flow rate of such flow can be obtained by integrating Eq. (3.2.9) to obtain:

$$\begin{aligned} dQ &= \left[\int_{-b}^{b} v dx\right] dt \\ &= -\frac{2}{3\mu} b^3 \left(-\frac{\sigma}{r_1 y} + \rho g\right) dt \end{aligned} \tag{3.2.10}$$

The flow rate can also be expressed with the time rate change of the location of the fluid front as:

$$dQ = 2b dy \,. \tag{3.2.11}$$

Equation (3.2.11) is then plugged into Eq. (3.2.10) and integrated to obtain the location of the fluid front with time. The initial condition of the flow is:

When $t=0$; $y=0$.

The expression of the fluid front location with time is:

$$y + \frac{\sigma}{\rho g \eta} \ln\left(1 - \frac{\rho g \eta y}{\sigma}\right) = -\frac{\rho g b^2}{3\mu} t \,. \tag{3.2.12}$$

The left-hand side of Eq. (3.2.12) can be expanded as a polynomial in terms of $\rho g \eta y / \sigma$. After some simple mathematical rearrangement, the following equation can be obtained:

$$t = \frac{3\mu}{b^2}\left[\frac{1}{2}\frac{\eta}{\sigma} y^2 + \frac{1}{3}\frac{\rho g \eta^2}{\sigma} + \cdots\right]. \tag{3.2.13}$$

It can be seen that the first term on the right-hand side of Eq. (3.2.13) is not dependent of gravity. When gravity becomes 0, the location of the fluid front changes linearly with the square root of time. The resulting equation of Eq. (3.2.13) when gravity becomes 0 is the same as in Bayramli and Powell's work where governing equation for capillary motion in a channel without gravity effect was presented.

The value of y in Eq. (3.2.12) is bounded for the validity of the natural logarithmic term. If y approaches its upper bound, the left-hand side of Eq. (3.2.12) approaches 0. Then the value of t should also be infinity. Physically, this is the final height that the fluid column can reach under capillary forces. The final height of the fluid column is:

$$y = \frac{\sigma}{\rho g \eta}. \tag{3.2.14}$$

To present the capillary motion in a uniform channel in a general form, Eq. (3.2.12) is nondimensionlized using the following parameters:

$$T = \frac{\rho g b}{\mu} t; \tag{3.2.15}$$

$$Y = y\sqrt{\frac{\rho g}{\sigma}}; \tag{3.2.16}$$

$$Y_f = r_1\sqrt{\frac{\rho g}{\sigma}}\ . \tag{3.2.17}$$

$$Bo = \frac{\rho g w^2}{\sigma}\ . \tag{3.2.18}$$

The nondimensionlized equation is:

$$Y + Y_f \ln(1 - \frac{Y}{Y_f}) = -\frac{1}{3}\sqrt{Bo}T\ . \tag{3.2.19}$$

Figures 3.2 and 3.3 show the solution curves of Eq. (3.2.19) under different Bond numbers. The value of the radius of curvature, r_1, is read from the calculation of the previous chapter when static free surface shapes are calculated. Figure 3.2 shows the solutions of Eq. (3.2.19) when contact angle is 30 degrees. Figure 3.3 shows the solutions when contact angle is 60 degrees. It can be seen from both figures that increase in Bond number decreases the final height that the fluid front can reach. Physically, increase in gravity means that the volume of fluid that capillary forces can support becomes less. Comparing the curves with same Bond number but different contact angles, it can be seen that an increase in contact angle results in a decrease the final height of the fluid front. As the contact angle increases, the vertical component of the capillary forces that supports the gravity of the fluid front decreases. Thus decrease the final height of the fluid front. When Bond number becomes 0, however, there is no bound for fluid climbing because capillary forces totally dominant over gravity. This can be observed from both figures.

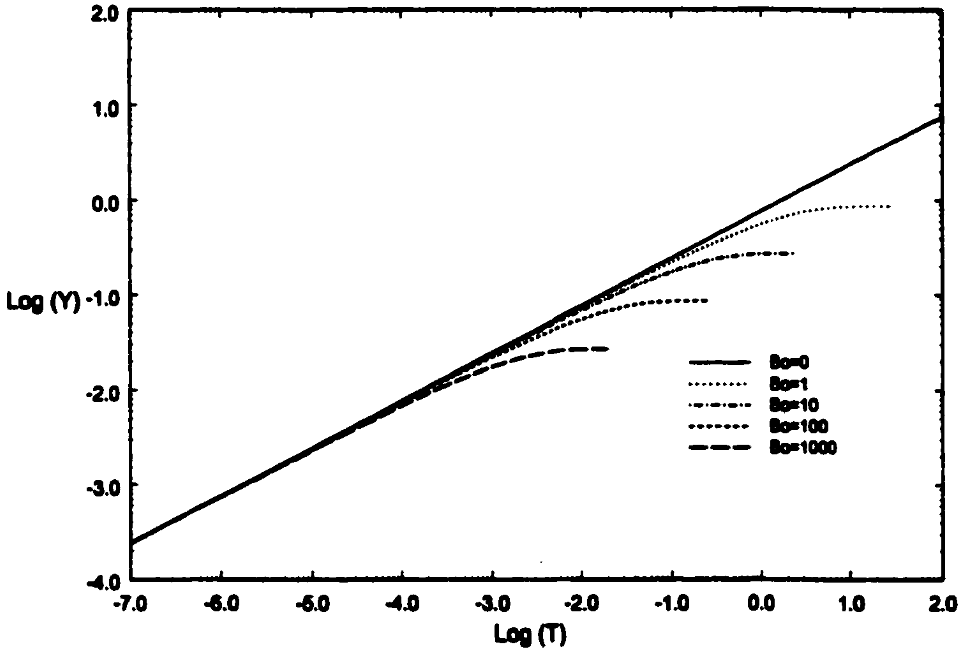

Figure 3.2 Change of the height of the fluid front during capillary motion in a uniform channel when contact angle is 30 degrees.

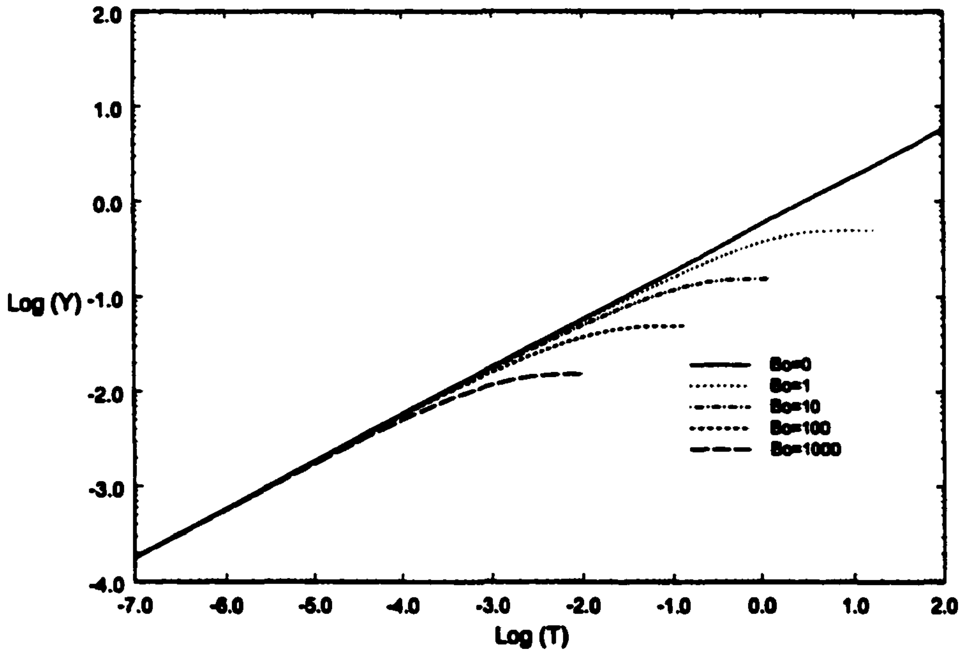

Figure 3.3 Change of the height of the fluid front during capillary motion in a uniform channel when contact angle is 60 degrees.

3.2.2 Capillary Impregnation of a Fiber Bed

If the contact angle between the fluid and the solid surface is less than 90 degrees, the fluid wets the surface and impregnates the porous medium due to capillary pressure. As the capillary impregnation continues, the balance between the gravity, capillary and viscous forces governs the impregnation dynamics. In order to model the impregnation of a porous fiber bed, the flow can be assumed to take place through two-dimensional channels at a microscopic length scale. The width of the channels varies in the flow direction due to the cylindrical surfaces forming the channel boundaries. The governing equation (Eq. (3.2.12)) for capillary impregnation of fluid in a two-dimensional vertical channel can be re-written as:

$$x + \frac{\sigma}{\rho g r_1} \ln(1 \quad \frac{\rho g x r_1}{\sigma}) = \frac{\rho g b^2}{3\mu} t, \tag{3.2.20}$$

where, x is the impregnation distance; σ, ρ, μ are the surface tension, density, and the viscosity of the fluid; g is gravity; r_1 is the radius of curvature of the free surface; b is the half-channel-width; and t is time. The shape of the free surface becomes circular if gravity effect is negligible. For such cases, the radius of curvature of the free surface is given by,

$$r_1 = \frac{b}{\cos\theta}, \tag{3.2.21}$$

where θ is contact angle between the fluid and the channel wall. The velocity of impregnation can be obtained by differentiating Eq. (3.2.20) with respect to time,

$$v = \frac{dx}{dt} = \left(\frac{\sigma}{xr_1} - \rho g\right)\frac{b^2}{3\mu}. \tag{3.2.22}$$

In a vertical channel flow with a free surface, the pressure drop in the flow direction is obtained as:

$$\frac{dp}{dx} = \frac{\sigma}{xr_1} - \rho g. \tag{3.2.23}$$

It is customary to use Darcy's law to define the macroscopic permeability of a fiber bed, K, as:

$$v = \frac{K}{\mu}\frac{dp}{dx}. \tag{3.2.24}$$

By comparing Eqs. (3.2.22) and (3.2.23) with the Darcy's law given in Eq. (3.2.24), the permeability of a two-dimensional channel is given by:

$$K = \frac{b^2}{3}. \tag{3.2.25}$$

3.3 Quasi-Steady Impregnation of Fiber Beds

In order to obtain a general expression for fluid front motion during the impregnation of the fiber bed, Eq. (3.2.20) is nondimensionlized using the following parameters:

$$X = \frac{x}{r}, \tag{3.3.1}$$

$$X_f = \frac{\sigma}{\rho\, g\, r_1\, r}, \tag{3.3.2}$$

$$T = \frac{2\sigma}{3\mu r} t, \tag{3.3.3}$$

$$B = \frac{\rho g b^2}{\sigma}. \tag{3.3.4}$$

Using Eqs. (3.3.1-3.3.4), nondimensional form of Eq. (3.2.19) is obtained as:

$$T = \frac{2}{B}(X + X_f \ln(1 - \frac{X}{X_f})) \quad . \tag{3.3.5}$$

Hexagonal fiber arrangement used in this study and the relevant geometric parameters are shown in Fig.3.4. During impregnation, the fluid front moves forward in between two fibers until it touches the surface of another fiber (i.e., point B in Fig. 3.4) located at the upper layer. Upon contact, the fluid front splits into two flow channels and continues to move forward (e.g., see line AB' in Fig. 3.4). Similarly, as the fluid front moves around a fiber, the contact line from both sides meet at a point (i.e., point D in Fig. 3.4). At this point, both free surfaces detach from the fiber surface and form a single fluid front shown as CC' in Fig. 3.4. For a zero contact angle, the geometric condition to have this detachment possible can be expressed as,

$$\sqrt{3}(r+d) \leq 2r\,, \tag{3.3.6}$$

where r is the fiber radius, and d is the separation distance of fibers shown in Fig. 3.4. For a hexagonal fiber packing pattern, the fiber volume fraction, v_f, is given as:

$$v_f = \frac{\pi}{2\sqrt{3}(1+\frac{d}{r})^2}\,. \tag{3.3.7}$$

The maximum fiber volume fraction for this packing geometry can be obtained by setting fiber separation distance, d, to zero in Eq. (3.3.7). Then, Eqs. (3.3.6) and (3.3.7) can be used to obtain the lower and upper bounds of fiber volume fraction to have capillary impregnation. These bounds are:

$$\frac{\sqrt{3}\pi}{8} \leq v_f \leq \frac{\pi}{2\sqrt{3}}\,. \tag{3.3.8}$$

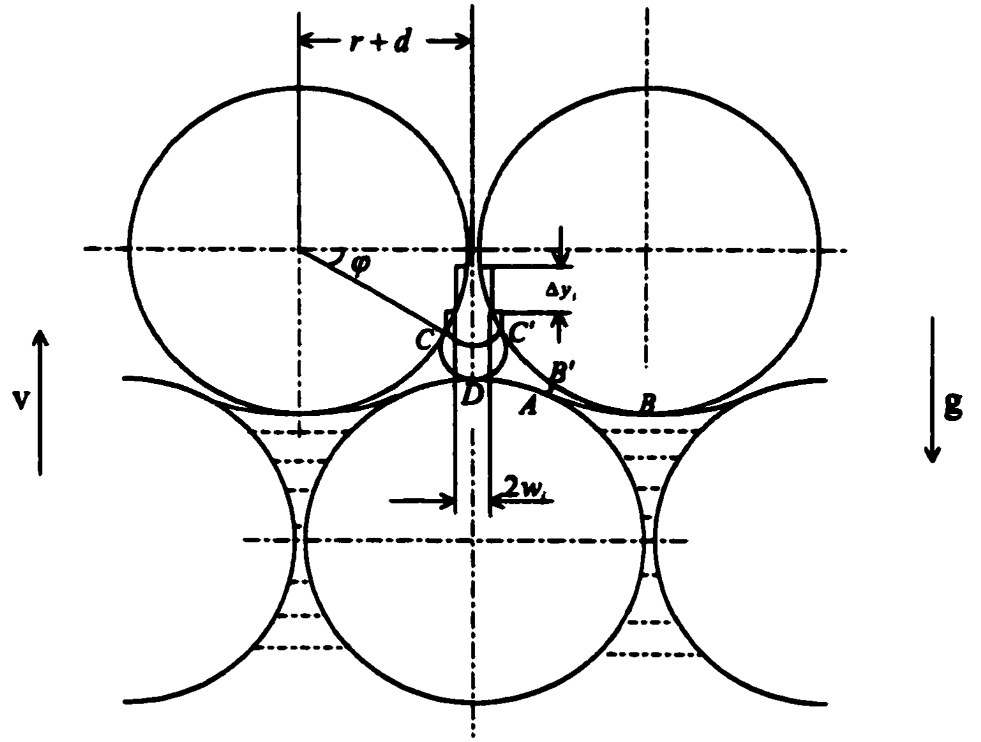

Figure 3.4 Motion of fluid front during capillary impregnation of a fiber bed and the relevant parameters.

The dynamics of capillary impregnation of a fiber bed is affected by the fiber arrangement pattern, fluid properties, capillary pressure and the gravity. To model the impregnation of a hexagonal fiber bed, these factors can be combined into three non-dimensional parameters, i.e., contact angle, θ, fiber volume fraction, v_f, and Bond number, Bo. In this study, the ratio of gravity to capillary forces are characterized by the Bond number as:

$$Bo = \frac{\rho g d^2}{\sigma}. \tag{3.3.9}$$

Width of the flow channel, w, varies as the fluid front progresses between cylindrical fibers. Thus, the parameters B and X_f in Eq. (3.3.5) vary periodically over each fiber layer. The location of the fluid front during impregnation is obtained by solving Eq. (3.3.5) with a marching scheme in nondimensional time T. Small X values are used for numerical accuracy as B and X_f are updated after calculation of each fluid front location. The shape and location of the flow front is obtained for different fiber volume fraction, contact angle, and Bond numbers. The method used in determining the location and the shape of the fluid front is similar to the model presented by Bayramli and Powell (1990).

3.4 Fluid Front Motion during Capillary Impregnation

The fluid front motion during capillary impregnation in a gravity field is best characterized by the variation of nondimensional height as a function of the square root of the nondimensional time, $\sqrt{T}$. The nondimensional impregnation height, $\bar{h} = h/r$, is defined based on h, which is the vertical distance the fluid front has moved into the fiber bed from the beginning of the impregnation process. It should be noted that X defined in Eq. (3.3.1) is different than $\bar{h}$. X is the total impregnation distance measured along the flow path, which changes direction as the fluid front moves around individual fibers.

In most manufacturing processes involving impregnation of a fiber bed, fiber radius is in the order of microns. Also, the separation distance, d, between fibers should be less than 15% of the fiber radius to have capillary impregnation (e.g., see Eq. (3.3.6)) possible. At these small length scales, the Bond number, Bo, defined in Eq. (3.3.9) is at the order of 10^{-7} to 10^{-9} for commonly used polymeric materials. For very small Bond numbers, the gravity effects become negligible in determining the shape of the fluid front. Under these conditions, the free surface becomes circular with the radius of curvature given in Eq. (3.2.20). Gravity effects, however, cannot be neglected in determining the final impregnation height. As the impregnation process continues, the gravity effects become more important and the capillary forces are balanced by the gravity. Capillary number during impregnation is shown to be less than 10^{-5}, hence the static contact angle can be used to simulate the progress of the fluid front (Hoffman, 1975).

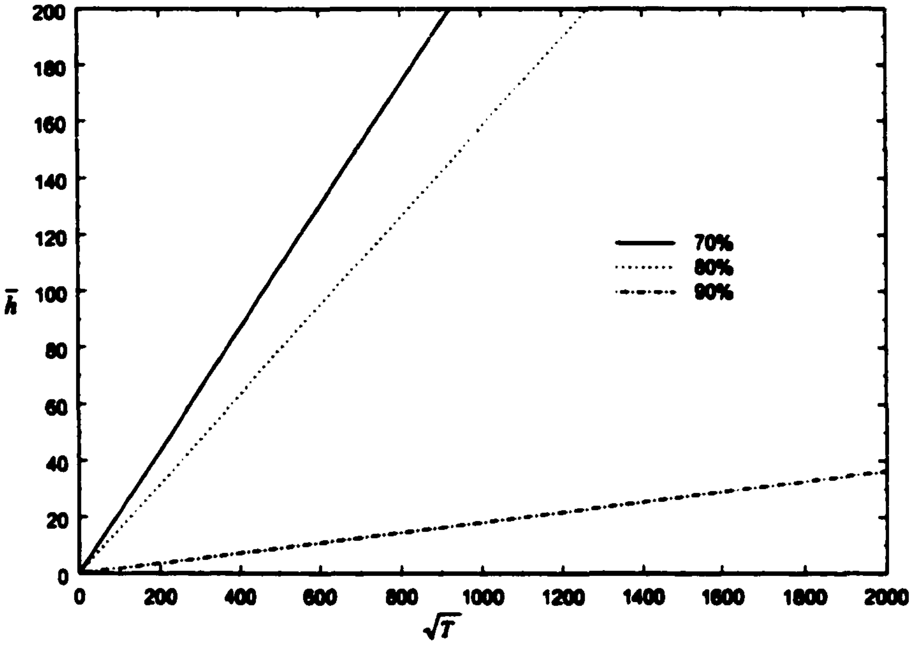

Figure 3.5 Change of vertical impregnation distance during impregnation for different fiber volume fractions. $Bo = 5.72\times10^{-8}$; $\theta = 0^{\circ}$.

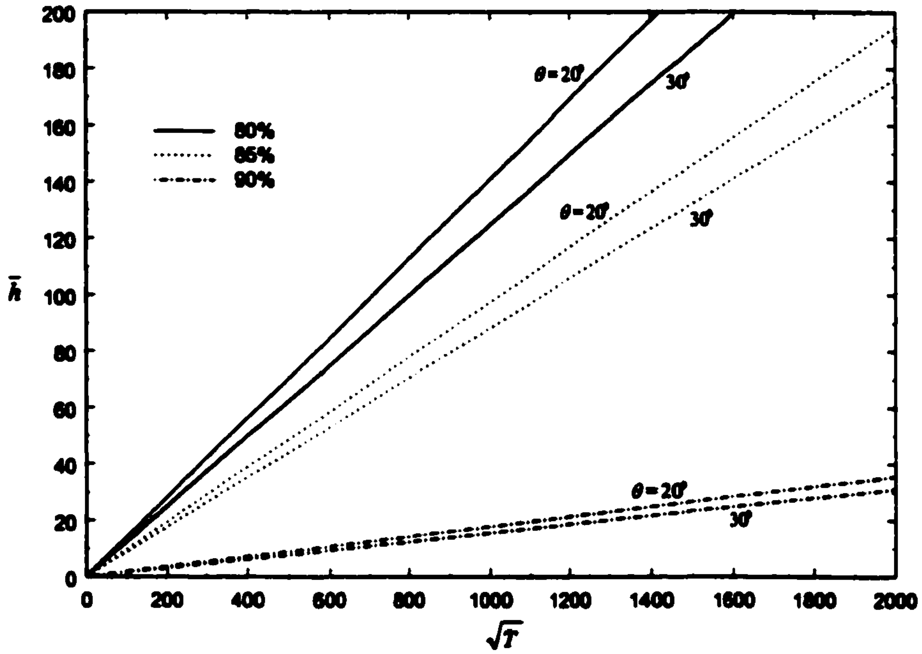

Figure 3.6 Change of vertical impregnation distance during impregnation for different fiber volume fractions. $Bo = 1.27\times10^{-8}$; $\theta = 20^0$ and 30^0.

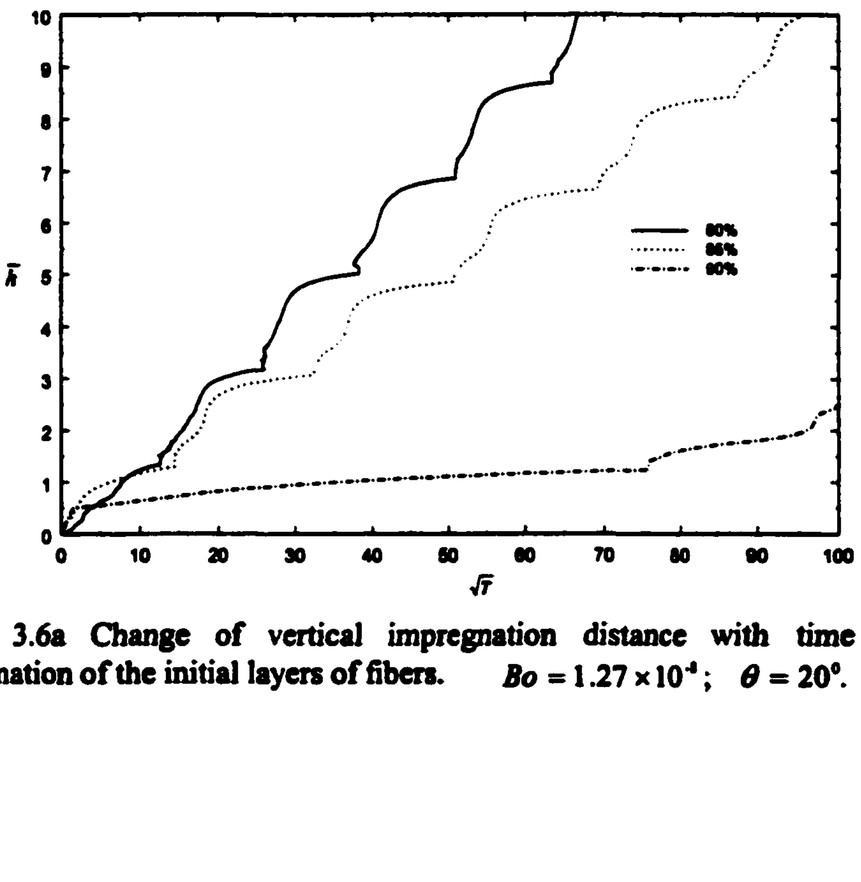

Figure 3.6a Change of vertical impregnation distance with time during the impregnation of the initial layers of fibers. $Bo = 1.27 \times 10^{-4}$; $\theta = 20°$.

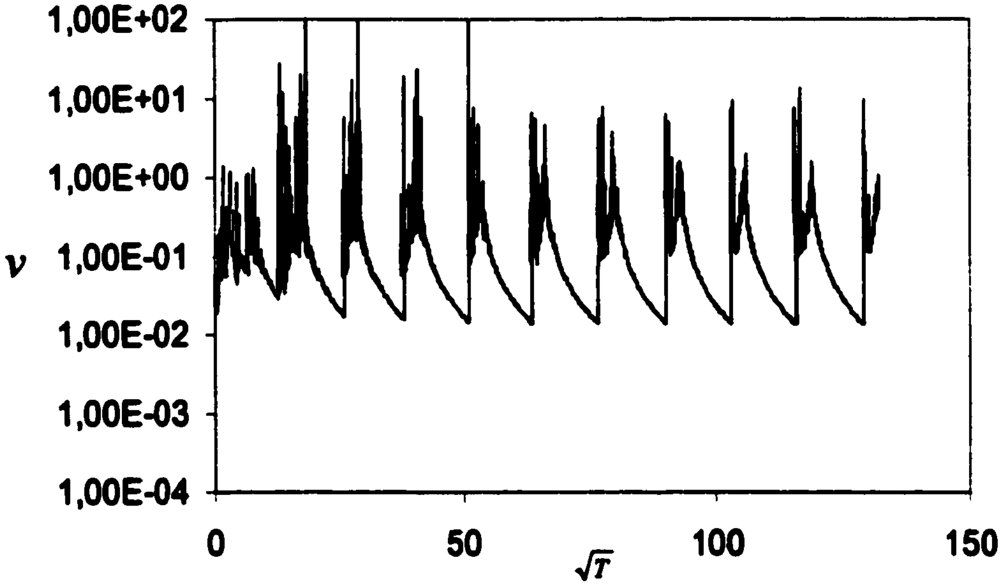

Figure 3.6b Change of impregnation velocity with time during the impregnation of the initial layers of fibers. $v_f = 80\%$; $Bo = 1.27 \times 10^{-4}$; $\theta = 20°$.

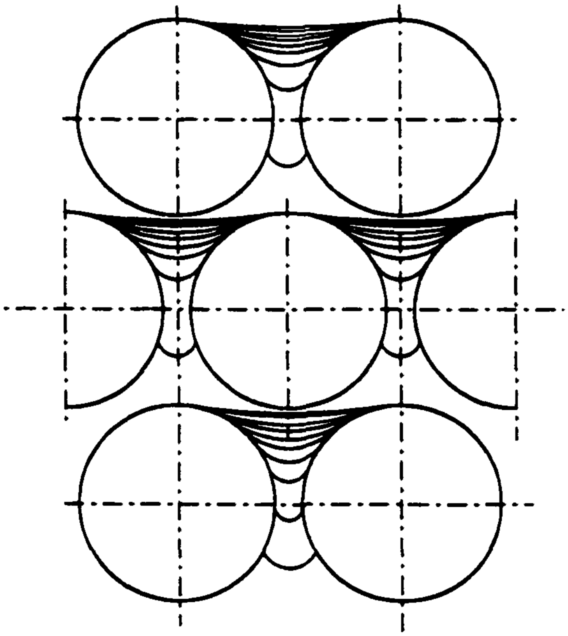

Figure 3.7 Location and shape of the fluid fronts at different times during impregnation for 70% fiber volume fraction.

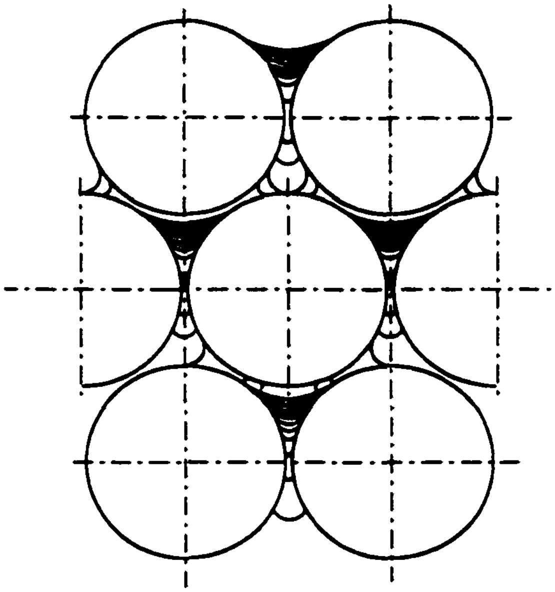

Figure 3.8 Location and shape of the fluid fronts at different times during impregnation for 85% fiber volume fraction.

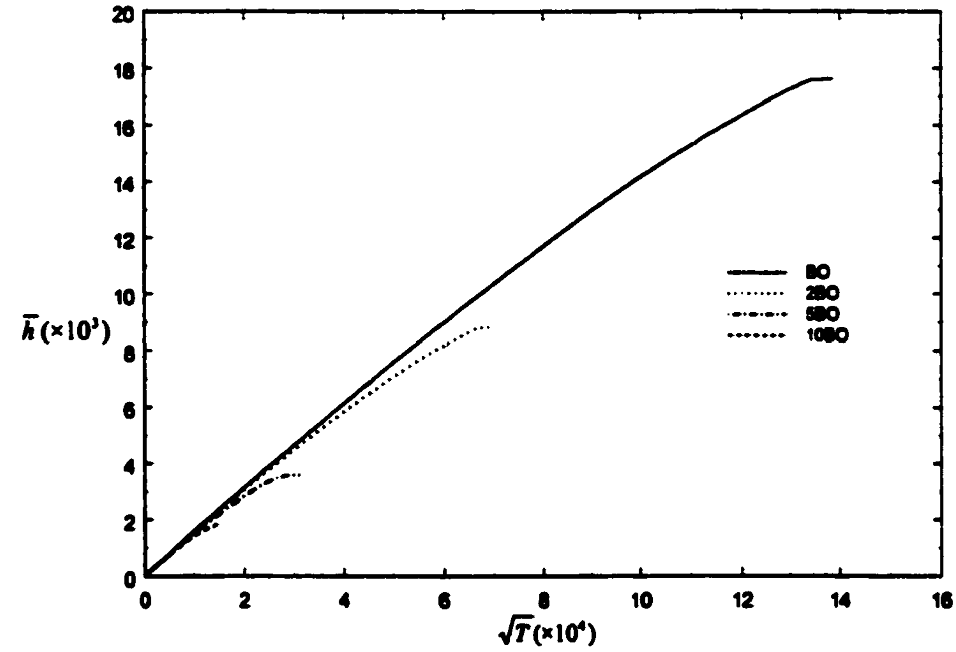

Figure 3.9 Change of vertical impregnation distance during impregnation for different Bond numbers. $Bo = 5.72\times10^{-8}$; $v_f = 70\%$; $\theta = 0^{\circ}$.

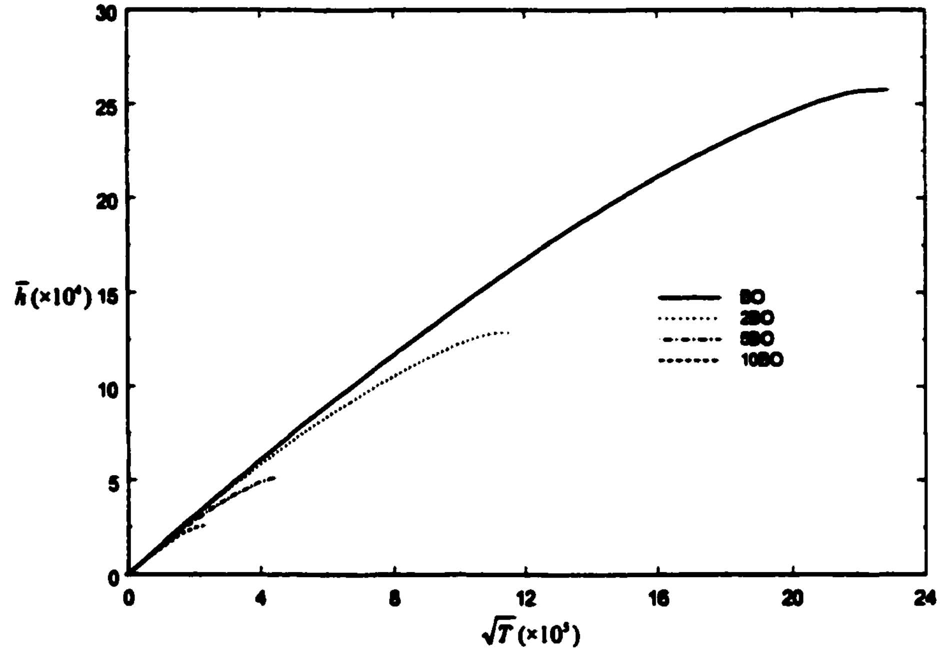

Figure 3.10 Change of vertical impregnation distance during impregnation for different Bond numbers. $Bo = 1.27\times10^{-8}$; $v_f = 80\%$; $\theta = 0^{\circ}$.

Figure 3.5 shows the change in nondimensional impregnation height as a function of square root of nondimensional time. In Fig. 3.5, impregnation heights for 70%, 80% and 90% fiber volume fraction are shown. Contact angle and Bond number are 0^{o} and 5.72×10^{-8}, respectively for all three curves. Since viscous forces dominate inertia during impregnation by capillary forces, an increase in fiber volume fraction increases viscous forces, thus reducing the impregnation speed. It can be seen from Figure 3.5 that as fiber volume fraction increases, the impregnation velocity decreases. For $\sqrt{T} = 400$, increasing fiber volume fraction from 70% to 90% decreases the impregnation height by 90.8%. Figure 3.5 illustrates only the initial stages of the impregnation process. In these early stages, the effect of gravity on the impregnation speed is negligible, and $\bar{h}$ varies linearly with $\sqrt{T}$ as explained earlier. Thus, initial stages of the impregnation process shown by Fig. 3.5 are almost identical to the Bayramli and Powell's impregnation results without gravity effects.

Figure 3.6 shows the effect of contact angle on the impregnation height for three different fiber volume fractions. For Fig. 3.6, Bond number is selected to be 1.27×10^{-8}. An increase in contact angle leads to a flatter free surface as the fluid flows through periodic fiber arrays. The flatness of the free surface yields a lower capillary pressure. Hence, an increase in contact angle decreases the impregnation speed as shown in Fig. 3.6. The effect of contact angle is more prominent if the fiber volume fraction is at the lower range of capillary impregnation (i.e., 70%). For example, increasing contact angle from 20^{o} to 30^{o} reduces the impregnation height, $\bar{h}$, by 10.7%.

Figs. 5.6a and 5.6b Show the initial stage of impregnation of the same fiber bed as in Fig. 5.6. The periodical impregnation velocity change can be observed in both figures. It is further shown in Fig. 5.6b that the impregnation velocity can be two orders of magnitude different when free surface is at different locations of fiber surface.

The influence of fiber volume fraction on the impregnation can also be graphically shown in Figs. 3.7-3.8. Since free surface shape is assumed to be part of a circle in this study, one can draw the shape of the free surface at each step when its location is obtained. Figure 3.7 shows the free surface locations and shapes at different times for 70% fiber volume fraction. Figure 3.8 shows a similar plot when fiber volume fraction is increased to 85%. In Figs. 3.7 and 3.8 fluid fronts are drawn at uniform intervals of square root of time. In both figures, the periodic change of the fluid front velocity is observed. The free surface plots given in Figs. 3.7 and 3.8 shows the fluid motion as the impregnation takes place across the first three fiber layers. During the impregnation of these initial layers, the effect of the gravity cannot be observed. For example the change in the maximum impregnation velocity from 2^{nd} to 3^{rd} fiber layer is less than 2×10^{-4}%.

Figure 3.9 shows the effect of Bond number on the impregnation velocity and final height. In Fig. 3.9, the smallest Bond number, *Bo*, is chosen to be 5.72×10^{-8} and three others curves for 2, 5, and 10 times the Bond number are included. The contact angle and the fiber volume fraction are 0° and 70%, respectively. An increase in Bond number increases the ratio of gravity to capillary forces. Thus, for higher Bond numbers, gravity and capillary forces are balanced at a lower impregnation height. However, the difference in impregnation velocity is negligible at the initial stages of impregnation, and all four curves have the same slope. Figure 3.10 shows a similar plot for the impregnation height. The volume fraction is 80%, Bond number is 1.27×10^{-8}, and contact angle is 0^{o}. As the volume fraction is increased to 80%, total impregnation time is an order of magnitude higher than that of Fig. 3.9. The final impregnation height is also an order of magnitude higher since the Bond number is significantly lower compared to Fig. 3.9. The effect of contact angle on the total impregnation height and time is shown in Fig. 3.11. In Fig. 3.11, contact angle is 20^{o} and Bond number is kept at 1.27×10^{-8}. The increase in contact angle indicates a reduction in capillary forces, which in turn, yields a lower total impregnation height. The impregnation process also takes 20% less time as contact angle is increased to 20^{o}.

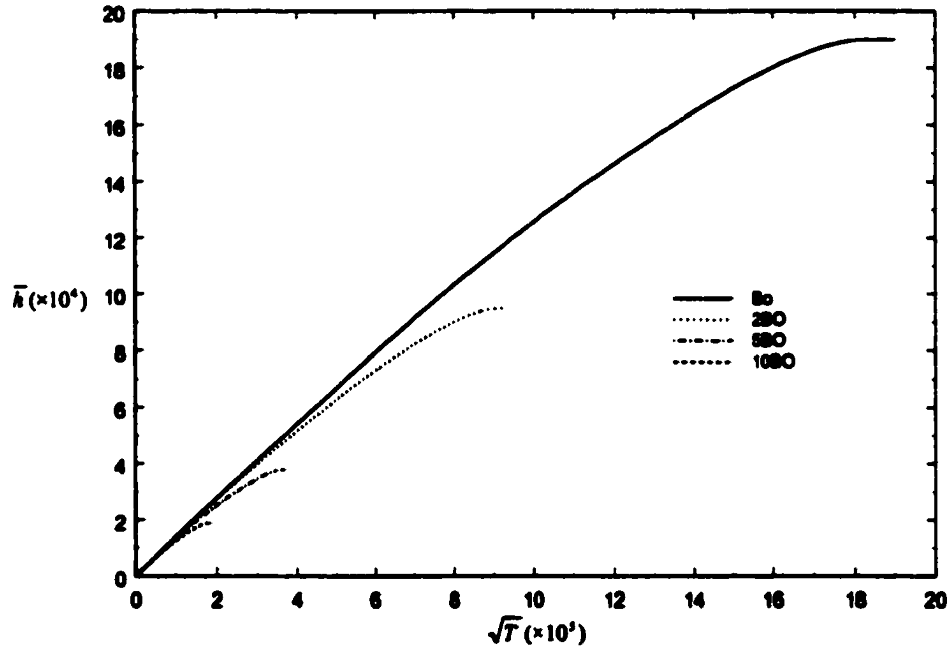

Figure 3.11 Change of vertical impregnation distance during impregnation for different Bond numbers. $Bo = 1.27\times10^{-8}$; $v_f = 80\%$; $\theta = 20^{0}$.

3.5 Permeability Predictions

The model developed for the motion of the fluid front also enables one to determine the permeability of the fiber bed. The permeability of a fiber bed, K, is usually nondimensionlized using the fiber radius, r, as:

$$\overline{K} = \frac{K}{r^2}. \qquad (3.5.1)$$

The permeability of a two-dimensional uniform channel is only a function of its width as given by Eq. (3.2.24). However, Eq. (3.2.24) cannot be directly used to obtain the permeability of fiber beds as the channel width periodically varies based on the microstructural arrangement of the fibers. Bayramli and Powell's study showed that during capillary impregnation of a fiber bed, the location of the fluid front changes linearly with the square root of time if the impregnation is viewed at a larger length scale compared to the radius of a fiber. This linearity can be interpreted as the existence of a two-dimensional uniform channel that has the same permeability with the fiber bed. Thus, to obtain the permeability of a particular fiber bed, the equivalent channel width, w, needs to be determined. At the limit of zero gravity, the governing impregnation equation of a uniform channel simplifies as:

$$x^2 = -\frac{2w\sigma\cos\theta}{3\mu}t. \qquad (3.5.2)$$

Equation (3.5.2) can be nondimensionlized and rearranged to obtain the width of the channel as:

$$\overline{w} = \frac{w}{r} = \frac{C^2}{cos\theta}, \tag{3.5.3}$$

where C is the slope of the impregnation height, $\overline{h}$, vs. $\sqrt{T}$ curve. After the channel width, $\overline{w}$ is obtained, the permeability, $\overline{K}$, is expressed as:

$$\overline{K} = \frac{C^4}{3\cos^2\theta}. \tag{3.5.4}$$

Equation (3.5.4) makes it possible to calculate the permeability of a fiber bed from its capillary impregnation behavior. The slope of the impregnation height vs. $\sqrt{T}$ can be numerically obtained from Figs. 3.9-3.11, and be used in Eq. (3.5.4) to evaluate the permeability.

The permeability obtained in this study is applicable when the fiber volume fraction is high (i.e., for θ $=0$, see Eq. (3.3.8)). Experimental data from Ahn et al. (1991) give the permeability of a fiber bed with high fiber volume fraction. Also lubrication model has been used to determine the permeability of a fiber bed when fiber volume fraction is high. One of the recent models for permeability of a hexagonal fiber bed is developed by Bruschke (1992). The nondimensional permeability, K/r^2, is defined as:

$$\bar{K} = \frac{1}{3\sqrt{3}}\frac{1}{\mu}\frac{(1-l)^2}{l^3}\left(3l\frac{\arctan(\sqrt{(1+l)/(1-l)})}{\sqrt{1-l^2}}+\frac{l^2}{2}+1\right)^{-1} \tag{3.5.5}$$

$$l = \frac{2\sqrt{3}}{\pi}\,v_f \quad . \tag{3.5.6}$$

The nondimensional permeability $\bar{K}$ obtained from Eq. (3.5.4) is shown in Fig. 3.12 as a function of porosity, e ($e=1-v_f$). For higher porosity values, capillary impregnation will not occur due to geometric constraints, thus for e>0.32 permeability cannot be predicted. The lower bound of porosity for permeability prediction is determined by the maximum packing of hexagonal arrangement (i.e., 0.09). The permeability results obtained in this study are compared with the results obtained from the lubrication model given by Eq. (3.5.5) as well as the experimental permeability data from Ahn et al. (1991) as shown in Fig. 3.12. Ahn et al. used T-300 carbon fibers with 7 μm diameter to measure the permeability of a porous fiber bed. Figure 3.12 depicts good agreement between the calculated and measured permeability values. It is also observed that permeability predictions from our model yield slightly better agreement with experiments compared to lubrication model predictions. Transverse permeability of this hexagonal arranged fiber bed is shown to increase by 14.5 times as the porosity is increased from 15 to 30%.

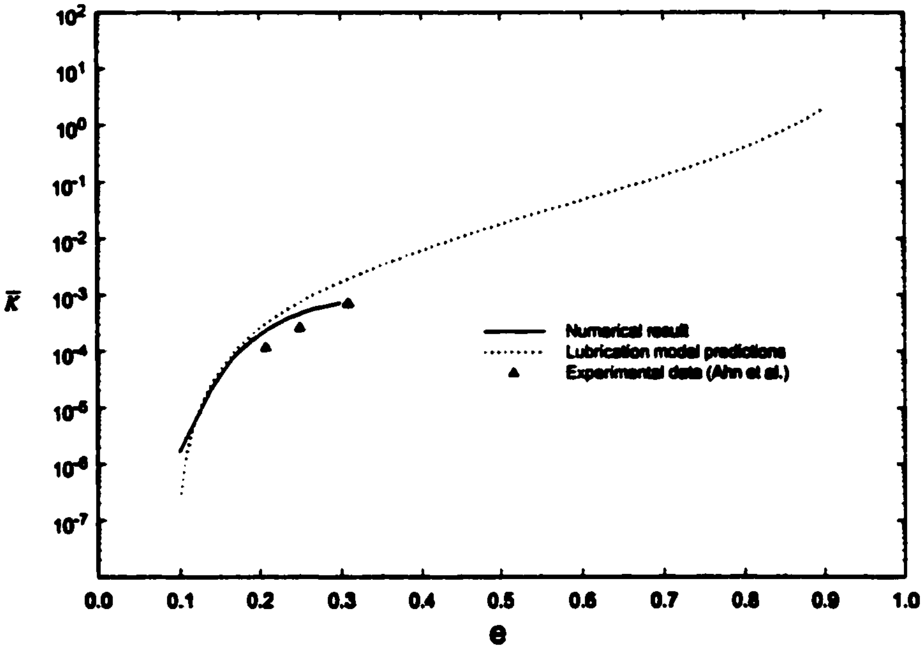

Figure 3.12 Comparison of permeability predictions obtained from current study with lubrication model and experimental data. $e = 1 - v_f$.

3.5 Conclusion

Quasi-static capillary impregnation of a fiber bed in a gravity field is analyzed. The impregnation height and velocity is obtained as a function of contact angle, fiber volume fraction, and Bond number. Gravity effect on the impregnation velocity is found to be significant only during the final stage of impregnation. As the fiber volume fraction is increased, impregnation velocity is found to decrease. Decreasing contact angle between the fluid and the porous fiber bed increases the capillary pressure, thus accelerating the impregnation process. Depending on the Bond number, the impregnation velocity is shown to decrease with time as the capillary pressure is balanced by the gravity. Impregnation velocity is also used to obtain the permeability of the fiber bed. Permeability prediction is compared with the experimental data and the lubrication theory and good agreement is observed.

Chapter 4 TRANSVERSE IMPREGNATION OF AN ANISOTROPIC FIBER BED BY CAPILLARY FORCES

4.1 Introduction

Capillary motion of a fluid through simple geometries such as a circular tube and a two-dimensional channel has been extensively used in modeling flow through porous media in many engineering fields. A commonly used porous medium is a so-called fiber bed, where continuous cylindrical fibers are arranged in a particular pattern. The length of each fiber is much larger than its radius, thus forming an anisotropic medium. When fiber are parallel in a fiber bed, the anisotropy is defined by the microstructure (i.e., fiber arrangement pattern) in the transverse plane. Therefore, unlike other porous media such as rock or soil in which the pores in the media are structurally isotropic, a fiber bed formed by parallel cylindrical fibers is either transversely isotropic or orthotropic.

The anisotropy of the fiber bed structure changes the value of the capillary forces. When capillary flow is along fiber axis, the perimeter of the fluid surface is comparable to the fiber radius. For this case, capillary flow can be studied using the Washburn's equation (1921) of quasi-static fluid front motion through a circular tube. When capillary flow is normal to the fiber axis, the length of the free surface between fibers is much smaller than fiber radius. Bayramli and Powell (1990) used quasi-static capillary motion in a two-dimensional channel to study the capillary impregnation. In Bayramli and Powell's study, the gravity effect is neglected and the fiber bed is assumed to be isotropic in the plane transverse to the fiber axis. He and Altan (2000) included gravity effect to the impregnation of the same fiber bed. The locations and shapes of the fluid front during the capillary impregnation can be predicted and the permeability of the fiber bed can be obtained. In both of these studies, only one flow direction is considered. Therefore, the anisotropy of the transverse permeability can not be observed.

The anisotropy of the fiber bed permeability can be experimentally observed by observing the change of the fluid front location with time along different flow directions. In the study of permeability of multilayer fabrics, Adams and Rebenfeld (1991) first measured the permeability of a single layer of fabric. Their data showed anisotropy of permeability when fibers are unidirectionally arranged. If fibers are randomly distributed as in a fiber mat, the permeability was shown to be isotropic. Gebart and Lidstrom (1996) used parallel molds to measure the anisotropic permeability of fiber beds. Fibers in these molds are placed in different directions relative to the incoming flow. Therefore, for a certain direction of incoming flow, the dynamics of the flow is different. The anisotropic permeability of the fiber beds can be obtained using Darcy's law and the flow velocity in the prospective mold. They found that the permeability could change as much as 23 times when the direction of flow changes 90 degrees. A different method of measuring the anisotropic permeability was performed by Chan et al (1993). In this work, the anisotropic permeability of a fiber bed was obtained by observing the fluid front shape during the radial filling of a fiber bed. Fluid front showed an ellipsoid shape during the filling process. The values of the principal permeabilities were calculated using Darcy's law and time rate change of the principal axes of the fluid front ellipse. Larson and Higdon (1987) numerically calculated the flow field in hexagonal and cubic arrangement cell with different flow directions. Their results show that the flow field changes dramatically when flow direction is changed. Larson and Higdon (1987) also calculated the anisotropic transverse permeability by changing the cross-sectional shape of the fiber from circular to ellipsoid. Their results show that the principal permeability of a fiber bed changes with the ratio of the two principal axes of the ellipses and the inclination angle of the packing.

This work investigates the capillary impregnation of an anisotropic fiber bed. Fibers are arranged in an isosceles triangular pattern. It is found that the flow velocity changes with fiber arrangement, fiber volume fraction and contact angle. Fluid front locations and shapes during the capillary impregnation are presented. Transverse permeability is obtained using the macroscopic flow velocity. It is found that the transverse permeability may vary up to two orders of magnitude, depending on the fiber arrangement pattern and fiber volume fraction. The results of the current study are found to agree with experimental observation available in the literature.

4.2 Fiber Packing Pattern

Current study analyzes capillary impregnation through regularly arranged fibers shown in Fig. 4.1. The impregnation takes place in the direction opposite to gravity. In Fig. 4.1, distance d_1 and d_2 represent half of fiber separation within one layer and the distance between two consecutive layers, respectively. Among consecutive layers, fibers form repeating isosceles triangles shown as triangle *BCD* in Fig. 4.1. The bottom angel of such arrangement is β (see Fig.4.1). If the same fiber bed is turned 90 degrees, flow along the same direction passes through a different geometry shown as triangle *ADC*.

The bottom angle now becomes $\pi/2-\beta$. Therefore, changing the the bottom angle β, of fiber arrangement to its complementary value does not change the fiber arrangement pattern. In this study, the range of β is chosen to be from $\pi/4$ to $\pi/2$.

The geometric condition to have capillary impregnation possible for a hexagonal fiber bed was discussed by He and Altan (2000). Similar discussion for an isosceles triangular fiber arrangement pattern is presented here. First, the lower bound of fiber volume fraction is obtained for different contact angles between fiber surface and the impregnating fluid. The same method as in He and Altan's work is used in this study for the impregnation of an anisotropic fiber bed. Since flow passes through a different geometry as the fiber bed is turned 90 degrees. The lower bound of the fiber volume fraction is chosen such that the capillary impregnation is possible for both geometries. Then the upper bound of the fiber volume fraction representing fiber touching each other in the fiber bed is obtained. The general expression of fiber volume fraction in terms of d_1, d_2, and fiber radius r can be written as:

$$v_f = \frac{\pi r^2}{2 d_1 d_2}. \tag{4.2.1}$$

The possible ways of fibers in touch with each other and the respective fiber volume fractions are (see Figure 4.1):

Fiber A touches fiber D:

$$d_2 = r \qquad\qquad v_f = \frac{\pi \tan\beta}{2}; \tag{4.2.2}$$

fiber B touches fiber C:

$$d_1 = 2r \qquad\qquad v_f = \frac{\pi}{2\tan\beta}; \tag{4.2.3}$$

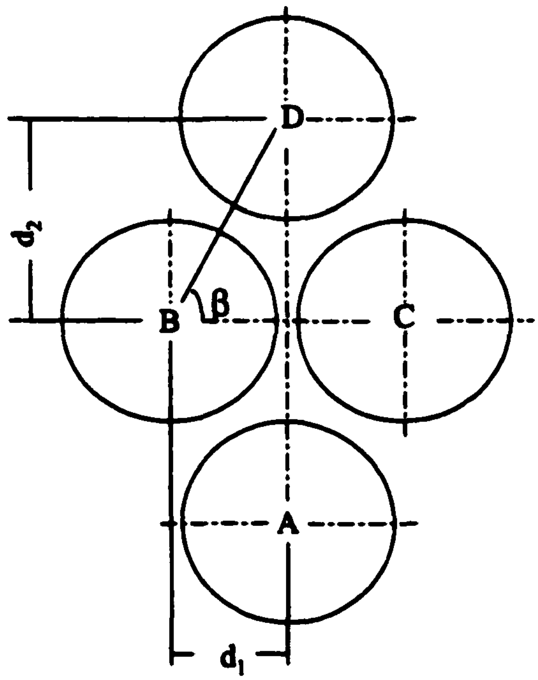

Figure 4.1 Fiber arrangement pattern used in this study.

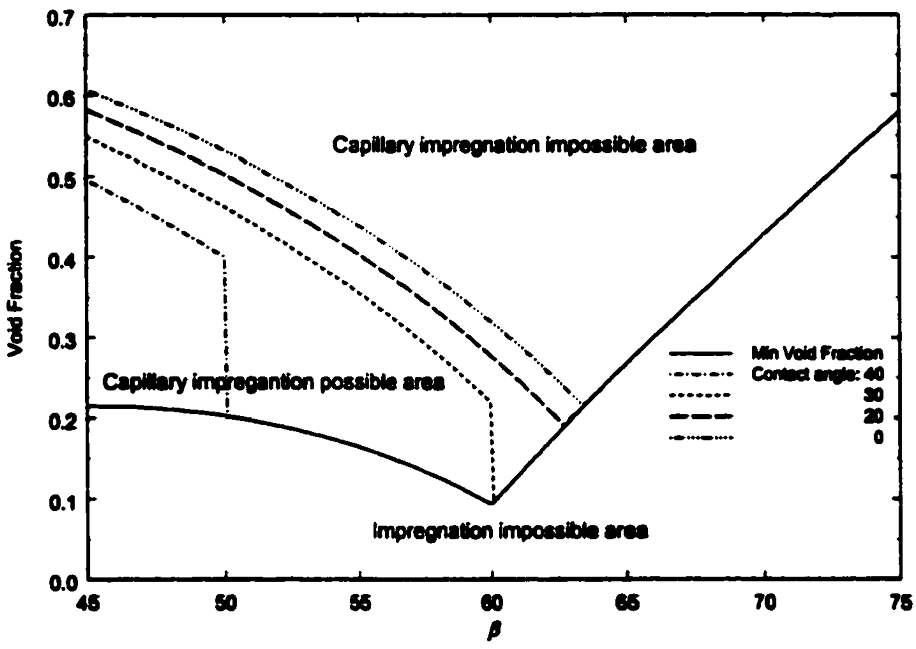

Figure 4.2 Fiber arrangement criteria for possible capillary impregnation using different contact angles.

fiber B touches fiber D:

$$\cos\beta = \frac{d_1}{2r} \qquad v_f = \frac{\pi}{4\sin 2\beta}. \tag{4.2.4}$$

If fibers touch each other in any of the above three ways, capillary impregnation is impossible. So in order for fibers not to touch each other, the fiber volume fraction, v_f, should be less than the minimum value calculated from Eqs. (4.2.2)-(4.2.4), for a certain packing angle β.

Figure 4.2 shows the criteria of fiber arrangement pattern for possible impregnation discussed above. The area below the V shaped solid line represents that fiber volume fraction is higher than the upper bound of its arrangement pattern. All other curves represent the lower bound of the fiber volume fraction, depending on the contact angle. So capillary impregnation can only take place in the range of fiber volume fraction between these two limits. If fiber volume fraction is lower than its lower bound, some external effort such as external pressure is needed to impregnate the fiber bed. On the other hand, if the fiber volume fraction is higher than its upper bound, no impregnation is possible through the fiber bed.

4.3 Anisotropic Capillary Impregnation of a Fiber Bed

When fiber arrangement pattern and contact angle are within the range mentioned above, fluid can be driven by capillary forces to impregnate the fiber bed.

The final position that the fluid front can reach depends on the balance of capillary forces with gravity. Such impregnation can be molded by the quasi-static creeping flow in a two-dimensional channel. The width of the channel changes periodically according to the fiber arrangement pattern. For capillary flow in a uniform channel in a gravity field, He and Altan's (2000) study gave the governing equation describing the fluid front location with time. This governing equation is nondimensionlized as:

$$T = \frac{2}{B}(X + X_f \ln(1 - \frac{X}{X_f})) \tag{4.3.1}$$

The nondimensional parameters are related to the fiber arrangement parameters and fluid properties as:

$$X = \frac{x}{r}, \tag{4.3.2}$$

$$T = \frac{2\sigma t}{3\mu r}, \tag{4.3.3}$$

$$B = \frac{\rho g w^2}{\sigma}, \tag{4.3.4}$$

$$X_f = \frac{\sigma \cos\alpha}{\rho g w r}. \tag{4.3.5}$$

where σ, ρ, and μ are surface tension, density and dynamic viscosity of the fluid. X is impregnation distance; t is time; b is half channel width; g is gravity; and θ is contact angle, respectively. When the channel is uniform, the parameter w in Eq. (4.3.4) is a constant. If capillary flow takes place through a fiber bed, the channel width changes because of the circular shape of the fiber surface. The free surface shape remains circular with its radius changing according to the varying channel width during the impregnation process. When the fiber bed is turned 90 degrees, the geometry through which the fluid flows is changed. Such change of the geometry changes the value of the capillary forces at each location of the fluid front. Therefore, the impregnation velocity is different. Each channel between fiber surfaces is divided into small segments of parallel channel channels. Equation (4.3.1) is used in the calculation of flow through these parallel channels. Such method of determining fluid front shape and location is the same as in Bayramly and Powell's work (1990)

Impregnation dynamics is affected by the packing angle β, fiber volume fraction v_f, contact angle θ, and gravity . The gravity effect can be represented by the nondimensional Bond number Bo ($Bo= \rho g d^2/\sigma$, where d is half fiber separation distance). As one can see from Fig. 4.2, capillary impregnation won't be possible for β greater than 63.43^0 or less than 26.57^0. Three values of angle β of: 45^0, 50^0, and 60^0, are chosen in the impregnation analysis.

4.4 Results of Fluid Front Motion

The result of the fluid front motion is expressed in terms of the nondimensional impregnation height, $\bar{h}$ ($\bar{h} = h/r$, where h is the vertical height of the fluid front), with the square root of the nondimensional time, $\sqrt{T}$. Since fluid front is circular during the impregnation process, one can predict the fluid front shape at different times when the fluid front location is obtained. When the same fiber bed is turned 90 degrees, the dynamics of the flow along the same direction changes due to the change of the geometry of the flow domain. Figs. 4.3-4.4 show the fluid front shapes and location at equal steps of the square root of dimensionless time. Angle β used in Fig. 3 is 60 degrees and fiber volume fraction is 70%. The same fiber bed is turned 90 degrees and the fluid front motion is shown in Fig. 4.4. Contact angle used in both figures is zero degree. The change of geometry of flow domain and fluid front shape can be observed by comparing these two figures. When the same fiber bed as in Fig. 4.3 is turned 90 degrees, Bond number changes from 5.72×10^{-8} to 1.72×10^{-7}. According to He and Altan's study, gravity only affect the impregnation at the final stage of the impregnation. Therefore, the effect of gravity to the impregnation process in both Figs. 4.3-4.4 is negligible. At the initial stage of the impregnation, the impregnation height, h, changes linearly with the square root of time. Such linearity of fluid front with time is shown in Fig. 4.5, in which two curves show the initial impregnation height with the square root of dimensionless time for the impregnation process in Figs. 4.3-4.4. It can be seen that the impregnation dynamics is significantly different when the fiber bed is turned 90 degrees.

The effect of gravity to the impregnation is shown in figs. 4.6-4.7. Figures 4.6-4.7 show the impregnation velocity v ($v = d\bar{h}/dT$) with T during the impregnation of hexagonal fiber bed (β=60^0) for different fiber volume fractions, bond numbers, and contact angles. It can be observed from these figures that the impregnation velocity is decreasing with time. The rate of velocity change with time depends on fiber volume fraction, Bond number and contact angle. At the final position of the impregnation where gravity balances capillary forces, the impregnation velocity reaches to zero. The smallest value of Bond number used is Bo=5.72$\times$10^{-8} both in Fig. 4.6 and Fig. 4.7. Then this Bond number value is increased to 2, 5, and 10 times to compare the impregnation velocity. In Fig. 4.6, fiber volume fractions, 70% and 80%, are used. Contact angle is kept at zero. It can be seen that the increase of fiber volume fraction decreases the impregnation velocity at each time and increase the total impregnation time. Fiber volume fraction used in Fig. 4.7 is 85%. Contact angles of 0, 10, and 20 degrees are use din the figure. Decrease in contact angle increases the value of the capillary forces in the flow direction. Therefore, the flow velocity is increased. Final height of the fluid front is decreased when contact angle is increased. It is shown in Fig. 4.7 that the total impregnation time decreases with increasing contact angle.

Angle β, of the fiber arrangement pattern can also change the dynamics of capillary impregnation of a fiber bed. The fiber arrangement pattern in Fig. 4.8 is different from that of Figs 4.4-4.5. Angle β and fiber volume fraction in Fig. 4.8 are 45 degrees and 70%, respectively. Change of β changes the geometry of the flow domain. Therefore, the values of the capillary forces are changed. It can be seen that the flow dynamics is different compared with Figs.4.3-4.4. For the fiber arrangement pattern shown in Fig. 4.8, the geometry of the flow domain does not change when the fiber bed is turned 90 degrees. Fluid front shapes and locations at each time of the impregnation will not change when the fiber bed is turned 90 degrees.

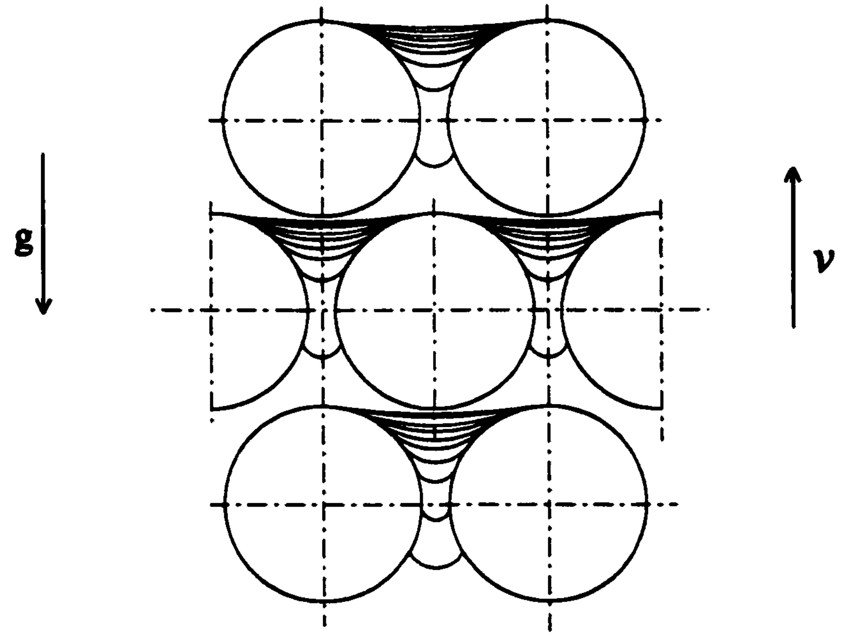

Figure 4.3 Location and shape of the fluid fronts at different times during capillary impregnation. $v_f = 70\%$; $\beta = 60°$; $\theta = 0°$.

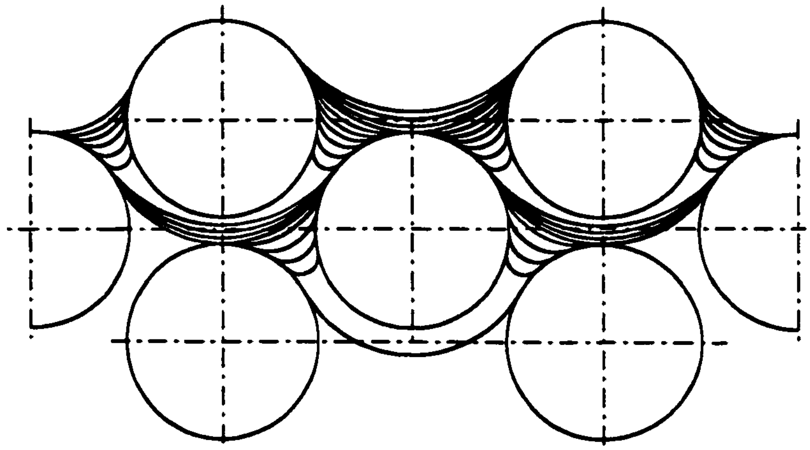

Figure 4.4 Location and shape of the fluid fronts at different times during capillary impregnation. ν_f **= 70%;** $\beta = 30°$; $\theta = 0°$.

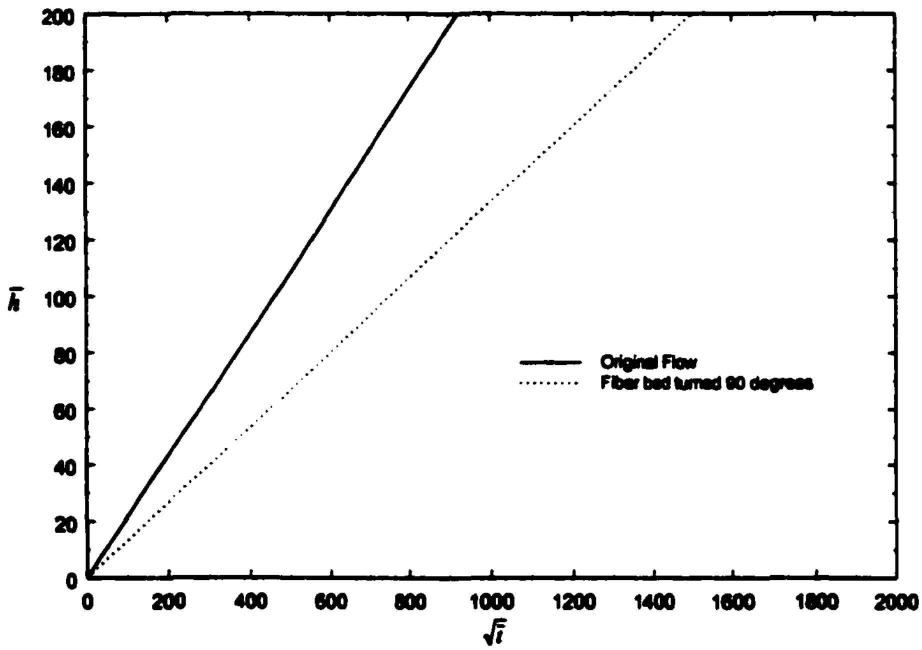

Figure 4.5 Change of impregnation height with time during impregnation for different flow directions. $v_f = 70\%$; $\beta = 60^0; \theta = 0^o$.

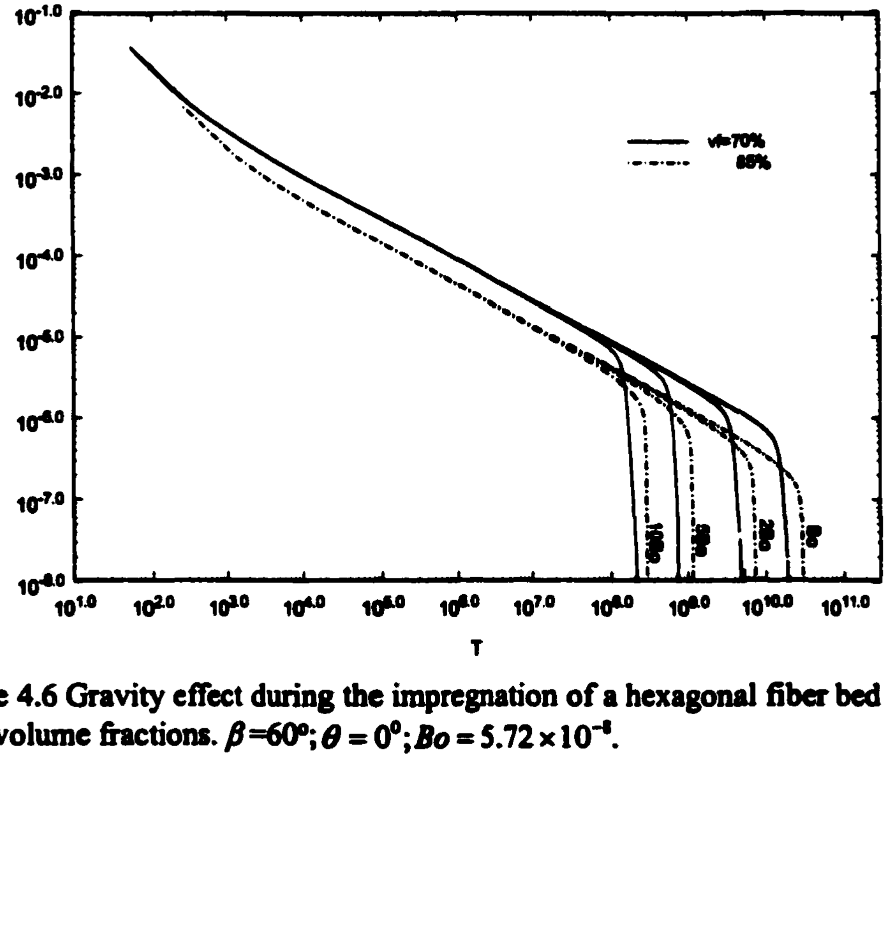

Figure 4.6 Gravity effect during the impregnation of a hexagonal fiber bed for different fiber volume fractions. β=60°; $\theta = 0^0$; $Bo = 5.72\times10^{-8}$.

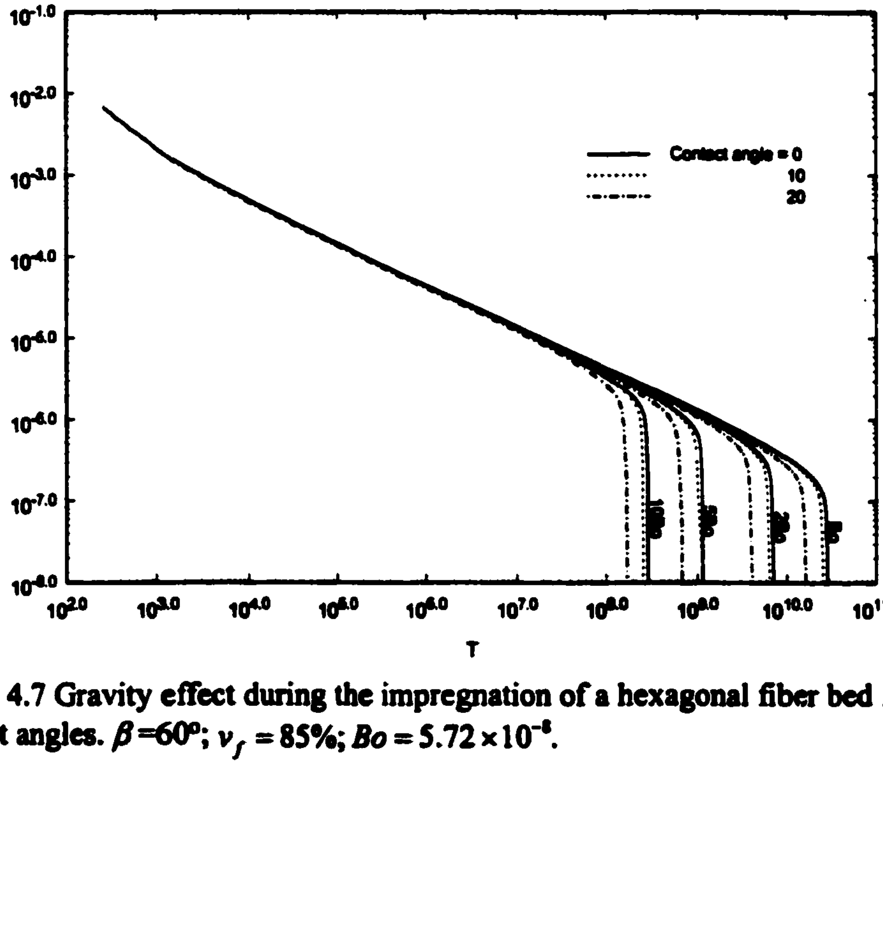

Figure 4.7 Gravity effect during the impregnation of a hexagonal fiber bed for different contact angles. β=60°; $v_f = 85\%$; $Bo = 5.72 \times 10^{-8}$.

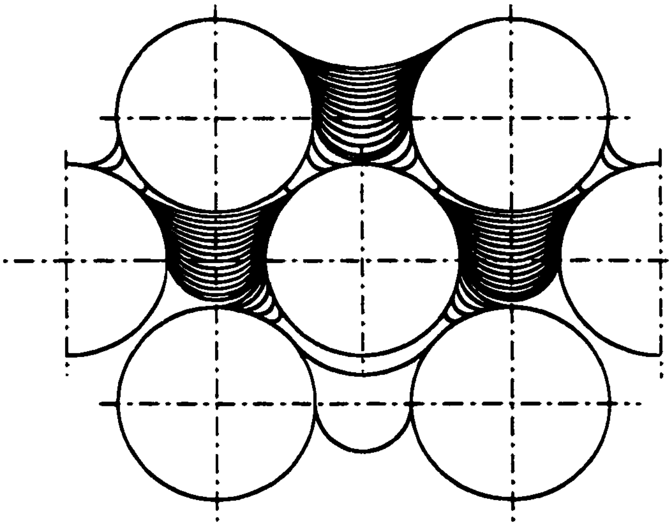

Figure 4.8 Location and shape of the fluid fronts at different times during capillary impregnation. $v_f = 70\%$; $\beta = 45°$; $\theta = 0°$.

4.5 Prediction of the Anisotropic Permeability of a Fiber Bed

The permeability of a fiber bed can be obtained using the slope of the fluid front height with the square root of time shown in Fig. 4.5 (He and Altan, 2000). Usually, the permeability of a fiber bed is nondimensiolized with the fiber radius. The dimensionless fiber bed permeability is related with the slope C, of the fluid front height with square root of time as:

$$\overline{\mathrm{K}} = \frac{K}{r^2} = \frac{\mathrm{C}^4}{3(\cos\theta)^2}. \tag{4.5.1}$$

As pointed out before, the flow dynamics is different for different fiber packing angle, β, even for the same fiber volume fraction. Thus, permeability of a fiber bed is the function of fiber volume fraction and angle β. Anisotropic permeability and their change with fiber volume fraction are shown in Figs 4.9-4.10 for different values of β. In these figures, $\overline{\mathrm{K}}_x$ represents fiber bed permeability with fiber bed not turned. If the fiber bed is turned 90 degrees, the permeability is represented as $\overline{\mathrm{K}}_y$. Both figures show that permeability decreases when fiber volume fraction is increased.

Most work in the literature used circular tube to simulate flow along fiber axis direction. This method is also used in this study. The radius of the tube is obtained by calculating the radius of a circular tube that can fit into the space among three adjacent fibers (See Fig. 4.11). The equation of obtaining this radius can be written as:

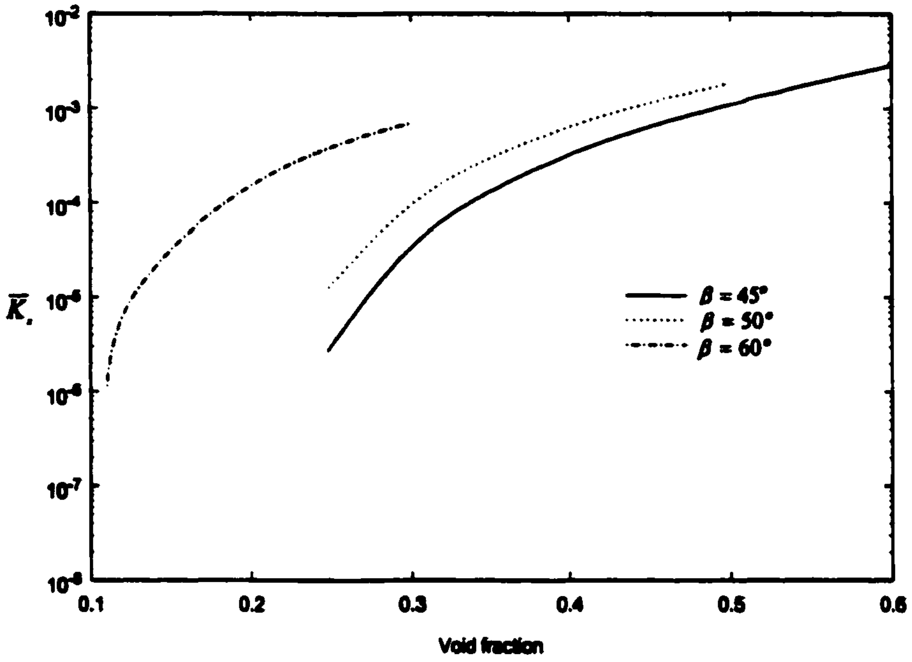

Figure 4.9 Permeability $\overline{K}_x$ prediction with fiber volume fraction for different packing angles.

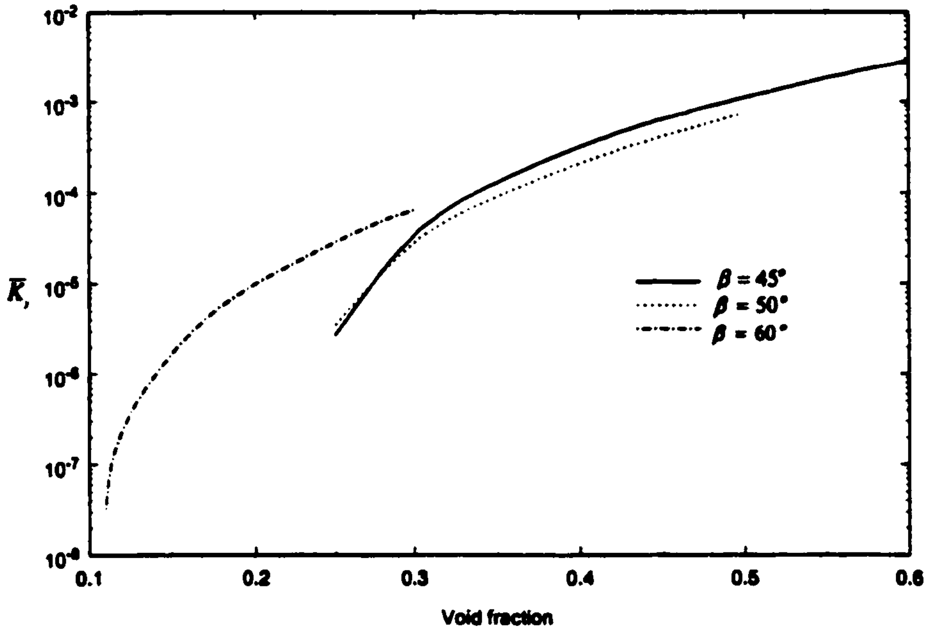

Figure 4.10 Permeability $\overline{K}_y$ prediction with fiber volume fraction for different packing angles.

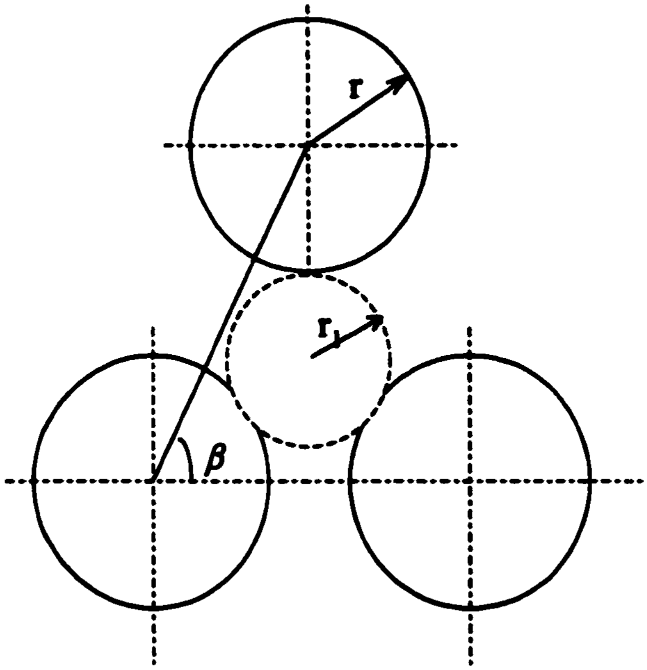

Figure 4.11 Fitting of a circular tube into space among fibers to calculate longitudinal permeability.

β			
45	40%	42.59	42.59
	45%	50.61	50.61
	50%	66.77	66.77
	55%	92.32	92.32
	60%	148.64	148.64
	65%	296.83	296.83
	70%	890.81	890.81
50	50%	54.93	32.83
	55%	77.59	35.18
	60%	120.35	53.01
	65%	223.17	84.82
	70%	568.89	203.18
60	70%	125.37	17.74
	75%	220.23	23.91
	80%	491.03	43.69
	85%	2210.9	145.09

$$\bar{r}_1 = \frac{r_1}{r} = \sqrt{\frac{\pi}{2v_f \tan\beta}(\tan\beta - \tan\alpha)} - 1 \qquad (4.5.2)$$

$$\alpha = 2\arctan\left(\frac{-2+\sqrt{4-4(1-\tan^2\beta)}}{2(1+\tan\beta)}\right) \qquad (4.5.3)$$

The longitudinal permeability is obtained using the following equation (Kolosov, 1988):

$$\bar{K}_z = \frac{r_1^2}{8}. \qquad (4.5.4)$$

Table 4.1 shows the ratio of longitudinal to normal permeability for different fiber arrangement patterns. For a certain fiber arrangement pattern, the ratio of longitudinal to normal permeability increases with the increase of fiber volume fraction, as shown in table 4.1. Also, longitudinal permeability is always greater than the normal permeability. Most ratios of the permeabilities are within two orders of magnitude.

Different researchers have performed experimental observations of permeability. Some of their results show in the form of the ratio of permeability in different directions. Foe example, Gebart and Lidstorm (1996) found that the permeability changes 23 times when flow direction changes 90 degrees. Lam and Kardos's (1988) experiment showed the ratio of longitudinal to normal permeability to be 19. Gutowski et al's (1987) results show this ratio to be 25 or higher. The possible answer to these observations is that flow direction is not along the designed direction. The ratio of permeability can be anywhere between the value of $\overline{K}_z / \overline{K}_x$ and $\overline{K}_z / \overline{K}_y$. Also the variation of packing angle, β, contributes to the variation in the ratio of permeability.

4.6 Conclusion

Capillary impregnation of an anisotropic fiber bed is analyzed. Fluid front locations and shapes during impregnation are obtained. Flow velocity changes periodically during the impregnation. Gravity effect slows down the impregnation and finally stops the process at the location where gravity and capillary forces are balanced. The velocity of the fluid front motion is found to change with fiber volume fraction, contact angle and fiber arrangement pattern. Anisotropic transverse permeability is obtained using impregnation velocity. The ratios of longitudinal to transverse permeability are found to be within two orders of magnitude. The results of current are found to agree with experimental observations.

Chapter 5 FIBER BED IMPREGNATION WITH EXTERNAL PRESSURE AND PERMEABILITY USING EXTENDED LUBRICATION THEORY

5.1 Introduction

Fluid motion through a fiber bed is a dynamic balance among various forces that act on the fluid. When capillary forces drive the impregnation, the dynamic change of the fluid front shape changes the pressure that drive the flow. Since surface tension forces dominate viscous forces in capillary impregnation, flow can be viewed as quasi-static. The free surface shape at every location is the same as its static shape. The change in the shape of the free surface at different times of the impregnation is due to the curved shape of the fiber surfaces that cause the change of the geometry of the flow domain. Research on capillary impregnation using such quasi-static assumption were found to agree with experimental data (Bayramli and Powell, 1990; Williams et. al, 1971). However, experimental works (Hoffman, 1975) found that even during the capillary driven flow, the free surface deviates from its static shape. The change of free surface shape from its static shape depends on the capillary number during the flow. Capillary number decreases during the capillary impregnation, and asymptotically reaches zero. Therefore, the deviation of free surface shape from its static shape is more likely to happen during the initial stage of the flow. For a small bond number flow, experimental evidence show that even though free surface shape appears to be different from the static shape, its shape remains to be circular. The only change is the radius of the curve. Joos et al's (1990) work included the dynamic change of the free surface shape to calculate the fluid front motion during capillary impregnation. Their results are found to match well with the experiments. When capillary number reaches to a certain level, it is shown that viscous force effect on the shape of the free surface will appear. At this stage, the free surface shape will no longer be circular (Hoffman, 1975).

Analyzing capillary flow in a fiber bed, an important physical parameter of the fiber bed, permeability can be obtained and compared directly with the experimental observation. Good agreement has been found between the numerical calculation and experimental results in Bayramli and Powell's work. In Chapters 3 and 4, capillary impregnation including gravity effects is also found to agree with experimental results in permeability predictions.

In previous chapters, it was pointed out that the permeability of a fiber bed could be predicted theoretically using either cell model or lubrication model depending on fiber volume fraction. When lubrication model is used in the permeability prediction, fiber volume fraction needs to be high. During the past few decades, researchers have tried to simplify the equation that leads to the permeability prediction of a fiber bed (Keller, 1959; Gebart, 1992). Recently, Bruschke (1992) gave the analytical expression of the permeability calculation for hexagonal and square arranged fiber beds. Bruschke also suggested a closed form equation for permeability prediction such that the permeability could be dominated by the term from cell model when fiber volume fraction is low while the permeability is dominated by the term from lubrication model when the fiber volume fraction is high. At the range of intermediate value of fiber volume fraction, both cell model and lubrication model contributes to the permeability prediction. However, as pointed out in the previous chapters, if the fiber volume fraction reaches a certain level, previous research of predicting fiber bed permeability needs to be reconsidered.

This chapter first calculates the impregnation of a hexagonal fiber bed. Different from the previous work, a small value of external pressure is applied to combine with the capillary pressure to drive the flow. Dynamic change of the fluid front is included in the analysis as was done in chapter 4. The value of the external pressure is chosen such that the free surface shape keeps circular. It is shown that during the pressure driven flow through the fiber bed, the free surface change due to capillary number can sometimes change the direction of the capillary forces. Therefore, it is possible that during certain stage of the flow, the capillary force starts resisting the flow instead of driving it.

The second part of this chapter studies the permeability prediction using lubrication model. Previous research results of permeability prediction are discussed when fibers are squarely or hexagonally arranged in a fiber bed. If the fiber volume fraction reaches the level where the previous method is not valid, a new approach is suggested to predict the permeability of a fiber bed. The arrangement of fibers in the fiber bed is extended from hexagonal and square patterns to isosceles triangular and rectangular patterns. Anisotropic permeability of the fiber bed can be predicted based on the suggested method. The result of the permeability prediction is found to agree with the previous calculation of permeability based on the capillary impregnation of a fiber bed.

5.2 Impregnation of a Fiber Bed with External Pressure

5.2.1 Fluid Front Motion and Shape Change

During pressure driven impregnation flow of a fiber bed, the change of the location and shape of the free surface depends on the pressure forces that drive the flow, the viscosity and surface tension of the fluid, and the static contact angle between the fluid and solid surface. When the free surface is circular, this dynamic change of the fluid front can be represented as the location and the dynamic contact angle of the free surface. Chapter 3 gave the detailed derivation of the governing equation of fluid front motion during the pressure driven flow. Since capillary forces are the only forces to drive the flow, the pressure gradient term in Eq. (3.2.5) includes capillary pressure only. Similarly, the governing equation for impregnation of a uniform channel with external pressure P_{ex} and capillary pressure can be obtained by adding one more term in Eq. (3.2.5). After a similar procedure of integration and rearrangement, the governing equation becomes:

$$y - \frac{p_{ex} - \sigma/r_l}{\rho g} \ln(1 + \frac{\rho g y}{p_{ex} - \sigma/r_l}) = -\frac{\rho g b^2}{3\mu} t. \qquad (5.2.1)$$

Equation (5.2.1) shows the impregnation of a uniform channel with external pressure and capillary forces. Compared with Eq. (3.2.5), one can see that the final height that the free surface can reach varies as the external pressure is introduced to push the flow. When the external pressure p_{ex} is zero, Eq. (5.2.1) simplifies to Eq. (3.2.5). similar to the derivation in chapter 3, the governing equation is nondimensionlized in order to obtain the general expression of nondimensional fluid front position with nondimensional time. The nondimensional parameters used in this chapter are:

$$\bar{y}=\frac{y}{r}; \tag{5.2.2}$$

$$\bar{y}_f=\frac{P_{ex}-\sigma/r_l}{\rho g r}; \tag{5.2.3}$$

$$\bar{t}=\frac{2\sigma}{3\mu r}t; \tag{5.2.4}$$

$$B=\frac{\rho g w^2}{\sigma}. \tag{5.2.5}$$

It can be seen that most of the nondimensional parameters used in this chapter are the same as in chapter 3. The fiber arrangement is the same as in chapter 3 with the geometric parameters shown in Fig. 3.4. A new parameter is introduced to represent the external pressure that drives the flow. This new parameter is the ratio of the external pressure to the maximum capillary pressure during the impregnation. The maximum capillary pressure is the one when the distance between two fiber surfaces is the minimum. For the same fiber structure used in chapter 3, the maximum capillary pressure is (when contact angle is zero):

$$P=\frac{\sigma}{d}. \tag{5.2.6}$$

The ratio of external pressure to the maximum capillary pressure is defined as:

$$\delta=\frac{P_{ex}d}{\sigma}. \tag{5.2.7}$$

The nondimensionlized governing equation for impregnation with external pressure and capillary forces has the same form as in chapter 3. This governing equation is written as:

$$\bar{t} = \frac{2}{B}(\bar{y} + \bar{y}_f\, ln(1 - \frac{\bar{y}}{\bar{y}_f})). \tag{5.2.8}$$

The consideration of dynamic contact angle uses the empirical equation from Jiang et al (1975). This equation calculates the dynamic contact angle as a function of the capillary number. It is written as:

$$\frac{\cos\theta_s - \cos\theta_d}{\cos\theta_s + 1} = \tanh(4.96\, Ca^{0.702}). \tag{5.2.9}$$

Equation (5.2.9) is based on the collection of experimental data from Hoffman (1975). An important observation of Hoffman's work is that all these data fit only for low capillary number and low Weber number We (a dimensionless parameter of the ratio of inertia forces to capillary forces) flow. Experimental evidences show that for capillary number greater than 36 and Weber number greater than 1.6×10^{-5}, free surface shape deviates from a circular one (Hoffman, 1975). For the calculation of this chapter, the choice of external pressure is limited such that the capillary numbers and Weber numbers can fall into this range. The free surface shape is assumed to be circular during the whole impregnation. The continuous and discontinuous model of the fluid front motion is the same as in chapter 3.

5.2.2 Fluid Front Shapes and Locations during the Flow

When an external pressure joins capillary pressure to impregnate a fiber bed, flow velocity is greater compared to only capillary driven impregnation. This increased velocity increases the capillary number during the flow. As shown in Eq. (5.2.9), a greater value of capillary number causes the increase in dynamic contact angle. When the dynamic contact angle is greater than 90 degrees, the curvature of the free surface becomes opposite to the flow direction. Thus, capillary forces become part of the resisting force to the flow. Impregnation of a fiber bed with external pressure is calculated using the same numerical method as in chapter 3. The same dimensionless height is used in presenting the results. It is observed that the linearity of the impregnation height with the square root of time still exists. In chapter 3, fluid front shape is assumed as the same as its static shape. Flow velocity doesn't affect the free surface shape at different times of the impregnation. However, since impregnation velocity decreases with time and the dynamic contact angle is taken into consideration in this chapter, the change of fluid front shape due to the change of flow velocity can be observed.

The fluid front shapes and locations at different times of impregnation are shown in Figs. 5.1-5.5. The same fiber volume fraction, 70% and 85%, as in chapter 3 are chosen for the convenience of comparison. Static contact angle is kept at 0 degrees.

Figure 5.1 shows the fluid front shapes and locations during the impregnation when fiber volume fraction is 70%. The external pressure ratio δ is 0.5. Same interval of the square root of time is chosen as in chapter 3. The periodical change of the fluid front velocity can be observed. Comparing with Fig. 3.9, it can be seen that the flow velocity is increased due to the applying of the external pressure. The contact angle at each fluid front location is not kept at 0 degrees. It changes with the flow velocity. At some locations where the flow velocity is greater than other locations, the contact angle appear to be greater than 90 degrees. At these locations, capillary pressure is resisting the flow, as opposed to the capillary impregnation. However, fluid can still flow due to the presence of external pressure.

Figure 5.2 shows the fluid front shapes and locations at different times of impregnation when fiber volume faction is 70%. Different from Fig. 5.1, an external pressure of $\delta = 0.3$ is applied. Static contact angle is kept at 0 degrees. It can be seen that the flow velocity is slower than the one in Fig. 5.1; but it is still greater than the one when capillary pressure is the only driving force. Fluid front shape changes from the static shapes. No contact angle greater than 90 degrees is observed in this figure. The comparison of long term fluid front motion with the square root of time when different external pressures are applied is shown in Fig. 5.3

Figure 5.4 shows the fluid front shapes and locations at different times of impregnation when fiber volume fraction is 85%. Static contact angle is 0 degrees. Comparing with Fig. 3.10; it can be seen that the flow velocity is increased, similar to the previous figures. Also the change of the dynamic contact angle is observed in the figure. The long term fluid front location with the square root of time is shown in Fig. 5.5.

In general, one can conclude that applying of external pressure to the fiber bed impregnation changes both fluid front shape and the impregnation velocity. However, the amount of the external pressure is limited when free surface shape is kept circular. When the value of external pressure increases, the free surface shape deviates from the circular ones. For such cases, different model needs to be used to study the impregnation of fiber bed.

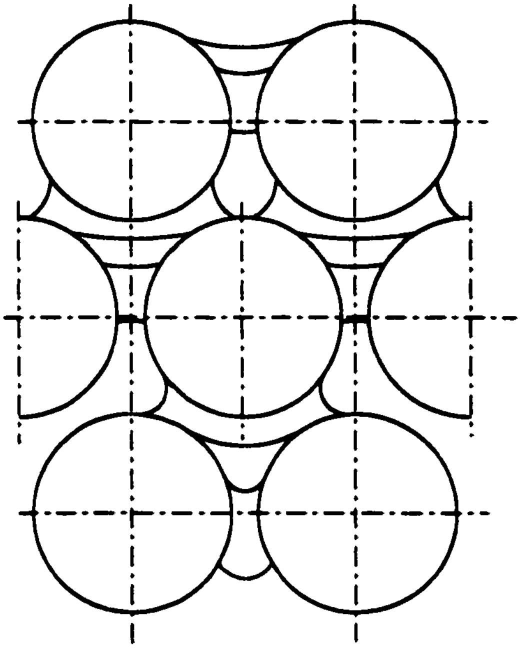

Figure 5.1 Location and shape of the fluid fronts at different times during impregnation for 70% fiber volume fraction. δ=0.5.

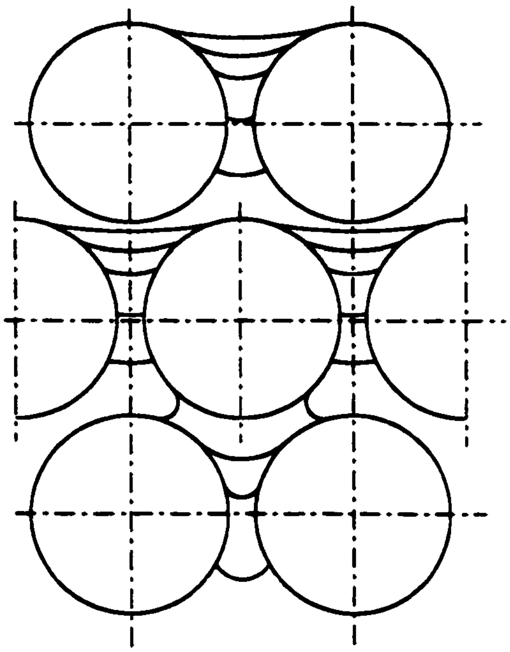

Figure 5.2 Location and shape of the fluid fronts at different times during impregnation for 70% fiber volume fraction. δ=0.3.

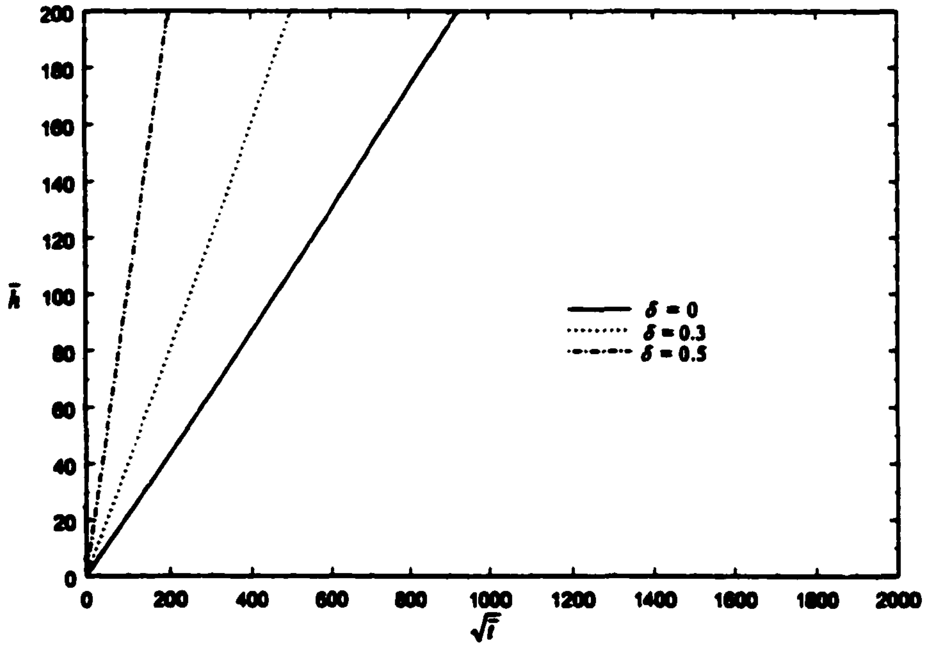

Figure 5.3 Change of vertical impregnation distance during impregnation for different external pressure. v_f=70%.

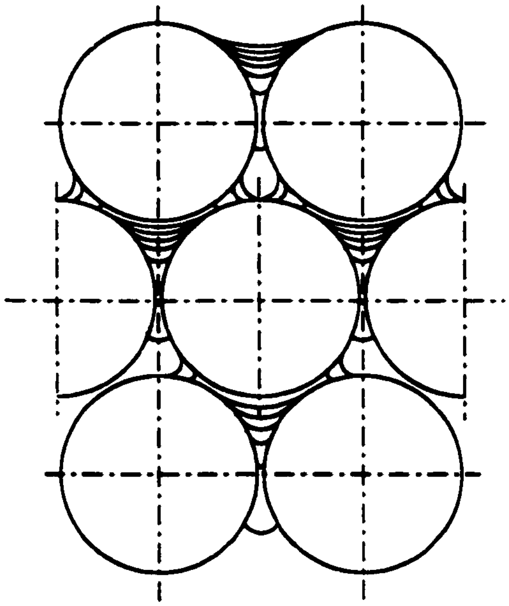

Figure 5.4 Location and shape of the fluid fronts at different times during impregnation for 85% fiber volume fraction. δ=0.1.

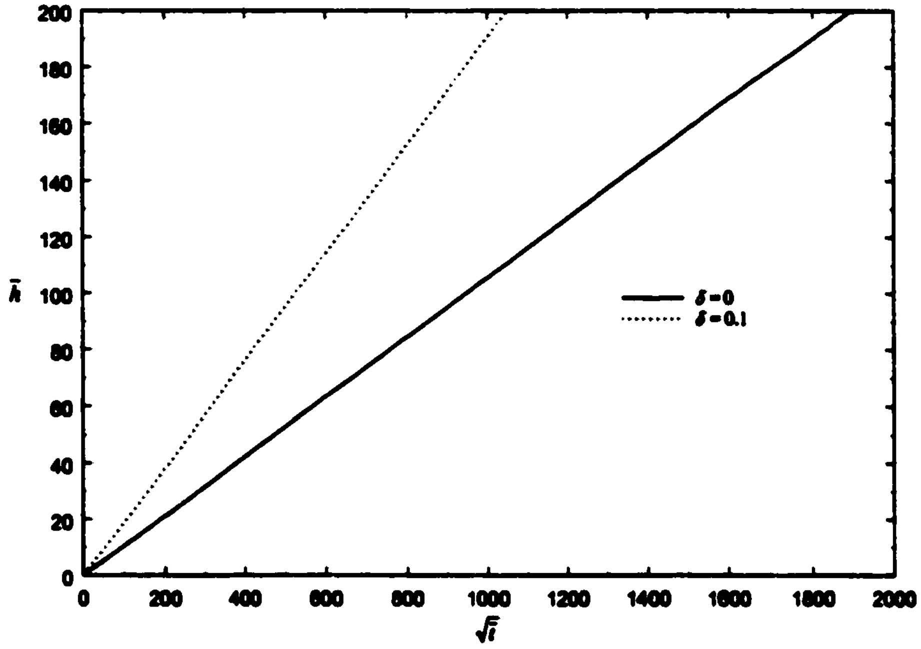

Figure 5.5 Change of vertical impregnation distance during impregnation for different external pressure. v_f=85%.

5.3 Extended Lubrication Model for Fiber Bed Permeability Prediction

5.3.1 Previous Works

Permeability represents the resistance force of a certain porous medium to the external flow. It is a function of the distribution of pores in the medium. For a porous fiber bed, fiber volume fraction and fiber arrangement pattern all contribute to the permeability of the fiber bed. If fibers are arranged in a periodical pattern, one can select a repeating unit cell from this arrangement to analyze the permeability. Lubrication model works for flow analysis in a channel with slowly varying area. Models based on lubrication theory has been used to analyze the in-plane permeability of fiber beds. No analytical solution of permeability prediction had been presented before. Bruschke (1992) obtained the permeability of hexagonal and square fiber beds. In this chapter, some of the previous works of permeability prediction as well as Bruschke's work is discussed. An extension of the permeability prediction is suggested such that the permeability prediction can cover the whole range of fiber volume fraction.

Keller's proposal

Permeability prediction using lubrication model was first proposed by Keller(1964). The scheme of this study is shown in Fig. 5.6. Flow is driven through the cavity between two cylindrical fiber surfaces. Using the coordinate system shown in the figure, the pressure drop across one cylindrical surface for steady state flow can be written as:

$$\frac{dp}{dx}=12\mu Q\frac{1}{\left(d-2\sqrt{R^2-x^2}\right)^3}. \tag{5.3.1}$$

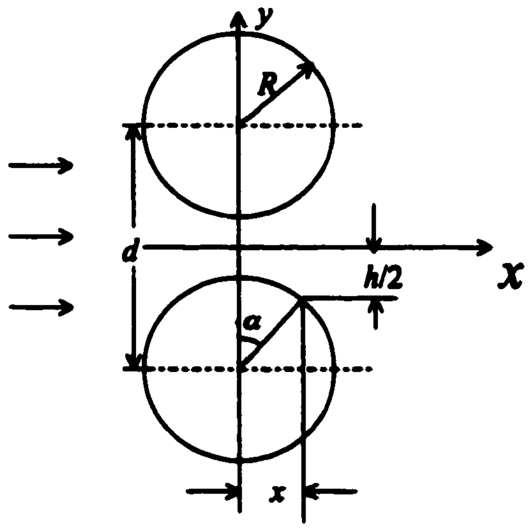

Figure 5.6 Permeability prediction using lubrication model for flow through the channel between fiber surfaces when fibers are arranged in square pattern.

Keller's study only considered square fiber arrangement pattern. Also it assumed that fibers are closely packed ($e=0.5d\approx R$). Equation (5.3.1) is then simplified and integrated over the cylindrical surface to obtain pressure gradient across the cylinder:

$$\Delta p\approx\frac{9\pi Q\sqrt{R}}{16\sqrt{2}\,(e-R)^{5/2}}. \tag{5.3.2}$$

Equation (5.3.2) expresses the pressure gradient as a function of volume flow rate, viscosity, and fiber arrangement parameters. The superficial flow velocity is taken as:

$$v=\frac{Q}{e}. \tag{5.3.3}$$

Comparing this equation with Darcy's law, one can easily obtain the permeability for a square lattice of fibers as:

$$K\approx\frac{8}{9}\cdot\frac{\sqrt{2}\,(e-R)^{5/2}}{\pi\sqrt{R}}. \tag{5.3.4}$$

Equation (5.3.4) is an approximate prediction of fiber bed permeability when fibers are arranged in a square lattice. It can be predicted that the closer the fibers are packed, the less the error of such prediction.

Gebart's prediction

Gebart's study (1992) accounts for a different fiber arrangement pattern. The hexagonal fiber arrangement is included in this study. Fig. 5.7 shows the representative unit cell for such arrangement and flow direction relative to the flow. It is assumed that

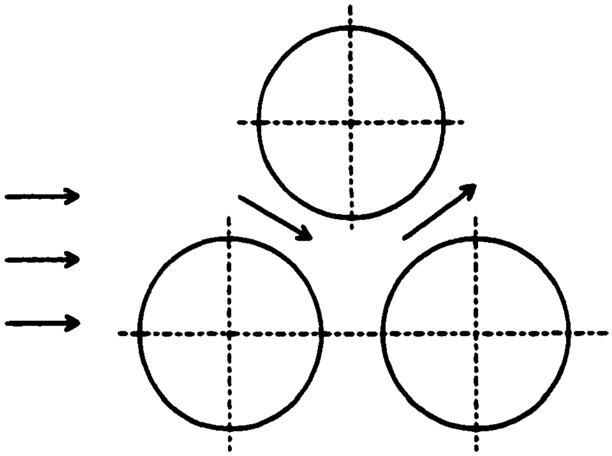

Figure 5.7 Permeability prediction using lubrication model for flow through the channel between fiber surfaces when fibers are arranged in hexagonal pattern.

the main contribution of pressure drop across the unit cell is from the channel formed by fiber surfaces when fibers are most closely packed. When fibers are squarely packed, flow passes one of such channel in every cell. When fibers are hexagonally packed, however, flow passes two of such channels, as shown in Fig. 5.7. Therefore, the pressure drop across a unit cell is two times as much as in the beds where fibers are in a square lattice. Equation (5.3.1) is used again to obtain the pressure drop across the cylindrical surface. The half channel height is approximated using a second-degree polynomial as:

$$h = \Delta + \frac{R}{2}\frac{x^2}{R^2}, \tag{5.3.5}$$

$$\Delta = e - R. \tag{5.3.6}$$

After using Eqs.(5.3.5-5.3.6), the integration between two points a and b of the channel becomes:

$$p_b - p_a = -\frac{3}{2}\frac{\mu q}{\Delta^3}\sqrt{2R\Delta}\int_{a/\sqrt{2R\Delta}}^{b/\sqrt{2R\Delta}}\frac{dt}{(1+t^2)^3}. \tag{5.3.7}$$

Gebart compared the result of the integration when different integration limit is used. It was found that the main pressure drop comes from the part of the channel near the origin. Therefore, the value of $3\pi/8$ is chosen, as the value of the integration, which is considered to be accurate enough. Then the pressure drop is obtained as:

$$\frac{\Delta p}{d} = -\frac{9\sqrt{2}\pi}{8d}\frac{\mu Q}{R^2}\left(\frac{\Delta}{R}\right)^{-5/2} . \tag{5.3.8}$$

Different from the square packing pattern, the fiber separation distance perpendicular to the flow direction is different from the distance of the flow channel. For hexagonal fiber packing pattern, the superficial velocity is expressed as:

$$v = \frac{q}{\sqrt{3}/2d}. \tag{5.3.9}$$

In order to obtain permeability as a function of fiber volume fraction, one needs the pressure drop expressed in terms of superficial velocity and fiber arrangement parameters. After substituting Eq. (5.3.9) into (5.3.8) and comparing with Darcy's law, one can obtain the permeability as a function of fiber arrangement parameters as:

$$K = \frac{16}{9\pi\sqrt{6}}\left(\frac{\Delta}{R}\right)^{5/2} R^2 \quad , \tag{5.3.10}$$

or dimensionless permeability in terms of fiber volume fraction as:

$$\overline{K} = \frac{K}{R^2} = \frac{16}{9\pi\sqrt{6}}\left(\sqrt{\frac{v_{f\,max}}{v_f}} - 1\right)^{5/2} \tag{5.3.11}$$

where $v_{f\,max}$ is the maximum possible fiber volume fraction, in this case, it is $\pi/(2\sqrt{3})$, the same value as calculated in chapter 3.

Gebart's study solved the permeability for two kinds of fiber arrangements, square and hexagonal packing pattern. Fiber bed permeability is expressed as a function of fiber volume fraction. Also, it can predict the permeability to be zero when the maximum fiber volume fraction is reached where fibers are touching with each other and block the flow. But still, it is an approximate solution to the lubrication model.

Bruschke's analytical solution

Bruschke's study (1992) of permeability prediction using lubrication theory used the same fiber arrangement pattern and flow direction as Gebart. Bruschke's work obtained the analytical solution of Eq. (5.3.1) without any approximation. The method of his analysis is the same as Gebart's. Therefore, it is considered as the analytical expression of permeability prediction. Bruschke's result of hexagonal fiber bed permeability can be written as:

$$\overline{K}=\frac{1}{3\sqrt{3}}\frac{(1-l^2)^2}{l}\left(3\frac{\arctan(\sqrt{(1+l)/(1-l)})}{\sqrt{1-l^2}}+\frac{1}{2}l^2+1\right)^{-1} . \qquad (5.3.12)$$

$$l^2=\frac{2\sqrt{3}}{\pi}v_f \qquad (5.3.13)$$

5.3.2. Extended Lubrication Model

The common assumption of all the previous research is that they all assume that fibers are closely packed. The closest fiber separation is small compared to fiber radius. Examining the analytical expression for the integration of pressure drop by Bruschke (1992), one can see that the integration limit is from $x=0$ to $x=R$ in the flow channel. If fibers are packed in a square lattice, this integration is valid for the whole range of fiber volume fraction. If fibers are hexagonally packed, these integration limits might not be applicable. As pointed out in chapter 3, the flow channel will be blocked by the appearance of another fiber in the flow downstream when fiber volume fraction exceeds a certain limit. For hexagonal packing, this blocking happens when the nearest fiber separation distance exceeds 30% of the fiber radius. If the flow channel is blocked, the above integration needs to be reconsidered.

Figure 5.8 shows the fiber arrangement pattern and flow directions used in this study. Fibers form repeatable isosceles triangles with bottom angle β and the length of

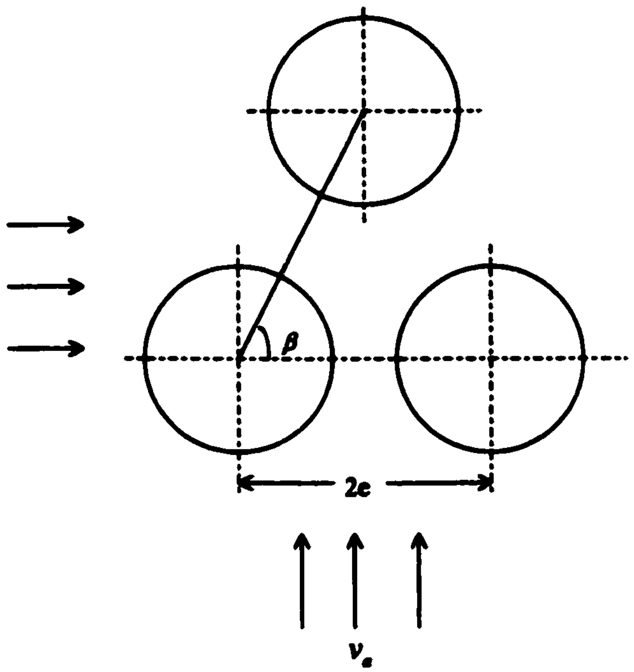

Figure 5.8 Permeability prediction using lubrication model for different flow directions relative to the isosceles triangle of the fiber arrangement.

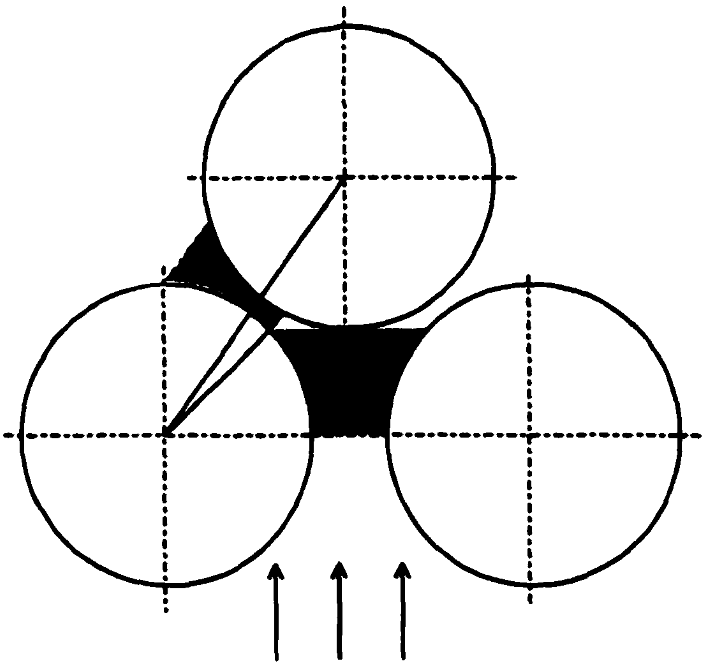

Figure 5.9a Separation of flow channel for permeability prediction using lubrication model when flow direction is shown as v_a in Fig. 5.8.

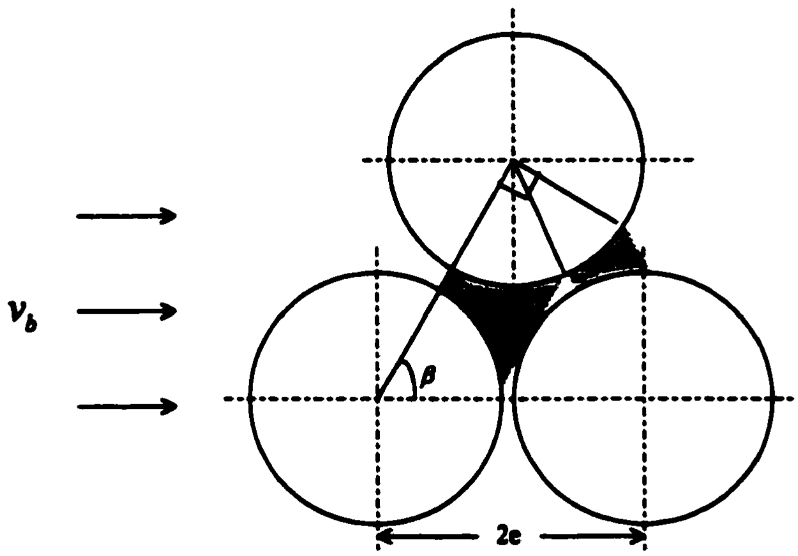

Figure 5.9b Separation of flow channel for permeability prediction using lubrication model when flow direction is shown as v_b in Fig. 5.8.

the bottom side $2e$. The length of the two equal sides of the isosceles triangle is defined as $2e_1$. Two flow directions, marked as v_a and v_b in the figure, are considered. The same as in others work, permeability of the fiber bed is calculated by analyzing the narrowest flow channel in the fiber bed. For an isosceles triangle, the narrowest channel is not necessarily in the flow direction. It might be inclined to the flow, as in Gebart and Bruschke's work. When flow is along a direction shown in Fig. 5.8, the criterion for the narrowest channel to be in the flow direction is:

$$cos\,\beta = \frac{e}{2e_1} \leq 0.5\,, \qquad \beta \geq 60^o\,. \tag{5.3.14}$$

When fiber arrangement satisfies Eq. (5.3.14), the choice of flow channel in permeability prediction is shown in Fig. 5.9a. It can be seen that this flow channel is similar to the ones used in the calculation of capillary impregnation in chapter 3. Flow channel repeatedly separates into two identical channels and then joins into a new channel. If flow direction is turned 90 degrees, the formation of flow channel is shown in Fig. 5.9b. The channels in which fibers are packed closest are inclined to the flow direction. Therefore, one needs to pick up these inclined channels to analyze the permeability. No splitting of channel happens for the analysis of permeability. For any isosceles triangular fiber-packing pattern, these are the two kinds of formation of flow channel for the analysis of permeability.

To analysis fiber bed permeability shown in Fig. 5.9a, the integration of pressure drop consists of two parts: integration of pressure drops in the channel along the flow direction and integration of pressure drops in the channel inclined to the flow direction. The appearance of the integration in the channel inclined to the flow direction comes from the blockage of the channel along flow direction by the downstream fiber. When fiber volume fraction is low such that the blockage will not happen, the integration of pressure drops in the inclined channel becomes zero. The expression of the half channel height of the channel along flow direction is the same as in the previous work:

$$h = e - \sqrt{R^2 - x^2}\,. \tag{5.3.15}$$

For the inclined channel, e_1 is related with e as:

$$e_1 = e/(2\cos\beta). \tag{5.3.16}$$

Since the pressure drop across the two channels are calculated separately, x axis is moved to the center of the second channel for the convenience of integration. Therefore, the expression for half of the channel height for the inclined channel is:

$$h_1 = \frac{e}{2\cos\beta} - \sqrt{R^2 - x^2}\,. \tag{5.3.17}$$

In order to carry out the integration of pressure drop in the corresponding channel, the limit of the integration needs to be specified. After the transformation of coordinate system into a cylindrical coordinate system, the general expression for the integration of Eq. (5.3.1) from zero to x $(x \le R)$ can be written as:

$$\Delta p(Q,e,\alpha) = \frac{3}{2} Q\mu \frac{R}{(e^2 - R^2)^2} (3Re \frac{\arctan(\gamma\sqrt{\frac{e+R}{e-R}})}{\sqrt{e^2 - R^2}} + \frac{(e+R)(2e^2 - eR - 2R^2)\gamma^3 + (e-R)(2e^2 + eR - 2R^2)\gamma}{(e+R)^2\gamma^4 + 2(e+R)(e-R)\gamma^2 + (e-R)^2}). \tag{5.3.18}$$

where $\gamma = \tan\alpha/2$, α represents the angle related with x as shown in Fig.5.6. Thus, the choice of integration limit becomes the choice of α. For the channel formation shown in

Fig. 5.9a, α changes from zero to $arcsin(e\tan\beta / R-1)$ in the channel along flow direction. Thus, pressure drop becomes:

$$\Delta p_1 = \Delta p(Q, e, are\sin(e\tan\beta / R-1)). \quad (5.3.19)$$

In the inclined channel, α changes from $arcsin(e\tan\beta / R-1)-\beta$ to $\pi/2-\beta$. Also in the inclined channel, since flow is separated equally into two identical channels, the flow rate is decreased in half. Also the channel height is different from channel I. For this channel, e_1 takes the place of e in Eq. (5.3.18). Thus, Pressure drop becomes:

$$\Delta p_2 = \Delta p(0.5Q, e_1, \pi/2-\beta) - \Delta p(0.5Q, e_1, are\sin(e\tan\beta / R-1)-\beta). \quad (5.3.20)$$

The total pressure drop p_{tol} is the sum Δp_1 and Δp_2. The superficial velocity is defined as:

$$v = \frac{Q}{e}. \quad (5.3.21)$$

Having obtained the pressure drop p_{tol}, the pressure gradient is calculated as:

$$\frac{dp}{dx} = \frac{p_{tol}}{e\tan\beta}. \quad (5.3.22)$$

Eliminate the flow rate term from the Eqs. (5.3.21) and (5.3.22), one can get the expression of flow velocity as a function of fiber arrangement parameters and the viscosity of the fluid. The resulting equation can be compared with Darcy's law to obtain the permeability as:

$$\overline{K}_e = \frac{K_e}{R^2} = \frac{1}{\tan\beta}\cdot\frac{1}{3l^4/(1-l^2)^2(T(l,\gamma_1)) + 3l_1^4/(2\cdot(1-l_1^2)^2)(T(l_1,\gamma_2)-T(l_1,\gamma_3))}; \quad (5.3.23)$$

$$l = \frac{R}{e}\sqrt{\frac{2v_f\tan\beta}{\pi}}; \quad (5.3.24)$$

$$l_1 = \frac{R}{e_1} = 2l \cos\beta \, ; \tag{5.3.25}$$

$$T(l,\gamma) = 3e \frac{arctan(\gamma\sqrt{\frac{1+l}{1-l}})}{\sqrt{1-l^2}} + \frac{(1+l)(2-l-2l^2)\gamma^3 + (1-l)(2+l-2l^2)\gamma}{(1+l)^2\gamma^4 + 2(1+l)(1-l)\gamma^2 + (1-l)^2}) \, ; \tag{5.3.26}$$

$$\gamma_1 = tan\{0.5\, arcsin(tan\beta / l - 1)\} \, ; \tag{5.3.27}$$

$$\gamma_2 = tan\left(\frac{\pi}{4} - \frac{\beta}{2}\right) ; \tag{5.3.28}$$

$$\gamma_3 = tan\{0.5(arcsin(tan\beta / l - 1) - \beta)\} \, . \tag{5.3.29}$$

when flow direction is the one as shown in Fig. 5.9b, the integration of pressure drop consists integration in two inclined channels with different integration limits. The expression for the channel height is the same as in Eq.(5.3.17). Since no separation of channel happens, the flow rates in the two channels are the same. α changes from zero to $arcsin(e_1 \, tan\beta / R - 1)$ in the first channel and in the second channel, α changes from $\pi/2 - \beta - arcsin(e_1 \, tan\beta / R - 1)$ to β in the second channel. The pressure gradient is:

$$\frac{dp}{dx} = \frac{p_{tol}}{e} \, . \tag{5.3.30}$$

The superficial velocity is:

$$v = \frac{Q}{e \, tan\beta} \, . \tag{5.3.31}$$

After a similar procedure, the final expression of fiber bed permeability as a function of fiber volume fraction is obtained as:

$$\overline{K}_b = \frac{K_b}{R^2} = \frac{1}{tan\beta} \cdot \frac{1}{3l^4/(1-l^2)^2(T(l,\gamma_1)) + 3l_1^4/(1-l_1^2)^2(T(l_1,\gamma_2) - T(l_1,\gamma_3))} \, ; \tag{5.3.32}$$

$$l = \frac{R}{e}\sqrt{\frac{2 v_f \tan\beta}{\pi}}\,; \tag{5.3.33}$$

$$l_1 = \frac{R}{e_1} = 2l\cos\beta\,; \tag{5.3.34}$$

$$T(l,\gamma) = 3e\frac{\arctan(\gamma\sqrt{\frac{1+l}{1-l}})}{\sqrt{1-l^2}} + \frac{(1+l)(2-l-2l^2)\gamma^3 + (1-l)(2+l-2l^2)\gamma}{(1+l)^2\gamma^4 + 2(1+l)(1-l)\gamma^2 + (1-l)^2})\,; \tag{5.3.35}$$

$$\gamma_1 = \tan\{0.5\arcsin(\tan\beta/l - l)\}\,; \tag{5.3.36}$$

$$\gamma_2 = \tan\left(\frac{\beta}{2}\right); \tag{5.3.37}$$

$$\gamma_3 = \tan\{0.5(\frac{\pi}{2} - \arcsin(\tan\beta/l - l) - \beta)\}\,. \tag{5.3.38}$$

As one can see from Eqs. (5.3.23) and (5.3.32), the permeability of a fiber bed when fibers are arranged in isosceles triangular pattern varies with the flow direction relative to the triangle. Therefore, the current model can predict the anisotropy of the permeability. When fiber volume fraction is low such that the separation of channel described above does not happen, the second part of the integration of pressure drops is reduced to zero. The current model goes back to the same as the previous research result.

The current model considers blockage of flow channel because of fiber arrangement. When fibers are packed in a rectangular pattern, this blockage won't happen. The anisotropy of the permeability can also be considered. Figure 5.10 shows the geometry and fiber arrangement parameters in a rectangular fiber arrangement. It is assumed the rectangle of fiber arrangement is in such a way that the length of the longer

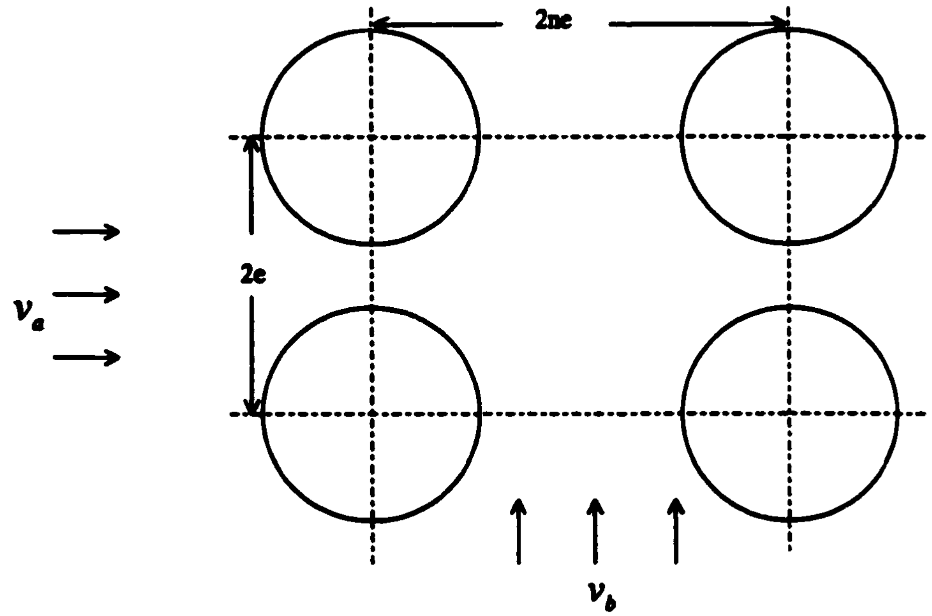

Figure 5.10 Permeability prediction using lubrication model for different flow directions when fibers are arranged in rectangular pattern.

side of the rectangle is n times of the shorter side. Half-length of the shorter side is e; then fiber volume fraction is written in terms of e and n as:

$$v_f = \frac{\pi R^2}{4ne^2} \tag{5.3.39}$$

Since there is no separation of channel, the integration of pressure drop can take the limit of α instead of zero to $\pi/2$. The difference in permeability comes from the difference in the channel height in the flow direction. With a similar deviation as before, one can obtain the expression for flow perpendicular to the shorter side of the rectangle in terms of fiber volume fraction as:

$$\bar{K} = \frac{n}{3}\cdot\frac{\left(1-l^2\right)^2}{l^3}\left(3l\frac{\arctan\left(\sqrt{\frac{1+l}{1-l}}\right)}{\sqrt{1-l^2}} + \frac{l^2}{2} + 1\right)^{-1}; \tag{5.3.40}$$

$$l^2 = \frac{4nv_f}{\pi} \tag{5.3.41}$$

The permeability for flow perpendicular to the longer side of the rectangle can be obtained similarly in terms of fiber volume fraction as:

$$\bar{K} = \frac{1}{3n}\cdot\frac{\left(1-l_1^2\right)^2}{l_1^3}\left(3l\frac{\arctan\left(\sqrt{\frac{1+l_1}{1-l_1}}\right)}{\sqrt{1-l_1^2}} + \frac{l_1^2}{2} + 1\right)^{-1}; \tag{5.3.42}$$

$$l_1^2 = \frac{4v_f}{n\pi}. \tag{5.3.43}$$

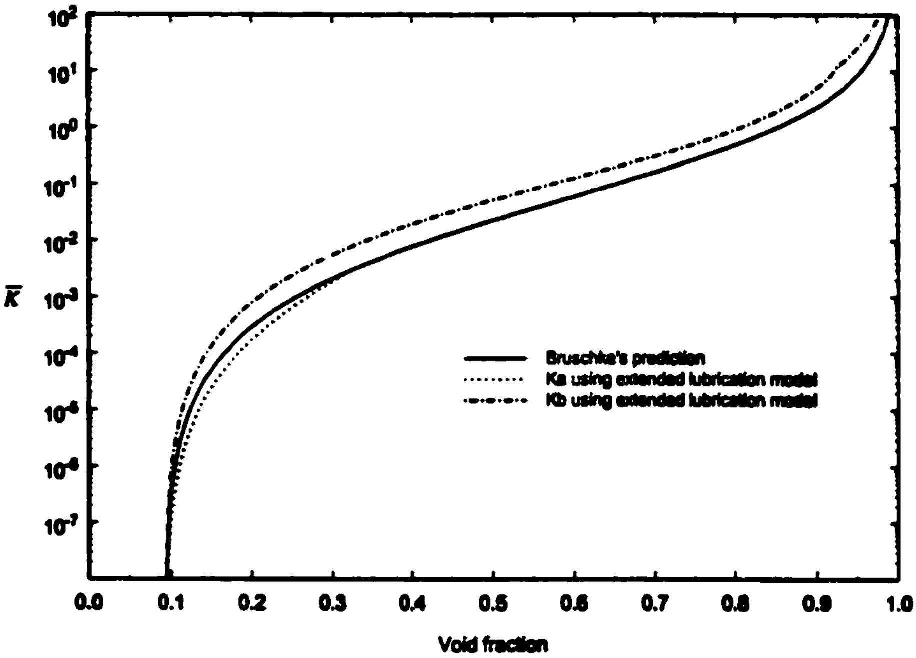

Figure 5.11 Permeability change with fiber volume fraction using extended lubrication model and the comparison with Bruschke's prediction. Fibers are packed in hexagonal pattern. ε=1-v_f.

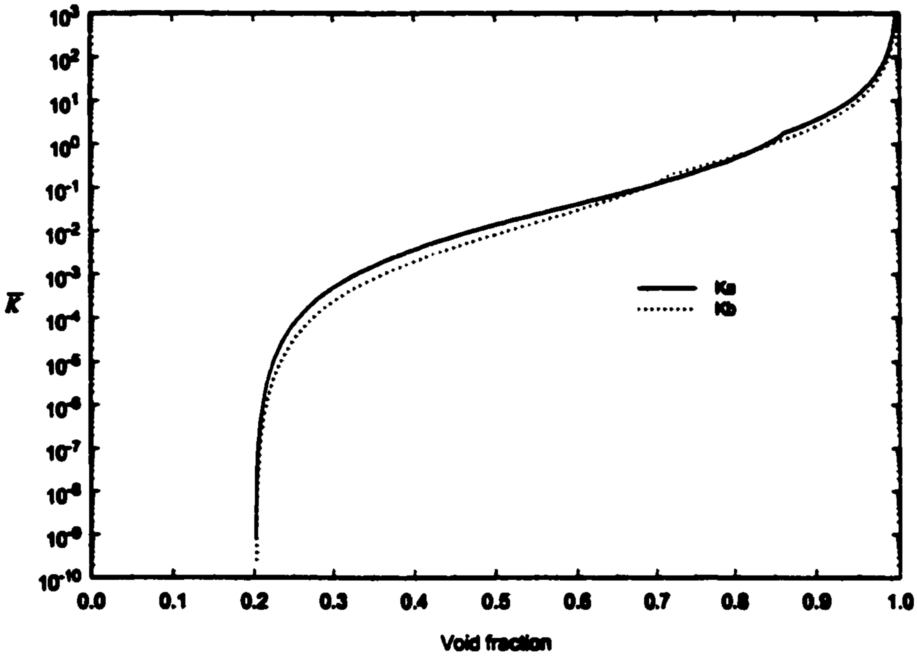

Figure 5.12 Permeability change with fiber volume fraction using extended lubrication model. Fibers are packed in isosceles triangular pattern. β=50°.

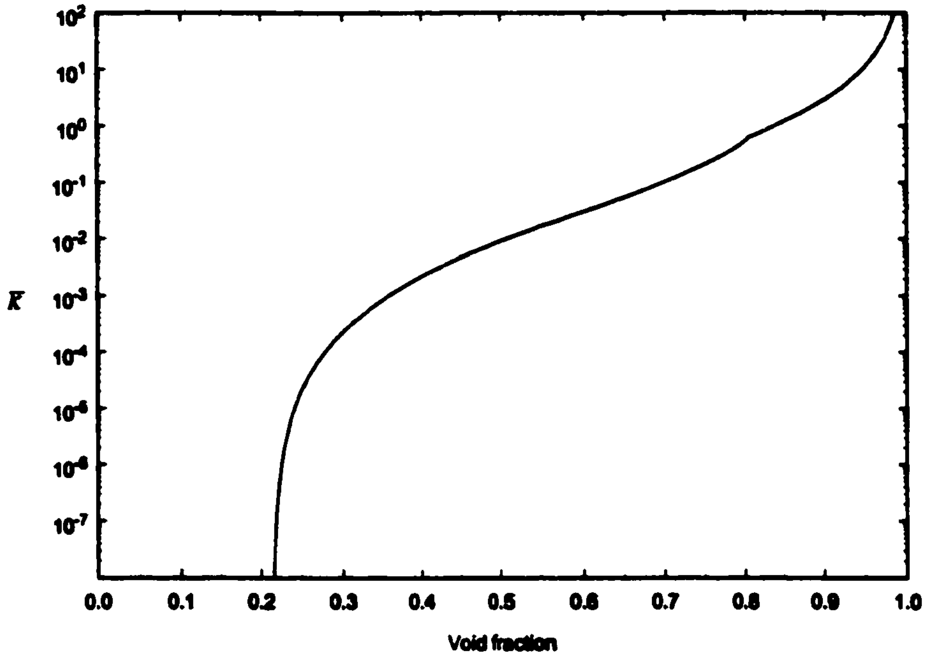

Figure 5.13 Permeability change with fiber volume fraction using extended lubrication model. Fibers are packed in isosceles triangular pattern. β=45°.

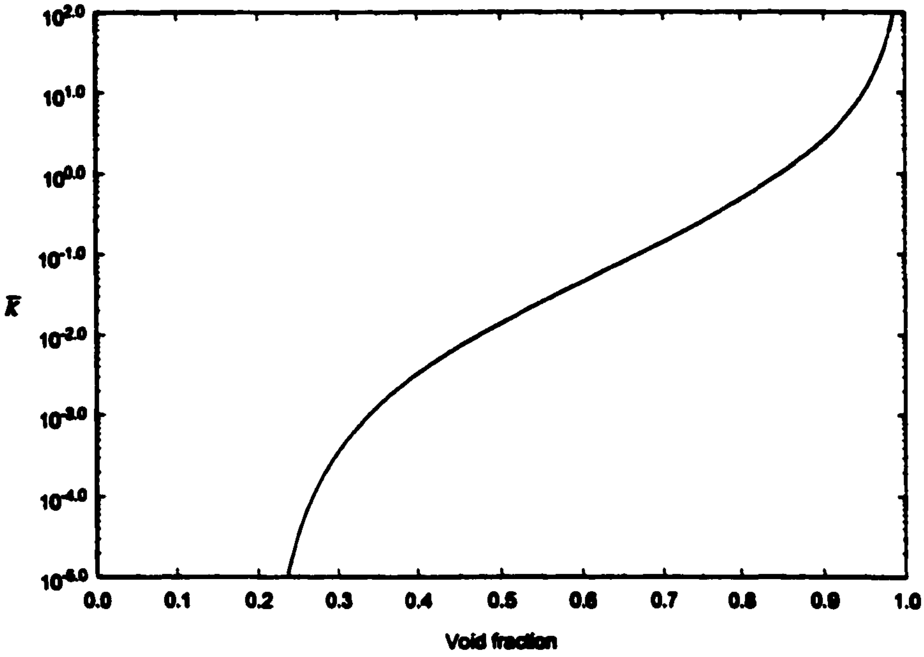

Figure 5.14 Permeability change with fiber volume fraction using extended lubrication model. Fibers are packed in square pattern.

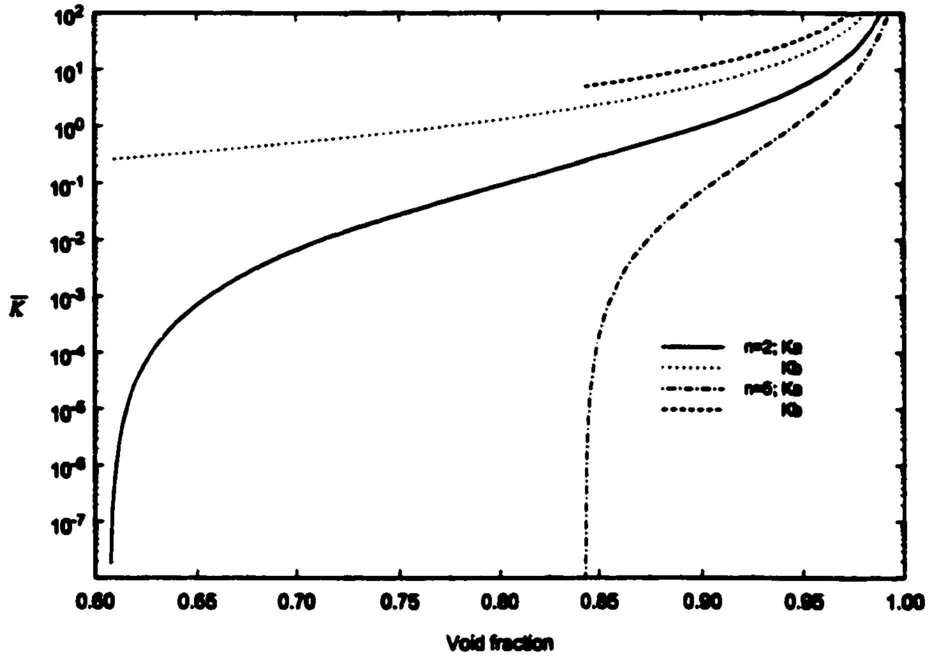

Figure 5.15 Permeability change with fiber volume fraction using extended lubrication model. Fibers are packed in rectangular pattern with different ratio of the two sides.

5.3.3 Permeability Prediction of Different Fiber Packing Patterns

Permeability of a fiber bed is regarded as one of its physical properties. The value of the permeability depends on the fiber arrangement pattern and fiber volume fraction. The properties of the fluid that flow through the fiber bed have no influence to the permeability value. The analytical prediction of the permeability of a fiber bed for different fiber packing patterns is shown in this chapter. Two kinds of fiber arrangement patterns: triangular and rectangular packing patterns are used. For triangular packing, the structure of fiber bed goes back to the hexagonal pattern when the triangle becomes equilateral. For rectangular packing, the square packing becomes its special case of fiber packing pattern. The result of permeability along different side of the rectangle is presented.

Figure 5.11 shows the permeability predictions for a hexagonal fiber arrangement pattern as a function of fiber volume fraction. The anisotropic permeabilities are included in the figure. Bruschke's analytical result is used as a comparison with the current prediction. As pointed out in chapter 3, flow channel will be blocked when fiber volume fraction exceeds 67%. The figure shows that for fiber volume fraction higher than this value, Bruschke's prediction of permeability gave a higher value of permeability estimation. The current prediction, however, shows that the permeability decreases faster in when fiber volume fraction is high. This result is consistent with the previous numerical calculation of capillary impregnation and also the experimental data. For flow in the other direction, however, permeability is higher than in the current direction. Another observation is that the difference between permeability in the two directions decreases as the fiber volume fraction increases.

Figure 5.12 shows the permeability for triangular fiber packing when the bottom angle is 50 degrees. It can be seen that although permeability is still different in two flow directions, the difference between the permeability in these two directions is smaller compared with the ones in Fig. 5.10. The difference in permeability in different directions decreases with fiber volume fraction. This trend is the same as in Fig. 5.10.

Figure 5.13 shows the permeability as a function of fiber volume fraction when the bottom angle is 45 degrees. There is no difference for flow in the two different directions. Therefore, the permeability is isotropic.

As one can observe from Figs. 5.11-5.13, the difference in permeability for different flow directions never exceeds one order of magnitude. This is the consistent result as the ones in chapter 4.

Figure 5.14 shows the permeability as a function of fiber volume fraction when fibers are arranged in a square pattern. Again, Bruschke's result is included as a comparison. Since there is no blockage of flow channel for square packing, the two results are identical.

Figure 5.15 shows the permeability as a function of fiber volume fraction when fibers are packed in a rectangular pattern. The ratio of the two sides of the rectangle, n, is chosen to be 2 and 5. It can be seen that the difference in permeability in different directions changes with fiber volume fraction as well as the ratio n.

5.4 Conclusion

Fluid front motion during impregnation of a fiber bed with capillary forces and a slight amount of external pressure is investigated. The change of fluid front shape during the impregnation can make the capillary force to an opposite direction such that it becomes the resistance force to the impregnation. The amount of such change in free surface shape changes with fiber volume fraction as well as the value of the external pressure. The amount of external pressure that can be added to the impregnation so that the free surface keeps circular is limited.

The in-plane permeability of a fiber bed changes with flow direction. The difference in permeability for different flow direction won't exceed one order of magnitude. Using lubrication model to predict fiber bed permeability, the blockage of flow channel is considered for high fiber volume fractions. Permeability prediction is lower than the previous results. For permeability of low fiber volume fraction, the permeability prediction has identical value with the previous results. If fibers are arranged in a rectangular pattern, no consideration of blockage in flow channel is needed. For such fiber arrangement, the permeability difference depends on the ratio of the two sides in the rectangle and fiber volume fraction.

Chapter 6 GENERAL CONCLUSIONS

This work studies the fluid front motion through porous in a gravity field. Both the static fluid surface shape and dynamic fluid surface motion are discussed. Static free surface shape in a two-dimensional channel for different Bond number, contact angle and the inclination of the channel is obtained numerically. The analytical solution of the free surface shape for a horizontal channel is obtained and compared with the numerical calculation. Dynamic free surface motion through a porous fiber bed driven by capillary forces is studied by using the quasi-static capillary motion theory from Washburn. Gravity effect is included in the analysis so the final position of the free surface can be predicted. Free surface shapes and locations during different times during capillary impregnation are obtained for different Bond numbers, contact angles, and fiber volume fractions. Permeability of the fiber bed obtained from the impregnation velocity is compared with previous research results. The anisotropic permeability of a fiber bed is obtained from free surface velocity during impregnation. Finally, permeability prediction by lubrication theory is discussed and an extension of the permeability model is suggested.

In chapter 2, free surface shapes in a two-dimensional channel for different Bond numbers, contact angles and inclination angles are obtained. The changes of the free surface shape with Bond number, contact angle and inclination angle of the channel are discussed. For a horizontal channel, the numerical calculation of the free surface shape is found to be identical with the analytical solution. The spreading of the free surface in the horizontal channel is discussed.

Chapter 3 investigates capillary impregnation through a fiber bed. Fluid front motion during impregnation is obtained for different fiber volume fractions, contact angles and Bond numbers. Fluid front velocity is found to change periodically as it moves through layers of fibers. Gravity effect is found to affect the impregnation more significantly during the final stage of impregnation. The velocity of the fluid front motion is used to obtain the permeability of the fiber bed. Permeability data obtained in this study are found to agree with the ones from lubrication model and experimental data available in the literature.

In chapter 4, capillary impregnation of an anisotropic fiber bed is studied. Transient fluid front locations and shapes at different times are obtained for different fiber volume fractions, contact angles and fiber packing angles. Anisotropic permeabilities are obtained using fluid front velocity along different impregnation paths. The ratio of longitudinal to normal permeability is found to be within two orders of magnitude.

Chapter 5 studies fluid front motion during impregnation of a fiber bed with capillary forces and a slight amount of external pressure. The change of fluid front shape during the impregnation can make the capillary force to opposite impregnation. The variation in free surface shape changes with fiber volume fraction and the value of the external pressure. However, the amount of external pressure that can be added to the impregnation so that the free surface keeps circular is limited.

The transverse permeability of a fiber bed changes with flow direction. The difference in permeability for different flow direction will not exceed two orders of magnitude. Lubrication model to predict fiber bed permeability is improved by accounting for the blockage of flow channel for high fiber volume fractions. Permeability prediction is lower than the previous results. For permeability of low fiber volume fraction, the permeability has identical value with the previous results. If fibers are arranged in a rectangular pattern, consideration of blockage in flow channel is not needed. For such fiber arrangements, the permeability difference depends on the ratio of the two sides in the rectangle and fiber volume fraction.

BIBLIOGRAPHY

Adams, K. L. and Rebenfeld, L., 1991, "Permeability Characteristics of Multilayer Fiber Reinforcements. Part I: Experimental Observations, " Polymer Composite, Vol.12 (3), pp. 179-185.

Adams, K. L. and Rebenfeld, L., 1991, "Permeability Characteristics of Multilayer Fiber Reinforcements. Part II: Theoretical Model, " Polymer Composite, Vol. 12 (3), pp. 186-190.

Ahn, K. J. and Seferis, J. C., 1991, "Simultaneous Measurements of permeability and Capillary Pressure of Thermosetting Matrices in Woven Fabric Reinforcements," Polymer Composites, Vol. 12(3), pp.146-152.

Ahn, S. H., Lee, W. I. and Springer, G. S., 1995, "Measurement of the Three-Dimensional Permeability of Fiber Preforms Using Embedded Fiber Optic Sensors," Journal of Composite Materials, Vol. 29(6), pp. 714-733.

Astrom B. T., Pipes, R. B. and Advani, S. G., 1992 "On flow through Aligned Fiber Beds and Its Application to Composites Processing," Journal of Composite Materials, Vol. 26(9), pp.1351-1373.

Bayramli, E. and Powell, R. L., 1990, "The Normal (Transverse) Impregnation of Liquids into Axially Oriented Fiber Bundles," Journal of Colloid and Interface Science, Vol. 138(2), pp. 346-353.

Bayramli, E. and Powell, R. L., 1991, "Experimental Investigation of the Axial Impregnation of Oriented Fiber Bundles by Capillary Forces," Colloids and Surfaces, Vol. 56, pp. 83-100.

Bayramli, E. and Powell, R. L., 1992, "Impregnation Dynamics of Carbon Fiber Tows," Journal of Composite Materials, Vol. 26(10), pp. 1427-1442.

Berdichevsky, A. L. and Cai, Z., 1993, "Preform Permeability Predictions by Self-Consistent Method and Finite Element Simulation," Polymer Composites, Vol. 14(2), pp. 132-143.

Borhan, A. and Rungta, K. K., 1993, "An experimental Study of the Radial Penetration of Liquids in Thin Porous Substrates," Journal of Colloid and Interface Science, Vol. 158, pp. 403-411.

Borhan, A., Rungta, K. K. and Marmur, A., 1991, "Capillary Penetration of Liquids between Periodically Corrugated Plates," Journal of Colloid and Interface Science, Vol. 146(2), pp. 425-433.

Bracke, M. D. Voeght, F. D., and Joos, P., 1989, "The Kinetics of Wetting: The Dynamic Contact Angle, " Progress in Colloid & Polymer Science, Vol. 79, pp.142-149.

Bruil, H. G. and Aartsen, J. J. V., 1974, "The Determination of Contact Angles of Aqueous Surfactant Solutions on Powders," Colloid and Polymer Science, Vol. 252, pp. 32-38.

Bruschke, M. I., 1992, "A Predictive Model for Permeability and Non-Isothermal Flow of Viscous and Shear-Thinning Fluids in Anisotropic Fibrous Media," Ph.D. thesis, University of Delaware.

Bruschke, M. V. and Advani, S. G., 1990, "A Finite Element/Control Volume Approach to Mold Filling in Anisotropic Porous Media," Polymer Composites, Vol. 11(6), pp. 398-405.

Bruschke, M. V. and Advani, S. G., 1993, "Flow of Generalized Newtonian Fluids Across a Periodic Array of Cylinders," Journal of Rheology, Vol. 37(3), pp. 479-498.

Cai, Z., 1992, "Estimation of the Permeability of Fibrous Preforms for Resin Transfer Molding Process," Composite Manufacturing, Vol. 3(4), pp. 251-257.

Cai, Z., 1993, "Numerical Simulation on the Permeability of a Fiber Assembly," Polymer Composites, Vol. 14(6), pp. 529-539.

Cain, J. B., Francis, D. W., Venter, R. D. and Neumann, A. W., 1983, "Dynamic Contact Angles on Smooth and Rough Surfaces," Journal of Colloid and Interface Science, Vol. 94(1), pp. 123-130.

Calado, V. M. A. and Advani, S. G., 1996, "Effective Average Permeability of Multi-Layer Preforms in Resin Transfer Molding," Composite Science and Technology, Vol. 56, pp. 519-531.

Chan, A.W. Larive, D. E. and Morgan, R. J., 1993, " Anisotropic Permeability of Fiber Reinforcements: Constant Flow Rate Measurement," Journal of Composite Materials, Vol. 27 (10), pp. 996-1008.

Chen, H. and Saghir, M. Z., 1994, "Nonaxisymmetric Equilibrium Shapes of the Liquid Bridge," Microgravity Science and Technology, Vol. 7(1), pp.12-19.

Chmielewski, C., Petty, C. A., and Jayaraman, K., 1990, "Crossflow of Elastic Liquids Through Arrays of Cylinders," Journal of Non-Newtonian Fluid Mechanics, Vol, 35, pp. 309-325.

Clague, D. S. and Phillips, R. J., 1997, "A Numerical Calculation of the Hydraulic Permeability of Three-Dimensional Disordered Fibrous Media," Physics of Fluids, Vol. 9(6), PP. 1562-1572.

Concus, P., 1964, "Capillary Stability in an Inverted Rectangular Channel for Free Surfaces with Curvature of Changing Sign" AIAA Journal, Vol. 2(12), pp. 2228-2230.

Concus, P., 1968, "Static Menisci in a Vertical Right Circular Cylinder," Journal of Fluid Mechanics, Vol. 34(3), pp. 481-495.

Danino, D. and Marmur, A., 1994, "Radial Capillary Penetration into Paper: Limited and Unlimited Reservoirs," Journal of Colloid and Interface Science, Vol. 166, pp. 245-250.

Dreyer, M., Delgado, A. and Rath, H. 1994, "Capillary Rise of Liquid between Parallel Plates under Microgravity," Journal of Colloid and Interface Science, Vol. 163, pp. 158-168.

Drummond, J. E. and Tahir, M. I., 1984, "Laminar Viscous Flow Through Regular Arrays of Parallel Solid Cylinders," International Journal of Multiphase Flow, Vol. 10(5), pp. 515-540.

Dussan V, E. B. and Davis, S. H., 1974, "On the Motion of a Fluid-Fluid Interface along a Solid Surface," Journal of Fluid Mechanics, Vol. 65(1), pp. 71-95.

Dussan V, E. B., 1976, "The Moving Contact Line: the Slip Boundary Condition," Journal of Fluid Mechanics, Vol. 77(4), pp.665-684.

Dussan V, E. B., Rame, E., and Garoff, S., 1991, "On Identifying the Appropriate Boundary Conditions at a Moving Contact Line: an Experimental Investigation," Journal of Fluid Mechanics, Vol. 230, pp. 97-116.

Ferland, P., Guittard, D. and Trochu, F., 1996, "Concurrent Methods for Permeability Measurement in Resin Transfer Molding," Polymer Composites, Vol. 17(1), pp. 149-158.

Fermigier, M. and Jenffer, P., 1991, "An Experimental Investigation of the Dynamic Contact Angle in Liquid-Liquid Systems," Journal of Colloid and Interface Science, Vol. 146(1), pp. 226-241.

Gauvin, R. and Chibani, M., 1990, "A Study of Permeability of Non-Woven Reinforcements in Composite Molding," SAMPE Quarterly, Vol. 21(3), pp. 52-58.

Gauvin, R., Trochu, F., Lemenn, Y. and Diallo, L., 1996, "Permeability Measurement and Flow Simulation Through Fiber Reinforcement," Polymer Composites, Vol. 17(1), pp. 34-42.

Gebart, B. R. and Lidstorm, P., 1996, "Measurement of In-Plane Permeability of Anisotropic Fiber Reinforcements, " Polymer Composite, Vol. 17 (1), pp.43-51.

Gebart, B. R., 1992, "Permeability of Unidirectional Reinforcements for RTM," Journal of Composite Materials, Vol. 26(8), pp. 1100-1133.

Good, R. J., 1973, " The Rate of Penetration of a Fluid into a Porous Body Initially Devoid of Absorbed Material (1,2)," Journal of Colloid and Interface Science, Vol. 42(3), pp. 473-477.

Gutowski, T. G., Morigaki, T. and Cai, Z., 1987, "Consolidation Experiments for Laminate Composites," Journal of Composite Materials, Vol. 21, pp.650-659.

Happel, J., 1959, "Viscous Flow Relative to Arrays of Cylinders," A. I. Ch. E. Journal, Vol. 5(2), pp174-177.

Hartland, S. and Hartley, R. W., 1976, "Axisymmetric Fluid-Liquid Interfaces," Elsevier Scientific Publishing Company, Amsterdam-Oxford-New York.

Hashimoto, H., 1959, "On the Periodic Fundamental Solutions of the Stokes Equations and Their Application to Viscous Flow Past a Cubic Array of Spheres," Journal of Fluid Mechanics, Vol. 5(2), pp. 317-328.

He, J. and Altan, M. C., 2000, "Quasi-Static Capillary Impregnation of a Fiber Bed with Gravity Effects," Journal of Materials Processing & Manufacturing Science, Vol. 8(1), pp. 40-52.

Hodgson, K. T. and Berg, J. C., 1988, "The Effect of Surfactants on Wicking Flow in Fiber Networks," Journal of Colloid and Interface Science, Vol. 121(1), pp. 22-31.

Hoffman, R. L., 1975, "A Study of the Advancing Interface I. Interface Shape in Liquid-Gas Systems," Journal of Colloid and Interface Science, Vol. 50(2), pp. 228-241.

Hristopulos, D. T. and Christakos, G., 1997, "Variational Calculation of the Effective Fluid Permeability of Heterogeneous Media," Physics Review E, Vol. 55(6), pp. 7288-7298.

Huh, C. and Mason, S. G., 1977, "The Steady Movement of a Liquid Meniscus in a Capillary Tube," Journal of Fluid Mechanics, Vol. 81(3), pp. 401-419.

Huh, C. and Scriven, L. E., 1969, "Shapes of Axisymmetric Fluid Interface of Unbounded Extent," Journal of Colloid and Interface Science, Vol. 30(3), pp. 323-337.

Ishimi, K. and Mohri, J., 1998, "Dynamic Wetting and Advancing Contact Angles in Horizontal Capillary, " Journal of Chemical Engineering of Japan, Vol. 31 (6), pp. 914-921.

Jiang, T. Oh, S. and Slattery, J. C., 1975, "Correlation for Dynamic Contact Angle, " Journal of Colloid and Interface Science, Vol. 69 (1), pp.74-77.

Joos, P., Remoortere, P. V., and Bracke, M., 1990, "The Kinetics of Wetting In a Capillary," Journal of Colloid and Interface Science, Vol. 136 (1), pp.189-197.

Kafka, F. and Dussan V, E. B., 1979, "On the Interpretation of Dynamic Contact Angles in Capillaries," Journal of Fluid Mechanics, Vol. 95(3), pp. 539-565.

Kagan, M. and Pinczewski, W. V., 1996, "Meniscus in a narrow Slit," Journal of Colloid and Interface Science, Vol. 180, pp.293-295.

Kalliadasis, S. and Chang, H., 1994, "Apparent Dynamic Contact Angle of an Advancing Gas-Liquid Meniscus," Physics of Fluids, Vol. 6(1), pp. 12-23.

Kececioglu, L. and Jiang, Y., 1994, "Flow Through Porous Media of Packed Spheres Saturated With Water," Transactions of the ASME, Vol. 116, pp. 164-170.

Keller, J. B., 1964, "Viscous Flow Through a grating or Lattice of Cylinders," Journal of Fluid Mechanics, Vol. 18, pp. 94-96.

Kim, Y. R., McCarthy S. P., Fanucci, J. P., Nolet, S. C. and Koppernaes, C., 1991, "Resin Flow Through Fiber Reinforcements during Composite Processing," SAMPE Quarterly, Vol. 22(3), pp. 16-22.

Kolosov, A. E., 1988, "Impregnation of Fibrous Fillers with Polymer Binders. 1. Kinetic Equations of Longitudinal and Transverse Impregnation," Mechanics of Composite Materials (English Translation), Vol. 23(5), pp. 625-633.

Lai, C. and Young, W., 1997, "Model Resin Permeation of Fiber Reinforcements After Shear Deformation," Polymer Composites, Vol. 18(5), pp. 642-648.

Lai, Y., Khomami, B. and Kardos, J. L., 1997, "Accurate Permeability Characterization of Preforms Used in Polymer Matrix Composite Fabrication Process," Polymer Composites, Vol. 18(3), pp. 368-377.

Lam, R. C. and Kardos, J. L., 1988, "the flow of resin through Aligned and Cross-Plied Fiber Beds during Processing of Composites," Proceedings of the ACS Division of Polymeric Materials, Science and Technology, Vol. 59, pp. 1190-1195.

Langbein, D., 1995, "Liquid Surfaces in Polyhedral Containers," Microgravity Science and Technology, Vol. 8(3), pp. 148-154.

Larson, R. E. and Higdon, J. J. L., 1987, "Microscopic Flow Near the Surface of Two-Dimensional Porous Media, Part 2. Transverse Flow, " Journal of Fluid Mechanics, Vol. 178, pp. 119-136.

Laveron-Simavilla, A. and Perales, J. M., 1995, "Equilibrium Shapes of Nonaxisymmetric Liquid Bridges of Arbitrary Volume in Gravitational Fields and Their Potential Energy," Physics of Fluids, Vol. 7(6), pp. 1204-1213.

Lawal, A. and Brown, R. A., 1982, "The Stability of Inclined Pendent Drops," Journal of Colloid and Interface Science, Vol. 89(2), pp.332-345.

Lawal, A. and Brown, R. A., 1982, "The Stability of Inclined Sessile Drops," Journal of Colloid and Interface Science, Vol. 89(2), pp.346-352.

Lee, Y. and Chiao, S., 1996, "Visualization of Dynamic Contact Angles on Cylinder and Fiber," Journal of Colloid and Interface Science, Vol. (181), pp.378-384.

Lekakou, C., Johari, M. A. K. B. and Bader, M. G., 1996, "Compressibility and Flow Permeability of Two-Dimensional Woven Reinforcements in the Processing of Composites," Polymer Composites, Vol. 17(5), pp. 666-672.

Leverett, M. C., 1941, "Capillary Behavior in Porous Solids," Transactions of AIME, Vol. 142, pp. 152-169.

Levine, S. and Neale, G. H., 1975, "Theory of the Rate of Wetting of a Porous Medium," Faraday Transactions 2, Vol. 71, pp. 12-21.

Luce, T. L., Advani, S. G., Howard, J. G. and Parnas, R. S., 1995, "Permeability Characterization. Part 2: Flow Behavior in Multi-Layer Preforms," Polymer Composites, Vol 16(6), pp. 446-458.

Lundstrom, T. S. and Gebart, B. R., 1995, "Effect of Perturbation of Fiber Architecture on Permeability Inside Fiber Tows," Journal of Composite Materials, Vol. 29(4), pp. 424-443.

Marmur, A. and Cohen, R. D., 1997, "Characterization of Porous Media by the Kinetics of Liquid Penetration: the Vertical Capillaries Model," Journal of Colloid and Interface Science, Vol. 189, pp. 299-304.

Marmur, A., 1988, "The Radial Capillary," Journal of Colloid and Interface Science, Vol. 124(1), pp. 301-308.

Martinis, I. and Perales, J. M., 1987, "Bidimensional Liquid Bridges in a Gravity Field," Acta Astronautica, Vol. 15(8), pp. 567-571.

Mason, G. and Morrow, N. R., 1984, "Meniscus Curvatures in Capillaries of Uniform Cross-Section," Faraday Transaction 1, Vol. 80, pp. 2375-2393.

Mason, G. and Morrow, N. R., 1991, "Capillary Behavior of a Perfectly Wetting Liquid in Irregular Triangular Tubes," Journal of Colloid and Interface Science, Vol. 141(1), pp. 262-274.

Mason, G. and Morrow, N. R., 1994, "Effect of Contact angle on Capillary Displacement Curvatures in Pore Throats Formed by Spheres," Journal of Colloid and Interface Science, Vol. 168, pp. 130-141.

Mogavero, J. and Advani, S. G., 1997, "Experimental Investigation of Flow through Multi-Layered Preforms," Polymer Composites, Vol. 18(5), pp. 649-655.

Ngan, C. G. and Dussan V, E. B., 1989, "On the Dynamics of Liquid Spreading on Solid Surfaces," Journal of Fluid Mechanics, Vol. 200, pp. 191-226.

O'Brien, S. B. G., 1991, "On the Shape of Small Sessile and Pendent Drops by Singular Perturbation techniques," Journal of Fluid Mechanics, Vol. 233, pp. 519-537.

Orr F. M., Scriven, L. E., and Rivas, A. P., 1975, "Menisci in Arrays of Cylinders: Numerical Simulation by Finite Elements," Journal of Colloid and Interface Science, Vol. 52(3), pp. 602-610.

Orr F. M., Scriven, L. E., and Rivas, A. P., 1975, "Pendular Rings Between Solids: Meniscus Properties and Capillary Force," Journal of Fluid Mechanics, Vol. 67(4), 723-742.

Padday, J. F. and Pitt, A., 1972, "Axisymmetric Meniscus Profiles," Journal of Colloid and Interface Science, Vol. 38(2), pp. 323-334.

Papathanasiou, T. D. and Lee, P. D., 1997, "Morphological Effects on the Transverse Permeability of Arrays of Aligned Fibers," Polymer Composites, Vol. 18(2), pp.242-253.

Parnas, R. S. and Salem, A. J., 1993, "A Comparison of the Unidirectional and Radial In-Plane flow of Fluids through Woven Composite Reinforcements," Polymer Composites, Vol. 14(5), pp. 383-394.

Parnas, R. S., Flynn, K. M. and Dal-Favero, M. E., 1997, "A Permeability Database for Composites manufacturing," Polymer Composites, Vol. 18(5), pp. 623-633.

Parnas, R. S., Howard, J. G., Luce, T. L. and Advani, S. G., 1995, "Permeability Characterization. Part 1: A Proposed Standard Reference fabric for Permeability," Polymer Composites, Vol 16(6), pp. 429-445.

Perales, J. M., 1987, "Non-Axisymmetric Effects on Long Liquid Bridges," Acta Astronautica, Vol. 15(8), pp. 561-565.

Petrov J. G. and Sedev, R. V., 1993, "Quasi-Static Shape of the Steady Moving Meniscus-Comparison of the Apparent and Extrapolated Dynamic Contact Angles," Colloids and Surfaces A, Vol. 74, pp. 233-241.

Princen, H. M., 1969, "Capillary Phenomena in Assemblies of Parallel Cylinders I. Capillary Rise between Two Cylinders," Journal of Colloid and Interface Science, Vol. 30(1), pp. 69-75.

Princen, H. M., 1969, "Capillary Phenomena in Assemblies of Parallel Cylinders II. Capillary Rise in Systems with More than two Cylinders," Journal of Colloid and Interface Science, Vol. 30(3), pp. 359-371.

Princen, H. M., 1970, "Capillary Phenomena in Assemblies of Parallel Cylinders III. Liquid Columns between Horizontal Parallel cylinders," Journal of Colloid and Interface Science, Vol. 34(2), pp. 171-184.

Rame, E. and Garoff, S., 1996, "Microscope and Macroscopic Dynamic Interface Shapes and the Interpretation of Dynamic Contact Angles," Journal of Colloid and Interface Science, Vol. 177, pp. 234-244.

Ranganathan, S., Phelan, F. R. Jr. and Advani, S. G., 1996, "A Generalized Model for the Transverse Fluid Permeability in Unidirectional Fibrous Media," Polymer Composites, Vol. 17(2), pp. 222-230.

Remoortere, P. V. and Joos, P., 1991, "The Kinetics of Wetting: The Motion of a Three Phase Contact line in a Capillary, " Journal Colloid Interface Science, Vol. 141(2), pp. 348-359.

Robitaille, F., Long, A. C., Rudd, C. D. and Souter, B. J., 1998, "The Measurement of In-Plane Permeability for Sheared Preforms," Computer Methods in Composite Materials VI, Computational Mechanics Publications, Southampton UK and Boston, USA.

Rudd, C. D., Long, A. C., McGeehin, P. and Smith, P., 1996, "In-Plane Permeability Determination for Simulation of Liquid Composite Molding of Complex Shapes," Polymer Composites, Vol. 17(1), pp. 52-59.

Sadiq, T. A. K., Advani, S. G. and Parnas, R. S., 1995, "Experimental Investigation of Transverse Flow through Aligned Cylinders," International Journal of Multiphase Flow, Vol. 21(5), pp. 755-774.

Saez E. and Carbonell, R. G., 1987, "The Equilibrium Shape and Stability of Menisci formed Between Two Touching Cylinders," Journal of Fluid Mechanics, Vol. 176, pp. 357-378.

Sangani, A. S. and Acrivos, A., 1982, "Slow Flow Past Periodic Arrays of Cylinders with Application to Heat Transfer," International Journal of Multiphase Flow, Vol. 8(3), pp. 193-206.

Sangani, A. S. and Acrivos, A., 1982, "Slow Flow Through a Periodic Arrays of Spheres," International Journal of Multiphase Flow, Vol. 8(4), pp. 343-360.

Sangani, A. S. and Yao, C., 1988, "Transport Processes in Random Arrays of Cylinders. I. Thermal Conduction," Physics of Fluids, Vol. 31(9), pp. 2426-2434.

Sangani, A. S. and Yao, C., 1988, "Transport Processes in Random Arrays of Cylinders. II. Viscous Flow," Physics of Fluids, Vol. 31(9), pp. 2435-2444.

Sanz, A. and Martinez, I., 1983, "Minimum Volume for a Liquid Bridge between Equal Disks," Journal of Colloid and Interface Science, Vol. 93(1), pp. 235-240.

Seo, J. W. and Lee, I. L., 1991, "A Model of the Resin Impregnation in Thermoplastic Composites," Journal of Composite Materials, Vol. 25, 1127-1142.

Shikhmurzaev, Y. D., 1993, "The Moving Contact Line on a Smooth Solid Surface," Journal of Multiphase Flow, Vol. 19(4), pp. 589-610.

Shikhmurzaev, Y. D., 1997, "Moving Contact Lines in Liquid/Liquid/Solid Systems," Journal of Fluid Mechanics, Vol. 334, pp. 211-249.

Siekmann, J. and Eck, W., 1977, "Analytische Bestimmung der Ebenen Trennflache Eines Zwischen Planparallelen Horizontalen Wanden Eingeschlossenen Systems Flussigkeit-Gas," Acta. Mechanica, Vol. 25, pp. 285-290.

Siekmann, J., 1979, "Note on the Capillary Curve," Journal of Non-Linear Mechanics, Vol. 14, pp. 267-272.

Slobozhanin, L. A., and Perales, J. M., 1993, "Stability of Liquid Bridges between Equal disks in an Axial Gravity Field," Physics of Fluids A, Vol. 5(6), pp. 1305-1314.

Sorbie, K. S., Wu, Y. Z. and McDougall, S. R., 1995, "The Extended Washburn Equation and its Application to the Oil/Water Pore Doublet Problem," Journal of Colloid and Interface Science, Vol. 174, pp. 289-301.

Studebaker, M. and Snow, C. W., 1955, " The Influence of Ultimate Composition upon the Wettability of Carbon Blacks," Journal of Physical Chemistry, Vol. 59, pp. 973-976.

Tallmadge, J. A., 1971, "Properties of Static Menisci on Cylinders: Analytical Expressions for Curvature and Height at Contact," Journal of Colloid and Interface Science, Vol. 37(4), pp. 801-810.

Thies-Weesie D. M. E. and Philipse, A. P., 1994, "Liquid Permeation of Bidisperse Colloidal Hard-Sphere Packings and the Kozeny-Carman Scaling Relation," Journal of Colloid and Interface Science, Vol. 162, pp. 470-480.

Thompson, P. A. and Robbins, M. O., 1989, "Simulations of Contact-Line Motion: Slip and the Dynamic Contact Angle," Physical Review Letters, Vol. 63(7), pp. 766-769.

Tilton, J. N., 1988, "The Steady Motion of an Interface between Two Viscous Liquids in a Capillary Tube," Chemical Engineering Science, Vol. 43(6), pp. 1371-1384.

Trevino, L., Rupel, K., Young, W. B., Liou, M. J. and Lee L. J., 1991, "Analysis of Resin Injection Molding in Molds with Preplaced Fiber Mats. I: Permeability and Compressibility Measurements," Polymer Composites, Vol. 12(1), pp. 20-29.

Trutschel, R. and SchellenBerger, U., 1998, "Dynamic Simulation of Free Surfaces in Capillaries with the Finite Element Method," International Journal for Numerical Methods in Fluids, Vol. 26, pp. 485-495.

Washburn, E. W., 1921, "The Dynamics of Capillary Flow," Physics Review, Vol. 17(3), pp. 273-283.

Williams, J. G., Morris, C. E. M. and Ennis, B. C., 1974, "Liquid Flow Through Aligned Fiber Beds," Polymer Engineering and Science, Vol. 14(6), pp. 413-419.

Woerdeman, D. L., Phelan, F. R. Jr. and Parnas, R. S., 1995, "Interpretation of 3-D Permeability Measurements for RTM Molding," Polymer Composites, Vol. 16(6), pp. 470-480.

Wong, H., Morris, S. and Radke, C. J., 1992, "Two-Dimensional Menisci in Nonaxisymmetric Capillaries," Journal of Colloid and Interface Science, Vol. 148, pp. 284-287.

Wong, H., Morris, S., and Radke, C. J., 1992, "Three-Dimensional Menisci in Polygonal Capillaries," Journal of Colloid and Interface Science, Vol. 148(2), pp. 317-336.

Yang, Y., Zografi, G. and Miller, E. E., 1988, "Capillary Flow Phenomena and Wettability in Porous Media II Dynamic Flow Studies," Journal of Colloid and Interface Science, Vol. 122(1), pp. 35-46.

Young, W. B., Rupel, K., Han, K., Lee, L. J. and Liou, M. J., 1991, "Analysis of Resin Injection Molding in Molds with Preplaced Fiber Mats. II: Numerical Simulation and Experiments of Mold Filling," Polymer Composites, Vol. 12(1), pp. 30-38.